The BOUSSOLE project technical reports; report #3 (t.b.c.), issue 1.

Validation of the MERIS water-leaving reflectances using MOBY *in situ* observations : a collaborative effort in the frame of the BOUSSOLE project.

David ANTOINE, André MOREL

Laboratoire d'Océanographie de Villefranche (LOV), 06238 Villefranche sur mer cedex, FRANCE

Dennis K. CLARK

NOAA National Environmental Satellite Data Information Service (NESDIS), Suitland, Maryland, USA.

Chuck R. McCLAIN

NASA Goddard Space Flight Center (GSFC), Greenbelt, Maryland 20771, USA.

Simon BELANGER, Ludovic BOURG, Vincent FOURNIER-SICRE

ACRI-st, Sophia Antipolis, 06904 Valbonne, FRANCE.

BOUSSOLE project
ESA/ESTEC contract N° 14393/00/NL/DC
CCN (rider) #2

July 11, 2003

Foreword

This report is the result of a collaborative effort between the MOBY and the SeaWiFS projects, on the one hand, and the BOUSSOLE project on the other hand. The work presented here is based on the use of data collected at the MOBY site, which has been developed and maintained by NOAA and NASA. This report is part of the technical report series that is being established by the BOUSSOLE project. Successive issues of this report might be published in a near future, when more MERIS observations are collected and more MOBY *in situ* measurements are available.

BOUSSOLE is funded/supported by the following Agencies, Institutions or Programs

European Space Agency

Centre National d'Etudes Spatiales, France

National Aeronautics and Space Administration of the USA

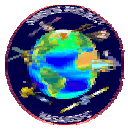

The NASA' SIMBIOS project

Centre National de la Recherche Scientifique, France

Institut National des Sciences de l'Univers, France

Université Pierre & Marie Curie, France

Observatoire Océanologique de Villefranche sur mer, France

Table of contents

1 Introduction

1.1 General context

Before starting, it is mentioned that the signals at the top-of-the-atmosphere (TOA) or at the ocean levels will be expressed as dimensionless bidirectional reflectances, ρ, which are related to radiances, L, through

$$\rho(\lambda,\theta_s,\theta_v,\Delta\phi) = \pi L(\lambda,\theta_s,\theta_v,\Delta\phi) / F_0(\lambda)\, cos(\theta_s) \quad (1)$$

where F_0 is the mean extraterrestrial irradiance, λ is wavelength, θ_s is the sun zenith angle, θ_v is the satellite viewing angle, and $\Delta\phi$ the azimuth difference between the pixel-sensor and pixel-sun half vertical planes.

The goal of the atmospheric correction applied to satellite ocean colour observations is to retrieve the water-leaving reflectance at the sea level from the total reflectance recorded at the top of the atmosphere (TOA). The water-leaving reflectances transmitted through the atmosphere form at the TOA level what is called the "marine reflectances". These reflectances are thus made of photons that have crossed the atmosphere down to the ocean, then have twice crossed the air-sea interface before reaching the sensor after a second atmospheric travel. The spectrum of the water-leaving reflectances carries information about the bio-optical state of the oceanic upper layers.

Because the atmospheric contribution largely exceeds the contribution of the ocean (in a ratio of about 10/1), the former needs to be accurately assessed for the final objective to be reachable. This accuracy has been previously determined (e.g., Gordon, 1997; Antoine and Morel, 1999), and can be expressed in slightly different terms, leading to a set of requirements that should be fulfilled. Note that these requirements are expressed in terms of uncertainties, rather than in terms of accuracy. These requirements concern on the one hand the retrieval of the water-leaving reflectance at a given wavelength, whatever the use of this data in subsequent analyses, and, on the other hand, the retrieval of the chlorophyll concentration from some parts of the water-leaving reflectance spectrum (the ratio of the reflectances at the two wavelengths 443 and 560 nm for instance).

A first requirement is a 5% uncertainty in the blue domain (*i.e.*, around 443 nm) and for oligotrophic waters (*i.e.*, chlorophyll concentration < 0.1 mg m^{-3}), which is supposed to maintain the capability of accurately computing the chlorophyll concentration in such a situation where the signal in the blue is maximum (Gordon, 1997). This is the situation that is encountered at the MOBY site for most of the time.

Another way of expressing these requirements is in terms of reflectance error. We use here the values determined in Antoine and Morel (1999). In terms of the retrieval of 30 reflectance values, the requirement is that atmospheric correction errors be maintained within ±1-2 10^{-3} at 443 nm, within ±5 10^{-4} at 490 nm, and within ±2 10^{-4} at 560 nm. Note that this last value at 560 nm is equal to the "noise equivalent reflectances" specified for MERIS. If it is assumed that atmospheric correction errors in the 440-500 nm domain are about twice the errors at 560 nm, the requirement associated to the discrimination of 30 (Chl) values is that errors remain within ±1 10^{-3} at 443 nm (then ±5 10^{-4} at 560 nm), or within ±5 10^{-4} at 490 nm (then ±2 10^{-4} at 560 nm). When expressed as relative errors, all the above requirements represent about 1% of the normalised oceanic reflectances at 443 nm (and often 2-5%), except when (Chl) > 3 mg m^{-3}. The situation is about the same for the wavelength couple 490-560 nm, except when Chl < 0.1 mg m^{-3}.

These low levels of uncertainty cannot be reached without using in-orbit "vicarious calibration" techniques, as recommended for instance by Gordon (1987, 1990, 1998). These techniques consist of measuring or predicting all components of the signal measured by the sensor at the top of the atmosphere, and then to attribute to calibration errors any difference between these predictions and the actual measurements. Several ways of achieving this vicarious calibration have been proposed, along two main pathways : the first one considers a comparison at the level of the normalised water-leaving radiances and

therefore is a calibration of the "instrument +algorithms" ensemble, whereas the second one considers the comparison at the level of the TOA total radiance.

The MOBY program has been precisely set up in the 1980's to provide a continuous record of the water-leaving radiance at an oligotrophic Case 1 waters site, in order to use these data for the vicarious calibration of the SeaWiFS and MODIS ocean colour sensors.

1.2 Practical goals

The goal of this short technical note is to present the results of a match-up analysis carried out by using on the one hand water-leaving radiances collected by the MOBY buoy ("**M**arine **O**ptical **B**uo**Y**"; Clark *et al.*, 1997, 2002), and, on the other hand, water-leaving reflectances derived from the ocean colour observations of the MERIS sensor (Rast and Bezy, 1995).

This validation exercise simply aims at identifying possible needed calibration adjustments of the MERIS bands or possible needed improvements of the MERIS level 2 algorithms (atmospheric correction and pigment retrieval). It is the first step of the "vicarious calibration" described above, the second one being the derivation of coefficients to be applied to the TOA total radiances in order to obtain the best fit in a statistical sense between the *in situ* and the satellite reflectances.

Short reminders about the MERIS level 2 algorithms concerned here and about the MOBY project are provided in this report (sections 2 & 3), before the matchup procedures and results are presented and discussed (sections 4 to 7). References are provided in the two summary sections in case further information is needed about the MOBY and about the MERIS atmospheric correction and pigment retrieval algorithms.

2 Atmospheric correction of MERIS observations above Case 1 waters

A short reminder is provided under this section about the rationale and the implementation of the MERIS atmospheric correction algorithm[1]. Further details can be found in the corresponding "Algorithm Theoretical Basis Document" (ATBD 2.7, available at http://envisat.esa.int/instruments/meris/data-app/dataprod.html#meris-level-2), and in Antoine and Morel (1998, 1999). The initial steps of the MERIS data processing are not detailed here. They concern the Level 1b processing, the pixel identification and cloud screening (ATBD 2.17) and the corrections for gas absorption (ozone and water vapour).

2.1 Physical basis and principle of the algorithm

The MERIS mission has been conceived, and the MERIS instrument accordingly designed, to meet the requirement that the discrimination of 30 classes of chlorophyll concentration, (from 0.03 to 30 mg Chl m^{-3}) should be possible. To meet this requirement, errors of about 5 10^{-4} to 1 10^{-3} in the water-leaving reflectance are tolerable, and can even reach ±2 10^{-3}. It has been shown elsewhere (Gordon, 1997) that an algorithm based on the assumption of single scattering was not able to meet this accuracy. The principle of the multiple scattering algorithm developed for MERIS is as follows.

In a situation where white caps are absent, and θ_v and $\Delta\phi$ are such that the specular reflection of direct sun rays (sun glint) is excluded, the total reflectance at the top of atmosphere level, ρ_t, is

$$\rho_t = \rho_{path} + t.\rho_w \qquad (2)$$

where ρ_w is the water-leaving reflectance, t is the diffuse transmittance along the pixel-to-sensor path, and ρ_{path} is the atmospheric path reflectance. The reflectance ρ_{path} accounts for all kinds of photon histories (except sun glint). The path reflectance can be expressed as a function of the type of scattering

[1] This text is mostly reproduced from Antoine and Morel (1997), in Ocean Optics XIII, Steven G. Ackleson and Robert Frouin Eds., Proc SPIE 2963, 101-106.

events, either of molecular or of aerosol type, with the following decomposition (the notations are those used in Antoine and Morel, 1998)

$$\rho_{path} = \rho^*_r + \rho^*_a + \rho^*_{ra} \quad (3)$$

where ρ^*_r is the reflectance which originates from scattering (single and multiple) by molecules only, but *in presence of aerosols*, ρ^*_a is the equivalent term for aerosols, also *in presence of molecules*, and ρ^*_{ra} stands for that part of ρ_{path} which strictly results from heterogeneous multiple scattering. In Antoine and Morel (1998), the behavior of the 3 terms in Eq. (3) has been examined as a function of increasing aerosol load, and it has been shown that, whatever the specific geometry (θ_s, θ_v, $\Delta\phi$) envisaged, the change in ρ_{path} resulting from the simultaneous changes of its 3 constitutive terms is nearly linear.

In the context of atmospheric correction, the three terms of Eq. (3) are not separately known or calculable, because aerosols are unknown. The only quantities at disposal are ρ_{path}, as measured in the near infrared (where it is equal to ρ_t because t.ρ_w = 0), and ρ_r, as calculated for any wavelength (depending only on the actual atmospheric pressure). The ratio [ρ_{path} / ρ_r], was also examined as a function of increasing aerosols loads. Its increase is, as for ρ_{path}, nearly linear with increasing τ_a. Examples of the change in the ratio [ρ_{path} / ρ_r] at 865 and 779 nm are displayed in Fig. 1.

The scheme for atmospheric correction is based on the above results concerning the variations of the ratio [ρ_{path} / ρ_r] with τ_a, and on the computation of ρ_r at all wavelengths. The successive steps of the correction are as follows : to the measured value of ρ_{path}(865), it is possible to associate several guess values for τ_a, each one corresponding to a given aerosol model (steps 1 and 2 in Fig. 1). Several τ_a(779) are then obtained from the spectral optical thickness of each aerosol (step 3). To these τ_a(779) values correspond several values of the ratio [ρ_{path} / ρ_r] at 779 nm , differing according to the aerosol type (steps 4 and 5). The last step consists in comparing this set of values to the actual ratio [ρ_{path} / ρ_r] at 779 nm, and by this way in selecting the two candidate aerosol models which most closely bracket the actual [ρ_{path} / ρ_r] ratio (step 6). The following rests on the assumption (Gordon and Wang, 1994) that the proportion defined in the near infrared by the actual [ρ_{path} / ρ_r] ratio and those of the two bracketing aerosols remains unchanged in the visible. A “mixing ratio” can therefore be computed, from the actual and the two bracketing values of [ρ_{path} / ρ_r]. It is then possible to transfer the estimate of [ρ_{path} / ρ_r] at any other wavelength, in particular toward the visible spectrum, provided that the relationships with τ_a have been previously established for all wavelengths. The ratios [ρ_{path} / ρ_r] in the visible are re-multiplied by the corresponding values of ρ_r,, and therefore lead to ρ_{path}, and to the desired marine reflectances. These reflectances are divided by the diffuse transmittance to obtain the water-leaving reflectances.

The retrieval of the aerosol optical thickness becomes straightforward, as a by-product of the algorithm, since a couple of aerosol models has been selected : the two values of τ_a(865) associated with these two aerosol models are simply mixed following the value of the mixing ratio mentioned above.

2.2 Implementation and test of the algorithm for clear maritime atmospheres

To implement the above algorithm, aerosol models have to be selected, which have to be as representative as possible of actual aerosols over the ocean. From the outputs of radiative transfer simulations, making use of the optical properties of these aerosols, the relationship between [ρ_{path} / ρ_r] and τ_a can be stored for various wavelengths and geometries. Aerosols are variable in nature and vertical distribution, so that a lot of situations can be encountered. Assumptions are therefore mandatory to define more or less generic cases to be used when generating lookup tables. In the present work, it has been

decided to consider the boundary layer (from the sea surface up to 2 km), the free troposphere (2-12 km), and the stratosphere (12-50 km), within which aerosols and molecules are uniformly mixed.

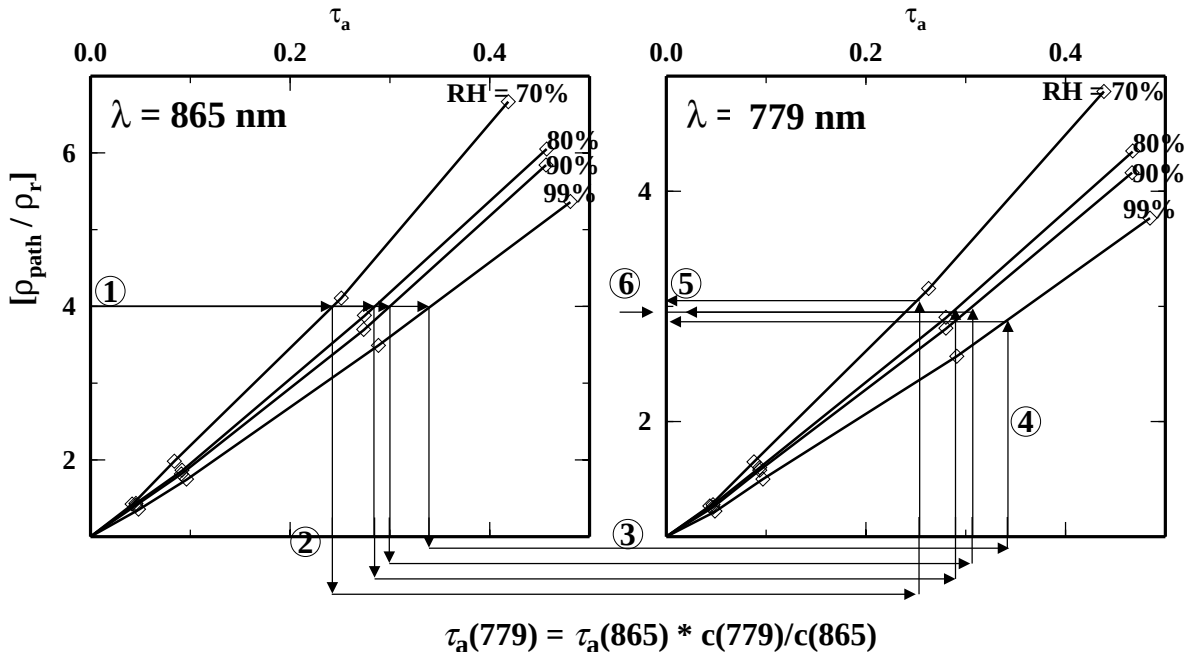

Fig. 1. Variation of the path reflectance at 865 and 779 nm as a function of the aerosol optical thickness τ_a, and expressed as the ratio $[\rho_{path} / \rho_r]$, when $\theta_s = 40°$, $\theta_v = 30°$, and $\Delta\phi = \pi/2$. The maritime aerosol model is used, for 4 values of the relative humidity, as indicated. Arrows symbolise a possible way for identifying a couple of aerosol models enclosing the actual aerosol. The circled numbers identify the successive steps of this scheme (see text).

The aerosol vertical structure as recommended by the experts working group on aerosols (WCRP, 1986) is presently adopted to represent clear maritime atmospheres. The aerosol models for each layer are constructed from the basic aerosol components defined in WCRP (1986) and Shettle and Fenn (1979). Five aerosols assemblages are defined (the word "assemblage" is used to describe the whole ensemble made up of the 3 aerosols located in the boundary layer, the free troposphere, and the stratosphere) by the relative humidity of the maritime boundary layer aerosol (i.e. 50, 70, 80, 90, or 99%). A constant aerosol background is present in the free troposphere (continental aerosol, with $\tau_a(550) = 0.025$) and in the stratosphere (H_2SO_4 aerosol, with $\tau_a(550) = 0.005$).The algorithm has been tested by using "pseudo data" obtained from the radiative transfer simulations (ρ_t and ρ_r) and the lookup tables. An histogram of the errors in the retrieved marine refletances (t.ρ_w) at 443 nm is displayed in Fig. 2, where results have been pooled together for several values of the optical thickness and geometry. Eighty percent of the errors are within $\pm 5\ 10^{-4}$, and the larger errors are about $\pm 1\ 10^{-3}$.

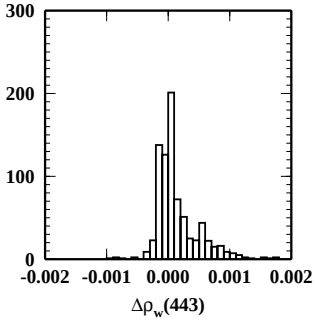

Fig. 2. Histogram of the error in the retrieved marine reflectance at 443 nm. The results for the five "standard" aerosol assemblages, four aerosol optical thicknesses, and various geometries, are here pooled together (800 cases).

2.3 Implementation and test of the algorithm for atmospheres carrying absorbing aerosols

The presence over the ocean of absorbing aerosols of continental origin is not anecdotal (Li *et al*., 1996; Andreae, 1996) and Fig. 3 shows how large the error in the retrieved marine reflectances at 443 nm might be, when the atmospheric correction is carried out by using the "standard" maritime aerosol models while the actual aerosol is absorbing. It is assumed here that absorbing aerosols over the ocean are of three main types, namely the continental aerosol, the desert dust aerosol, and the urban aerosol. The continental and desert dust aerosols are assumed to be located within the free-troposphere (2-12 km), and the urban aerosol within the boundary layer (0-2 km). The stratosphere remains unchanged in all cases. Several additional aerosol assemblages have been therefore defined, with fixed proportions between the aerosols within the boundary layer and the free troposphere.

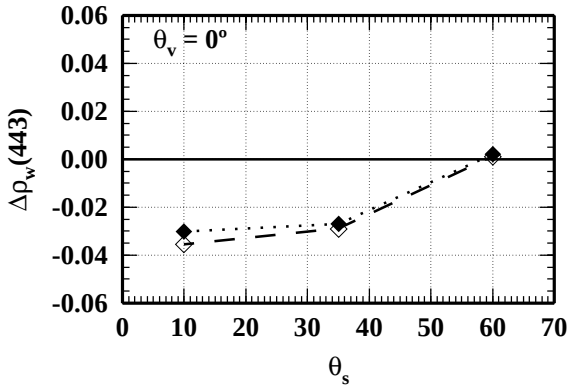

Fig. 3. Error $\Delta\rho_w(443)$, for the urban aerosol with RH = 98%, and when the standard set of aerosol models (clear maritime atmospheres) is used to carry out the correction.

To identify the presence of absorbing aerosols, a tentative correction is carried out by using the standard set of aerosol models, and then the error that is made at 709 and 510 nm is examined.

At 709 nm the error in the atmospheric correction is straightforwardly obtained ($\rho_w = 0$). The band at 709 nm is however close to the two bands used in the correction process (779 and 865 nm), and the error that is made when extrapolating to 709 nm is usually too low to detect any failure of the algorithm, except for the strongly absorbing urban aerosol.

The converse problem is faced at 510 nm, with possibly large errors in the atmospheric correction, added or subtracted however to significant water-leaving reflectances. The clue lies here in the relatively constant value of the water-leaving reflectance at 510 nm.. Measured value (Mediprod, 1976; Tyler, 1973; Paciprod, 1986; Olipac, 1992) of the diffuse reflectance of oceanic Case 1 waters at 510 nm, $R(0^-)_{510}$, are displayed in Fig. 4 as a function of chlorophyll concentration, along with the values calculated from a reflectance model (Morel and Maritorena, 2001; Morel and Gentili, 1991) and for two values of the sun zenith angle. Considering the scatter of the points, it seems wise to assign a mean value of 2% to $R(0^-)_{510}$, which leads to a mean value of the bidirectional marine reflectance (t.ρ_w) of about 0.007, with an attached uncertainty of about ±0.001. Thresholds on $\Delta\rho(510)$ have been defined : absorbing aerosols are revealed if $|\Delta\rho(510)|$ is greater than 0.002, or if it is included between 0.001 and 0.002 and the aerosol optical thickness is lower than 0.1. To ensure that the indication of the presence of absorbing aerosols is not due to an incorrect assumption on the value of t.$\rho_w(510)$, rather than to an incorrect atmospheric correction, the test is carried out twice, first with the mean value of t.$\rho_w(510)$, and second by introducing the typical error of t.$\rho_w(510)$.

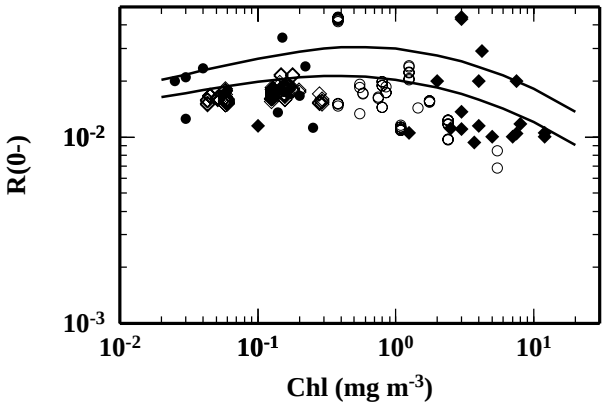

Fig. 4. Diffuse reflectance of the ocean at 510 nm, for Case 1 waters with variable chlorophyll concentration. The two curves have been obtained from a reflectance model (see text), either for a sun at zenith (bottom), or with a sun zenith angle of 60° (top). Reflectance values extracted from reflectance spectra measured at sea are also shown (Black diamonds : northeast Atlantic ocean, off Mauritania; Black circles : Galapagos islands, Caribean sea, sargasso sea; open circles and open diamonds : Pacific ocean). References in the text.

The implementation of the above algorithm for identification of absorbing aerosols and for the estimation of their contribution to the path reflectance has been tested, following the same principle than for the clear maritime atmospheres.The ability of the tests at 510 and 709 nm to detect the presence of absorbing aerosols is increasing with increasing optical thickness, and most of the absorbing aerosols are detected (not shown).

Histograms of the errors in the retrieved marine reflectance at 443 nm are shown in Fig. 5. For each kind of absorbing aerosol, 1920 values of $\Delta\rho_w 443$ are pooled together, and correspond to 4 values of the aerosol optical thickness, 40 geometries and 12 aerosol assemblages, each one corresponding to 4 values of the relative humidity for the maritime aerosol within the boundary layer, and to 3 values of the sharing of optical thickness between the boundary layer and the free troposphere. The atmospheric correction is not so accurate as for clear maritime atmospheres (Fig. 2), yet a significant percentage of the $\Delta\rho_w 443$ values remain within $\pm 2\ 10^{-3}$, namely 97, 72, and 77%, for the aerosol assemblages containing respectively the continental aerosol, the desert dust, or the urban aerosol.The above results, even if not perfect, clearly improve the quality of the atmospheric correction in situations where a classical algorithm, without the ability to address separately different kind of aerosols, would totally fail (see Fig. 3).

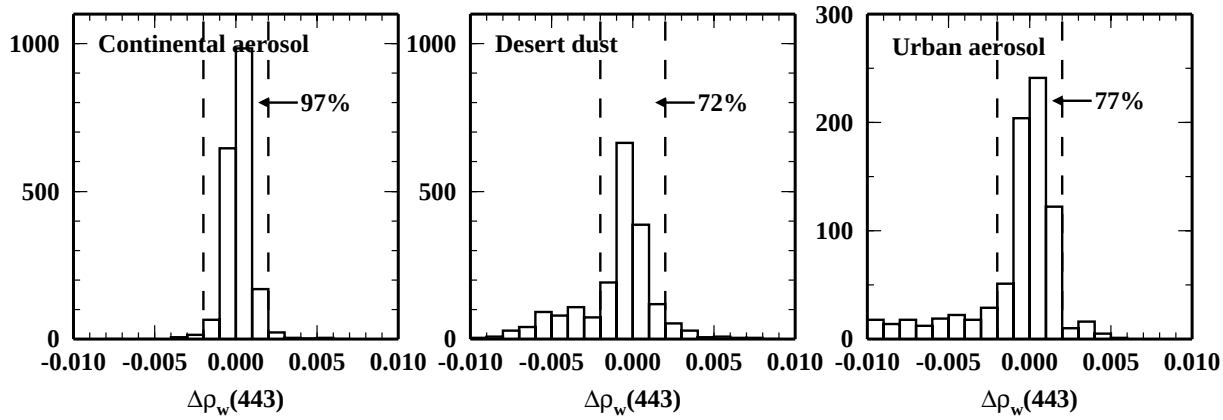

Fig. 5. Histogram of the error in the retrieved marine reflectance at 443 nm, and for the three "non-standard" aerosol assemblages, as indicated. The results for the four aerosol optical thicknesses, the three "mixing ratios" (the proportion of aerosols within the boundary layer and the free troposphere), and various geometries, are here pooled together (1920 cases for each aerosol assemblage). The percentages indicated correspond to the errors within ±0.002 in reflectance.

3 MERIS radiometric calibration

The radiometric calibration of MERIS is performed with the use of two on-board sun-lit radiometric (white) calibration diffuser plates. These Spectralon™ plates provide a uniform illumination signal over the entire field of view of the instrument. They have been extensively characterised on-ground using a dedicated BDRF bench to an absolute accuracy of better than 1%. This performance estimate was confirmed by a round-robin exercise performed with other laboratories (*i.e.*, NIST, NASA, NPL).

The plates have been exposed to a post-production processing in order to reduce the degradation (browning) of its scattering characteristics to space environment. According to on-ground simulations, the degradation over the mission lifetime should be minimal**.** However, as a means of verification, MERIS makes use of both its on-board diffusers to monitor the degradation of the frequently used (every 15 days) diffuser-1 by comparing it with the results from diffuser-2 which is deployed only every 3 months.

The results of this calibration scenario have been recently published (Bourg *et al*., 2002; Delwart *et al*., 2003).

4 The MOBY site and the MOBY buoy

4.1 Location

The MOBY site is located in the Hawaii archipelago, approximately 11 nautical miles offshore west of the Lanaï island (Fig. 6), where the water depth is about 1200 meters. This site is most of the time protected from large swells by the presence of the Lanaï islands, which is however sufficiently far so that environment effects (both on the satellite observations and on the water optical properties) are not affecting the mooring site. The conditions remain oligotrophic throughout the year (chlorophyll around 0.05-0.17 mg(Chl) m^{-3}). Regular cruises are carried out, during which complementary bio-optical and radiometric data are collected, among other things for the validation of the MOBY determinations of the water-leaving radiance. Additional details about the project and the buoy can be found in Clark *et al*. (1997, 2002).

4.2 Instrumentation

4.2.1 MOBY and the Marine Optical System (MOS)

MOBY is a 12 m spar buoy (including the lower instrument bay) uniquely designed as an optical bench for measurements of $E_d(z,\lambda)$ and $L_u(z,\lambda)$ at depths of 1 m, 5 m, 9 m, and 12 m (Fig. 7). A schematic illustration of the MOBY system's sensors, operations, and communications are shown in Fig. 8. Meteorological sensors for wind speed, wind direction, air temperature, relative humidity, and barometric pressure are mounted on the main mooring buoy.

The Marine Optical System (MOS), the heart of MOBY, consists of two single-grating CCD spectrographs connected via an optical multiplexer and fiber optic cables to the $E_d(z,\lambda)$ and $L_u(z,\lambda)$ optical heads mounted at the ends of the buoy's three standoff arms (Figs. 7 and 8). To provide low-loss transmission at ultraviolet wavelengths, 1 mm diameter silica fiber optic cables are used to connect the optical heads to MOS. $L_u(12,\lambda)$, at z = 12 m, is measured through a window in the bottom of the MOS housing itself. A seventh fiber optic cable connects a surface irradiance, $E_s(\lambda)$, cosine collector, mounted at the top of the MOBY above-water mast, to the spectrographs. Each pair of in-water optical heads is mounted on a standoff arm to minimize radiometric artifacts due to shadows or reflections from the buoy.

The MOS system elements and optical layout are illustrated schematically in Fig. 9. Light from an $L_u(z,\lambda)$, $E_d(z,\lambda)$, or $E_s(\lambda)$ head entering the spectrograph package via its fiber optic cable and the

multiplexer is directed to a dichroic mirror that reflects light at wavelengths between 350 nm and 630 nm into one (blue) grating spectrograph and transmits wavelengths greater than 630 nm to the other (red) spectrograph. The MOS spectrograph package is mounted in MOBY's lower instrument bay (Fig. 7), at a depth of approximately 12 m, primarily to isolate the package from the shock and vibration that surface waves inflict on the upper instrument bay. The deeper location also facilitates heat dissipation from the thermoelectric coolers used to maintain the operating temperature of the CCD arrays, and $L_u(12,\lambda)$ may be measured through the MOS optical window at the very bottom of the MOBY spar. Even more critically, the high current draw of the MOS requires that it be located close to the batteries, which themselves must be placed at the bottom of the spar to act as stabilizing ballast.

The elements defining the spectral radiometric characteristics of each of the spectrographs are its entrance slit, holographic grating, and cooled CCD detector array (Fig. 9). For the blue spectrograph (350 nm to 630 nm), the FWHP bandpass of the spectral slit response function centered at any given wavelength is approximately 2 nm, and the 512 element detector array is designed to sample at approximately a 0.6 nm interval. The MOS was designed with such high spectral resolution in order for it to support vicarious calibrations of a variety of different satellite ocean color sensors. By measuring *in situ* spectra of $L_u(\lambda,z)$ at this resolution, it is practical to compute band-averaged values of $L_{WN}(\lambda)$ that are appropriately weighted for any of these satellite ocean color sensors.

4.2.2 Ancillary Measurements on MOBY

Additional ancillary sensors are installed in the MOS package. Internal housing and CCD array temperatures are measured as indicators of performance quality and may be used in applying radiometric calibration factors to the data. A high precision pressure transducer is installed on the top radiometric arm to determine depth variations $[z(t) - z_P]$ about its nominal reference depth z_P (fixed by its location on the spar) during each radiometric measurement sequence. A separate temperature sensor monitors the temperature of the pressure transducer to minimize uncertainties in the depth determinations.

Tilt sensors within the MOS package are used to determine the 2-axis orientation (pitch and yaw) of the MOBY spar relative to the local vertical. A flux gate compass, also installed within the MOS package, is used to determine the direction (magnetic) in which the radiometric sensor arms extend out from the spar. The relative angle between the spar pointing azimuth and the solar azimuth are used to detect measurement geometries in which the irradiance and radiance collectors may be influenced by shadows, or reflections, from the main MOBY structure and will be used for radiance distribution corrections.

A typical MOBY deployment is shown in Fig. 10.

4.2.3 Mooring Buoy Measurements

Sensors mounted on the mast of the mooring buoy measures photosynthetically available radiation (PAR), wind velocity, surface barometric pressure, air temperature, and relative humidity. Also, near surface sensors on this buoy measure water temperature, conductivity, beam attenuation and Chl *a* fluorescence.

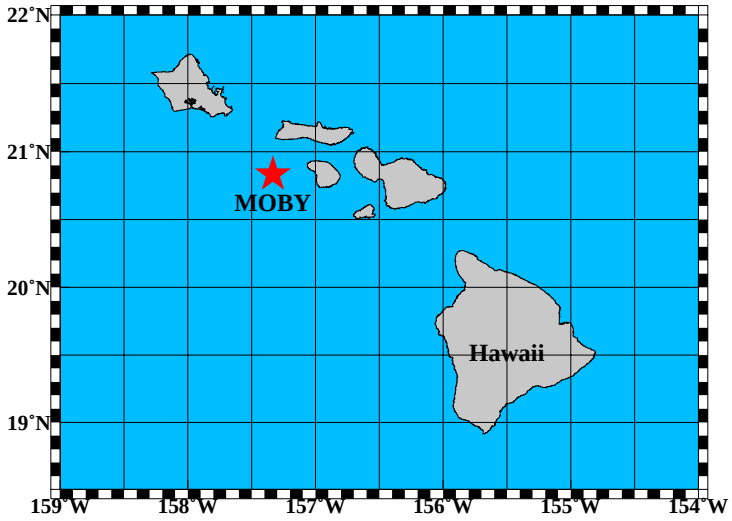

Fig. 6. Location of the MOBY site near Hawaii

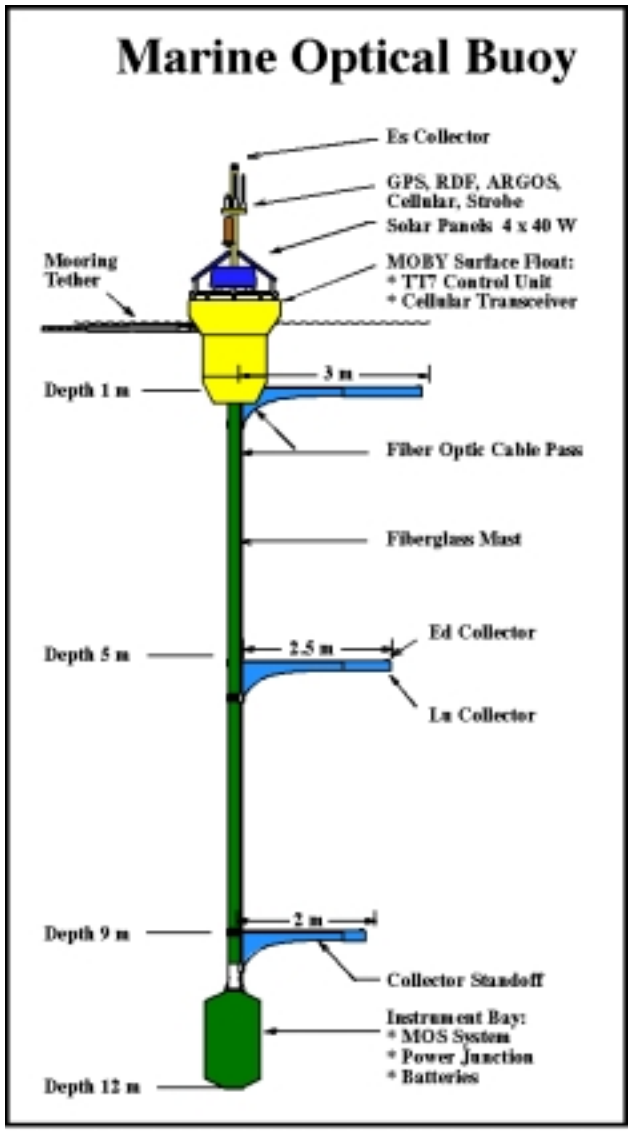

Fig. 7. The Marine Optical Buoy (MOBY)

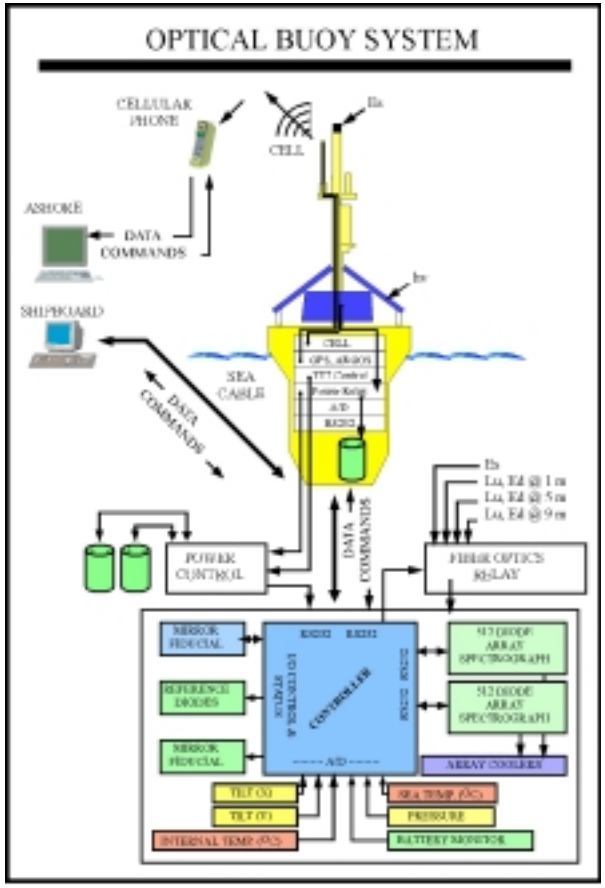

Fig. 8. A Schematic overview of the MOBY system elements

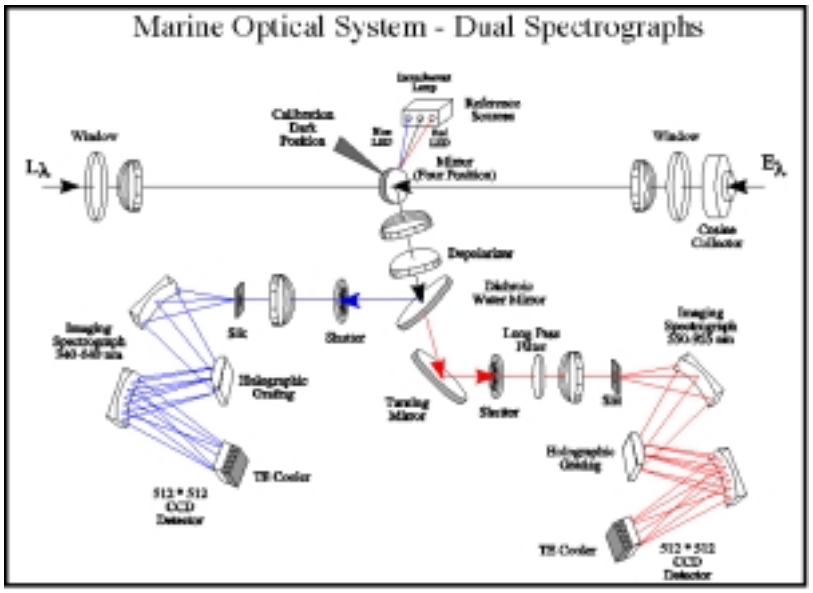

Fig. 9. A schematic diagram showing the optical design of the MOS spectrographs

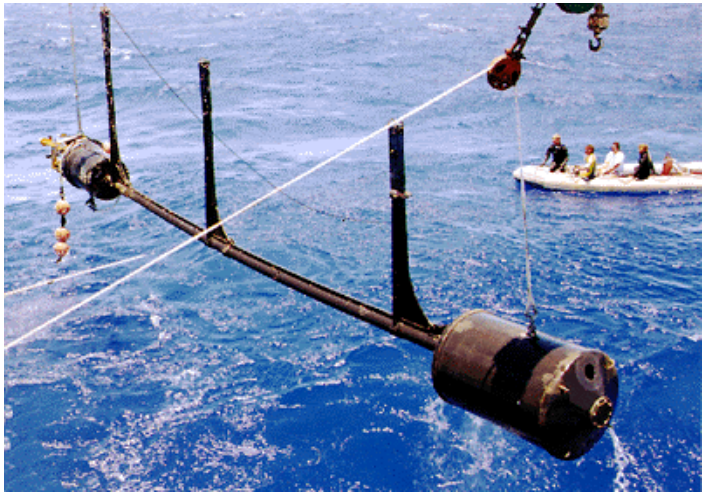

Fig. 10. A MOBY deployment

5 Match-up procedures

5.1 Relationships between the radiometric quantities

What is measured at three different depths by the MOBY buoy are upwelling radiances for the nadir direction, $L_u(z)$, from 350 to 950 nm by steps of about 0.6 to 1 nm, from which the upwelling radiance at null depth ("just below the sea surface") is obtained as (the wavelength, λ, is omitted in the following equations) :

$$L_u(0^-, \theta_v=0) = L_u(z)\, e^{(K_L z)} \quad (4)$$

Where z is depth, and K_L is the attenuation coefficient for the upwelling radiance computed from the measurements of $L_u(z)$ collected by the instruments installed at the different depths on the buoy.

The water-leaving radiance, L_w, is then computed :

$$L_w(\theta_v=0)) = [(1 - \rho) / n^2]\, L_u(0^-, \theta_v=0) \quad (5)$$

where a constant value of 0.543 is set to the $[(1 - \rho) / n^2]$ factor accounting for the transmission across the water-air interface.

These water-leaving radiances are still for the nadir direction, and they are normalised *sensu* Gordon and Clark (1981), *i.e.* :

$$[L_w]_N(\theta_v=0) = L_w(\theta_v=0)) / (\varepsilon_c\ \cos(\theta_s)\, t_d(\theta_s))^2 \quad (6)$$

where θ_s is the sun zenith angle, ε_c is a correction of the extraterrestrial solar irradiance accounting for the eccentricity of the Earth orbit, and t_d is the diffuse transmittance of the atmosphere for the angle θ_s (sun-pixel path). The diffuse transmittance t_d is computed as :

$$t_d(\theta_s) = \exp(-(\tau_r/2 + \tau_{oz}) / \cos(\theta_s)) \quad (7)$$

where τ_r and τ_{oz} are the Rayleigh and ozone optical thicknesses, respectively, and the correction factor ε_c is computed from the eccentricity of the Earth orbit (e = 0.0167) and from the day number as :

$$\varepsilon_c = \left(1 + e \cos\left(\frac{2\pi(D-3)}{365}\right)\right)^2 \quad (8)$$

The spectral normalised water-leaving radiances are then used to produce band-averaged values (for the MERIS bands in our case), following (using notation in Clark *et al*., 2002) :

[2] In case the downwelling irradiance above the surface is measured, it can be used for the normalisation, leading then to rewrite Eq. (6) as : $[L_w]_N(\theta_v=0) = F_0\, L_w(\theta_v=0)) / E_d(0^+, \theta_s)$

$$[L_w]_N^{Meris}(\bar{\lambda}_i) = \frac{\int_0^{\infty} r_n^s(\lambda,\bar{\lambda}_i)\,[L_w]_N(\lambda)\,d\lambda}{\int_0^{\infty} r_n^s(\lambda,\bar{\lambda}_i)\;d\lambda} \quad (9)$$

where the $r_n^s(\lambda,\bar{\lambda}_i)$ are the normalised relative spectral response functions of the MERIS bands (see appendix 2).

The MERIS reflectances are defined as :

$$\rho'_w(\theta_s, \theta_v, \Delta\phi) = \pi L_w(\theta_s, \theta_v, \Delta\phi) / E_d(0^+, \theta_s) \quad (10)$$

where $E_d(0^+, \theta_s)$ is the downwelling irradiance just above the sea surface. Eq. (10) is rewritten as :

$$\rho'_w(\theta_s, \theta_v, \Delta\phi) = \pi L_w(\theta_s, \theta_v, \Delta\phi) / (\varepsilon_c\ F_0\ \cos(\theta_s)\ t_d(\theta_s)) \quad (11)$$

where F_0 is the mean extraterrestrial irradiance.

The water-leaving radiance can be written as (*e.g.*, Morel and Gentili 1996) :

$$L_w(\theta_s,\theta_v,\Delta\phi) = E_d(0^+)\,\Re(\theta')\,\frac{f(\theta_s)}{Q(\theta_s,\theta',\Delta\phi)}\,\frac{b_b}{a} \quad = \quad (\varepsilon_c F_0 \mu_s t_d(\theta_s))\,\Re(\theta')\,\frac{f(\theta_s)}{Q(\theta_s,\theta',\Delta\phi)}\,\frac{b_b}{a} \quad (12)$$

where θ' is the viewing angle below the surface ($\theta' = \sin^{-1}(\sin(\theta_v) / 1.34)$), and where the gothic R ($\Re$) is a factor accounting for all reflection and transmission effects at the air-sea interface. It is equal to (subscript 0 when $\theta' = 0$) :

$$\Re(\theta') = \left[\frac{(1-\bar{\rho})}{(1-\bar{r}R)}\,\frac{(1-\rho_F(\theta'))}{n^2}\right] \quad (13)$$

where n is the refractive index of water, $\rho_F(\theta)$ is the Fresnel reflection coefficient for incident angle θ, $\bar{\rho}$ is the mean reflection coefficient for the downwelling irradiance at the sea surface, and $\bar{r}$ is the average reflection for upwelling irradiance at the water-air interface.

Combining Eqs. (6), (11), (12) and (13), the relationship between the normalised water-leaving radiance produced by the MOBY project (necessarily at nadir : $[L_w]_N(\theta_v=0)$) and the MERIS water-leaving reflectance (for any viewing angle, $\rho'_w(\theta_s, \theta_v, \Delta\phi)$) is :

$$\rho'_w(\theta_{s,sat},\theta_v,\Delta\phi) = [L_w]_N(\theta_v=0)\left[\frac{\pi}{F_0}\right]\left[\frac{\Re(\theta')}{\Re_0}\right]\left[\frac{f(\theta_{s,sat})}{Q(\theta_{s,sat},\theta',\Delta\phi)}\right]\left[\frac{f(\theta_{s,moby})}{Q(\theta_{s,moby},\theta'=0,\Delta\phi=0)}\right]^{-1} \quad (14)$$

where $\theta_{s,sat}$ and $\theta_{s,moby}$ are the sun zenith angles at the time of the satellite pass and at the time of the MOBY measurement, respectively.

5.2 Practical aspects

5.2.1 MERIS data processing

The MERIS level 1b data used in the present study have been systematically processed to the level 2 by using in parallel both the LOV breadboard and the MERIS prototype. The former is the code that has been progressively developed at the LOV ("in house code") during the definition and test phase of the MERIS atmospheric correction algorithms. It is a transcription of MERIS ATBDs 2.7 and 2.9. The latter is the code that has been developed at ACRI-st, based on ATBDs 2.7 and 2.9, on the "Detailed Processing Model" established in collaboration between ACRI-st and the LOV, and on the LOV breadboard. This MERIS prototype, along with the specification documents that were produced by ACRI-st, is the basis of the operational MERIS ground segment ("MEGS"). Using the prototype is strictly identical to using the operational ground segment. As soon as the ESRIN operational ground segment will be able to provide the necessary level-2 products, they will be used instead of the prototype results in order to produce a more final version of the present report.

The parallel use of the breadboard and the prototype allows a permanent verification of any changes incorporated in either of these two codes. It has been the basis of what has been referred to as the "algorithm verification" that takes place since fall of 2002, when MERIS level 1b data begun to be distributed to the calibration/validation P.I.s.

Results are only shown here for the prototype processing, as far as they are extremely close to the results obtained with the breadboard processing.

5.2.2 Matchup procedure

For each MERIS scene corresponding to an overpass of the MOBY buoy, the pixel the closest to the buoy is selected. The distance is computed as the square root of the sum of the squares of the latitude and longitude differences between the pixel and the MOBY position (latitude and longitude have units of decimal degrees). Then, mean quantities and standard deviations are computed for a 5 by 5 box centred on this pixel. Extraction from the prototype level 2 are performed using the "MerisView" software package developed at ACRI-st, while it is performed with in-house codes for the LOV breadboard outputs.

The resulting quantities are then compared to the MOBY-derived reflectances, after the geometric corrections described in the section 4.1 have been applied.

Simple differences (X-Y) as well as unbiased percent differences "UPD", *i.e.*, 100 x (X – Y) / ((X + Y) / 2) between the MERIS-derived reflectances and the MOBY-derived reflectances are also computed.

6 The data used for the vicarious radiometric calibration experiments

6.1 MERIS data

Two sets of MERIS images have been assembled. The first one comprises 18 overpasses for which the MOBY site is within the western half of the swath, *i.e.*, out of the effect of sun glint. The second set comprises 13 overpasses for which the MOBY site is within the eastern half of the swath, *i.e.*, within the area contaminated by sun glint. The two lists are given below.

Table 1 : list of the MERIS filenames for situations where the MOBY buoy is outside of the glint influence

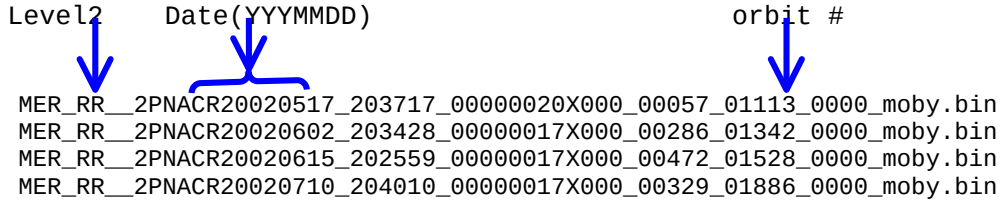

MER_RR__2PNACR20020723_203138_00000017X000_00014_02072_0000_moby.bin
MER_RR__2PNACR20020805_202306_00000020X000_00200_02258_0000_moby.bin
MER_RR__2PNACR20020827_203138_00000017X000_00014_02573_0000_moby.bin
MER_RR__2PNACR20020912_202848_00000017X000_00243_02802_0000_moby.bin
MER_RR__2PNACR20020918_204010_00000017X000_00329_02888_0000_moby.bin
MER_RR__2PNACR20021014_202306_00000020X000_00200_03260_0000_moby.bin
MER_RR__2PNACR20021020_203428_00000017X000_00286_03346_0000_moby.bin
MER_RR__2PNACR20021030_202016_00000017X000_00429_03489_0000_moby.bin
MER_RR__2PNACR20021124_203428_00000017X000_00286_03847_0000_moby.bin
MER_RR__2PNACR20021127_204010_00000017X000_00329_03890_0000_moby.bin
MER_RR__2PNACR20021204_202016_00000017X000_00429_03990_0000_moby.bin
MER_RR__2PNACR20021210_203138_00000017X000_00014_04076_0000_moby.bin
MER_RR__2PNACR20021213_203717_00000020X000_00057_04119_0000_moby.bin
MER_RR__2PNACR20021223_202306_00000020X000_00200_04262_0000_moby.bin

Table 2 : list of the MERIS filenames for situations where the MOBY buoy is within the glint influence

MER_RR__2PNACR20020523_204802_00000090X000_00143_01199_0000_moby.bin
MER_RR__2PNACR20020614_205631_00000090X000_00458_01514_0000_moby.bin
MER_RR__2PNACR20020630_205341_00000090X000_00186_01743_0000_moby.bin
MER_RR__2PNACR20020801_204802_00000090X000_00143_02201_0000_moby.bin
MER_RR__2PNACR20020804_205341_00000090X000_00186_02244_0000_moby.bin
MER_RR__2PNACR20020817_204512_00000090X000_00372_02430_0000_moby.bin
MER_RR__2PNACR20020823_205631_00000090X000_00458_02516_0000_moby.bin
MER_RR__2PNACR20020921_204512_00000090X000_00372_02931_0000_moby.bin
MER_RR__2PNACR20021010_204802_00000090X000_00143_03203_0000_moby.bin
MER_RR__2PNACR20021013_205341_00000090X000_00186_03246_0000_moby.bin
MER_RR__2PNACR20021130_204512_00000090X000_00372_03933_0000_moby.bin
MER_RR__2PNACR20021219_204802_00000090X000_00143_04205_0000_moby.bin
MER_RR__2PNACR20021222_205341_00000090X000_00186_04248_0000_moby.bin

6.2 MOBY water-leaving radiances

The two tables below provide the MOBY water-leaving radiances corresponding to the MERIS overpasses, with several values each day (from 2 to 6 values). These different values correspond to the different ways of determining the upwelling radiance at null depth (Eq. 5), which can be based on several combination of the measurements collected from the buoy horizontal arms at 2, 5 and 9 meters.

Table 3 : List of the MOBY water-leaving radiances determinations used in the match-up exercise. These situations correspond to the "non glint" conditions of Table 1.

filename	year	day	Lw(412)	Lw(443)	Lw(490)	Lw(510)	Lw(560)	Lw(620)	Lw(665)	Lw(681)	Lw(708)
219_meri1.txt	2002	137	1.4930	1.3443	0.9955	0.5549	0.2205	0.0198	0.0064	0.0054	0.0009
219_meri3.txt	2002	137	1.4649	1.3149	0.9806	0.5540	0.2233	0.0291	0.0143	0.0126	0.0038
220_meri1.txt	2002	153	1.3919	1.2225	0.9062	0.5017	0.1925	0.0190	0.0060	0.0051	0.0009
220_meri2.txt	2002	153	1.6097	1.4128	1.0571	0.5943	0.2302	0.0257	0.0099	0.0085	0.0021
220_meri3.txt	2002	153	1.5993	1.3774	1.0001	0.5411	0.1971	0.0153	0.0036	0.0031	0.0004
220_meri5.txt	2002	153	1.4813	1.3011	0.9619	0.5409	0.2121	0.0285	0.0120	0.0105	0.0031
220_meri1.txt	2002	166	1.0112	0.9339	0.7005	0.3958	0.1511	0.0138	0.0045	0.0041	0.0007
220_meri2.txt	2002	166	1.4533	1.3269	0.9727	0.5468	0.2083	0.0243	0.0093	0.0080	0.0020
220_meri3.txt	2002	166	1.4142	1.2946	0.9541	0.5282	0.1924	0.0151	0.0036	0.0030	0.0004
220_meri5.txt	2002	166	1.0604	0.9837	0.7419	0.4164	0.1585	0.0206	0.0085	0.0074	0.0019
220_meri.txt	2002	191	1.5587	1.3031	0.8959	0.4733	0.1730	0.0149	0.0041	0.0037	0.0006
220_meri1.txt	2002	191	1.5938	1.3503	0.9292	0.4904	0.1824	0.0179	0.0054	0.0049	0.0009
220_meri4.txt	2002	191	1.6189	1.3769	0.9640	0.5206	0.1963	0.0257	0.0111	0.0099	0.0028
220_meri5.txt	2002	191	1.5076	1.2880	0.9021	0.4862	0.1841	0.0245	0.0106	0.0095	0.0027
220_meri.txt	2002	204	1.8442	1.5200	1.0106	0.5244	0.1902	0.0189	0.0059	0.0050	0.0008
220_meri1.txt	2002	204	1.7557	1.4435	0.9704	0.4985	0.1744	0.0152	0.0041	0.0037	0.0006
220_meri2.txt	2002	204	1.9354	1.5876	1.0659	0.5570	0.2001	0.0226	0.0093	0.0082	0.0021
220_meri3.txt	2002	204	1.9319	1.5812	1.0634	0.5623	0.2071	0.0180	0.0048	0.0042	0.0006
220_meri4.txt	2002	204	1.8739	1.5565	1.0515	0.5581	0.2072	0.0273	0.0124	0.0110	0.0033
220_meri5.txt	2002	204	1.7071	1.4147	0.9665	0.5151	0.1919	0.0252	0.0111	0.0098	0.0029
220_meri.txt	2002	217	1.7186	1.4441	1.0104	0.5613	0.2210	0.0209	0.0063	0.0051	0.0008
220_meri4.txt	2002	217	1.7480	1.4374	0.9845	0.5278	0.1992	0.0272	0.0118	0.0102	0.0031
220_meri.txt	2002	239	1.7393	1.4339	0.9861	0.5390	0.2069	0.0202	0.0056	0.0048	0.0009
220_meri1.txt	2002	236	1.5746	1.3073	0.9034	0.4859	0.1846	0.0179	0.0054	0.0050	0.0009
220_meri4.txt	2002	239	1.7702	1.4632	1.0015	0.5400	0.2069	0.0303	0.0133	0.0117	0.0037
220_meri5.txt	2002	236	1.6834	1.4087	0.9760	0.5275	0.2003	0.0267	0.0118	0.0105	0.0031
220_meri1.txt	2002	255	1.6195	1.3488	0.9450	0.5105	0.1933	0.0186	0.0055	0.0050	0.0008
220_meri2.txt	2002	255	1.8113	1.5030	1.0578	0.5785	0.2213	0.0282	0.0118	0.0103	0.0029
220_meri3.txt	2002	255	1.8067	1.4924	1.0430	0.5719	0.2206	0.0210	0.0061	0.0052	0.0008
220_meri5.txt	2002	255	1.6170	1.3504	0.9540	0.5236	0.2023	0.0279	0.0121	0.0109	0.0033
220_meri1.txt	2002	261	1.1851	1.0283	0.8077	0.4696	0.1913	0.0196	0.0057	0.0055	0.0008
220_meri2.txt	2002	261	1.5701	1.3393	1.0061	0.5741	0.2287	0.0317	0.0138	0.0120	0.0038
220_meri3.txt	2002	261	1.4934	1.2749	0.9714	0.5545	0.2208	0.0227	0.0074	0.0065	0.0010
220_meri5.txt	2002	261	1.2844	1.1176	0.8809	0.5173	0.2109	0.0293	0.0137	0.0124	0.0039
221_meri.txt	2002	303	1.2536	1.0713	0.7525	0.4052	0.1515	0.0134	0.0040	0.0039	0.0007
221_meri2.txt	2002	303	1.2731	1.0874	0.7739	0.4222	0.1600	0.0212	0.0102	0.0093	0.0028
221_meri1.txt	2002	328	0.9170	0.8188	0.6107	0.3427	0.1337	0.0168	0.0078	0.0072	0.0021
221_meri.txt	2002	331	0.9591	0.8368	0.6231	0.3496	0.1343	0.0114	0.0037	0.0036	0.0007
221_meri2.txt	2002	331	0.9782	0.8603	0.6462	0.3651	0.1450	0.0199	0.0092	0.0084	0.0026
221_meri.txt	2002	338	1.0011	0.8666	0.6039	0.3164	0.1116	0.0083	0.0023	0.0021	0.0004
221_meri1.txt	2002	338	0.9606	0.8450	0.6326	0.3597	0.1422	0.0210	0.0110	0.0098	0.0036
221_meri2.txt	2002	338	1.0180	0.8847	0.6345	0.3429	0.1288	0.0183	0.0090	0.0081	0.0026
221_meri.txt	2002	344	0.8687	0.7622	0.5756	0.3239	0.1262	0.0110	0.0036	0.0039	0.0007
221_meri2.txt	2002	344	0.9192	0.7990	0.6019	0.3419	0.1345	0.0185	0.0099	0.0093	0.0032
221_meri.txt	2002	347	0.9116	0.8056	0.5794	0.3109	0.1151	0.0093	0.0031	0.0031	0.0006
221_meri2.txt	2002	347	0.9737	0.8560	0.6134	0.3314	0.1258	0.0167	0.0077	0.0070	0.0020
221_meri1.txt	2002	357	0.9318	0.8297	0.6148	0.3396	0.1300	0.0164	0.0077	0.0071	0.0020

Table 4 : List of the MOBY water-leaving radiances determinations used in the match-up exercise. These situations correspond to the " glint" conditions of Table 2.

filename	year	day	Lw(412)	Lw(443)	Lw(490)	Lw(510)	Lw(560)	Lw(620)	Lw(665)	Lw(681)	Lw(708)
219_meri.txt	2002	143	1.6342	1.4186	0.9972	0.5348	0.1901	0.0135	0.0036	0.0032	0.0005
219_meri2.txt	2002	143	1.7272	1.4960	1.0500	0.5719	0.2156	0.0253	0.0108	0.0095	0.0026
220_meri2.txt	2002	165	1.4136	1.3032	0.9613	0.5367	0.2055	0.0259	0.0111	0.0099	0.0025
220_meri3.txt	2002	165	1.3909	1.2761	0.9278	0.5094	0.1895	0.0150	0.0040	0.0036	0.0005
220_meri.txt	2002	181	1.8706	1.5382	1.0266	0.5323	0.1923	0.0187	0.0057	0.0047	0.0008
220_meri4.txt	2002	181	1.8528	1.5367	1.0392	0.5479	0.2039	0.0272	0.0120	0.0106	0.0032
220_meri1.txt	2002	213	1.6887	1.4029	0.9617	0.5049	0.1829	0.0166	0.0051	0.0045	0.0007
220_meri2.txt	2002	213	1.8773	1.5565	1.0746	0.5726	0.2108	0.0233	0.0084	0.0074	0.0017
220_meri3.txt	2002	213	1.8624	1.5403	1.0599	0.5655	0.2094	0.0197	0.0057	0.0048	0.0007
220_meri5.txt	2002	213	1.6673	1.3904	0.9663	0.5209	0.1974	0.0264	0.0113	0.0101	0.0029
220_meri.txt	2002	216	1.7237	1.4403	1.0072	0.5442	0.2039	0.0191	0.0057	0.0050	0.0008
220_meri1.txt	2002	216	1.7008	1.3767	0.9448	0.5008	0.1856	0.0177	0.0054	0.0047	0.0008
220_meri4.txt	2002	216	1.6747	1.4160	1.0020	0.5490	0.2097	0.0273	0.0118	0.0104	0.0029
220_meri5.txt	2002	216	1.7051	1.4095	0.9846	0.5359	0.2058	0.0287	0.0129	0.0114	0.0036
220_meri1.txt	2002	229	1.5207	1.2866	0.9005	0.4789	0.1763	0.0182	0.0057	0.0050	0.0009
220_meri2.txt	2002	229	1.9372	1.6157	1.1133	0.5984	0.2239	0.0291	0.0130	0.0112	0.0033
220_meri3.txt	2002	229	1.9969	1.6584	1.1330	0.5966	0.2169	0.0189	0.0048	0.0041	0.0005
220_meri5.txt	2002	229	1.5742	1.3300	0.9433	0.5225	0.2014	0.0274	0.0125	0.0110	0.0034
220_meri.txt	2002	235	1.8606	1.5317	1.0358	0.5492	0.2044	0.0192	0.0056	0.0047	0.0008
220_meri4.txt	2002	235	1.7922	1.4963	1.0290	0.5542	0.2107	0.0284	0.0124	0.0110	0.0034
220_meri.txt	2002	264	1.6607	1.4234	0.9606	0.5045	0.1895	0.0176	0.0052	0.0045	0.0007
220_meri1.txt	2002	264	1.4926	1.2731	0.8756	0.4654	0.1713	0.0168	0.0049	0.0042	0.0007
220_meri2.txt	2002	264	1.8639	1.5756	1.0708	0.5722	0.2145	0.0280	0.0119	0.0103	0.0030
220_meri3.txt	2002	264	1.9463	1.6293	1.0934	0.5772	0.2128	0.0203	0.0058	0.0047	0.0007
220_meri4.txt	2002	264	1.5889	1.3684	0.9386	0.4971	0.1871	0.0245	0.0105	0.0092	0.0026
220_meri5.txt	2002	264	1.5227	1.3097	0.9272	0.5070	0.1918	0.0248	0.0109	0.0095	0.0027
220_meri.txt	2002	283	1.1454	0.9914	0.7648	0.4454	0.1758	0.0152	0.0045	0.0041	0.0005
220_meri1.txt	2002	283	1.1108	0.9949	0.7569	0.4257	0.1655	0.0159	0.0050	0.0047	0.0008
220_meri4.txt	2002	283	1.1701	1.0016	0.7591	0.4400	0.1754	0.0240	0.0106	0.0095	0.0029
220_meri5.txt	2002	283	1.1005	1.0095	0.7863	0.4566	0.1818	0.0250	0.0119	0.0107	0.0033
221_meri1.txt	2002	286	1.1860	1.0435	0.7754	0.4440	0.1767	0.0255	0.0129	0.0116	0.0042
221_meri.txt	2002	334	0.8185	0.7509	0.6026	0.3575	0.1424	0.0127	0.0042	0.0042	0.0008
221_meri1.txt	2002	334	0.9574	0.8184	0.6307	0.3686	0.1516	0.0225	0.0120	0.0113	0.0040
221_meri2.txt	2002	334	0.8340	0.7570	0.5989	0.3522	0.1407	0.0188	0.0094	0.0086	0.0026
221_meri.txt	2002	353	0.8642	0.7734	0.5601	0.2988	0.1101	0.0091	0.0032	0.0032	0.0006
221_meri2.txt	2002	353	0.9196	0.8179	0.5930	0.3207	0.1219	0.0161	0.0081	0.0074	0.0023
221_meri.txt	2002	356	0.8136	0.7351	0.5545	0.3062	0.1159	0.0100	0.0032	0.0032	0.0006
221_meri1.txt	2002	356	0.9309	0.8264	0.6047	0.3317	0.1259	0.0163	0.0079	0.0072	0.0021
221_meri2.txt	2002	356	0.8360	0.7470	0.5639	0.3177	0.1245	0.0164	0.0077	0.0071	0.0020

6.3 Auxiliary data

The wind speed modulus (m s^{-1}), the total ozone content of the atmosphere (DU) and the atmospheric pressure (hPa), which are inputs to the atmospheric correction algorithms, are all taken from the MERIS ECMWF auxiliary products.

7 Results

7.1 A first look to the chlorophyll images

The 31 MERIS scenes used here are displayed in Appendix 1, as chlorophyll concentration maps. The colour scale is on the top right corner of each image (all colours are distributed between extrema of 0.02 and 2 mg m^{-3}), and he location of the MOBY buoy is marked by a red cross.

At first glance, the chlorophyll images produced through the MERIS prototype are about perfect. The chlorophyll values are exactly in the expected range for the MOBY area (from 0.03 to 0.2 mg m^{-3}, except very near the Hawaii archipelago islands where the concentrations may reach about 0.5 mg m^{-3}), and no major artefacts appear. Subtle changes in the chlorophyll concentration are coherently mapped, *i.e.*, small-scale ocean structures are revealed in this generally oligotrophic area, thanks to the high radiometric accuracy of MERIS.

A closer look reveals some peculiar, non-systematic, features, which may however indicate the need for some improvements of the level 1b and level 2 processing :

- Camera limits remain here and there visible, mostly between camera 1 and 2 at the East of the swath (*e.g.*, images of the 19th and 22nd of December).
- Clouds are not fully identified as such, and the corresponding pixels exhibit mistakenly large or low chlorophyll concentrations. This phenomenon is likely to occur as well in images of the aerosol optical thickness.
- Sun glint is covering more than half of the swath in certain circumstances, yet this is consubstantial with the instrument design. The implemented glint correction seems however correctly performed, so that no artefacts are seen when approaching the glint-covered area.
- A high frequency line-to-line noise sometimes appear (*e.g.*, images of the 19th and 22nd of December)

7.2 General match-up including all wavelengths

All matchup points, *i.e.*, all stations and all wavelengths, have been pooled together to draw a general matchup plot of the MERIS-derived reflectances *versus* the MOBY-derived reflectances. This is shown in Fig. 11(a) with linear axes, and in Fig. 11(b) in a log-log space. The latter is necessary to distinguish amongst the different wavelengths in the red part of the visible spectrum. These results have been obtained with the MERIS prototype.

The overall fit is extremely good, with a coefficient of regression of 0.986 and a slope of 1.04, indicating that the MERIS-derived reflectances would be slightly (*i.e.*, by 4%) overestimated. The intercept of the linear regression is negligible.

The scatter of the points is larger in the red part of the spectrum, yet it has to be kept in mind that the ocean reflectance there is particularly low for oligotrophic waters. Most of the scatter is within $2\ 10^{-4}$, *i.e.*, the predicted theoretical uncertainty of the atmospheric correction in this wavelength domain (as represented by the blue vertical bars on Fig. 11(b)). This number is also close to the "Noise Equivalent Reflectance (Ne$\Delta\rho$)" that was reached for the MERIS sensor, according to specifications.

7.3 Per-wavelength analysis

Fig. 12 shows the "unbiased percent differences" between the MERIS-derived reflectances and the MOBY-derived reflectances, for all 9 wavelengths considered here. The number given on top of each panel is the percentage of the UPD that are lower than ±5% and the number just below is for UPDs lower than ±10%. The about 4% positive bias is clearly appearing through this analysis, at least in the blue.

Note that the typical error of the atmospheric correction tends to be of the same magnitude than the marine signal itself when going beyond about 600 nm, so that the UPD is not the most relevant measure of the performance of the atmospheric correction in this domain. Therefore the absolute differences are

plotted in Fig. 13, again separately for each wavelength. They are mostly between plus or minus 4 10^{-3} at 412 and 443 nm, between plus or minus 2 10^{-3} at 490 and 510 nm, between plus or minus 1 10^{-3} at 560 and 620 nm, and finally between plus or minus 5 10^{-4} at 665, 681 and 708 nm. Again, the slight positive bias appears across the entire spectrum.

Having all errors within plus or minus 2 10^{-3} in the blue would indicate that the atmospheric correction behaves as requested. The results shown here indicate that some work is needed to reach this level of uncertainty. When pooling together the results for the first 6 wavelengths, however, it is shown (Fig. 14) that about 75% of the errors are already within the acceptable limits of plus or minus 2 10^{-3}.

7.4 Band ratios

Water-leaving reflectances are usually combined through band ratio algorithms, which are supposed to provide a geophysical quantity from this ratio, usually the chlorophyll concentration (*e.g.*, see O'Reilly *et al*., 2001).

Therefore we have plotted (Fig. 15) the 443/560 nm and the 490/560 nm band ratios, as derived either from the MERIS-derived reflectances or from the MOBY-derived reflectances. The dispersion of the results for individual wavelengths being small (Fig. 11), the ratio are also well correlated. They differ on average by less than 0.5.

The resulting differences in terms of the chlorophyll concentration are within the specifications, i.e., a maximum error of one class of the logarithm of the chlorophyll concentration (with 30 classes between 0.03 and 30 mg m^{-3}, se section 1).

7.5 Individual water-leaving reflectance spectra

The full set of 27 reflectance spectra is shown on Fig. 16, using in parallel a linear and a log scale, which are adapted for emphasising errors either in the blue or the red parts of the spectrum. The results from both the MERIS prototype and the LOV breadboard are shown.

One first result is that the spectral shape is usually extremely well reproduced for wavelengths below 600 nm. Even when a bias sometimes exists between the *in situ* and the MERIS-derived spectra, the change from one wavelength to another one is preserved.

The slight overestimation in the blue again appears quite clearly.

A sharp increase of the MERIS-derived water-leaving reflectance occurs between 665 nm and 681 nm, which is not present in the *in situ* determinations, where one can just observe a slight change in the decreasing slope of the reflectance. There is no clear indication, however, that this erroneous spectral change would be due primarily to an underestimation of the 665 nm reflectance or rather to an overestimation of the reflectance at 681 nm. Both situations occur approximately with the same probability. A practical consequence would be a large overestimate of the fluorescence signal in case it would be computed, as usually done, by drawing a baseline between the bands at 665 and 708 nm.

The reflectance is overestimated at 708 nm in approximately two third of the cases.

These last comments are to be cautiously considered because the signals in this spectral domain are extremely small in the clear oligotrophic waters of the MOBY site.

8 Conclusions

The MERIS atmospheric corrections and pigment retrieval algorithms are performing well above clear oceanic Case 1 waters. The errors in the retrieved water-leaving reflectances are within the specifications, and no major artefacts appear in the images. A slight bias of 4% has been identified, which remains to be confirmed by additional matchups at the same site and at other locations as well.

Some improvements are needed in terms of the smile correction, line-to-line high frequency noise, glint correction, clouds elimination, and accuracy of the atmospheric correction in the red part of the spectrum.

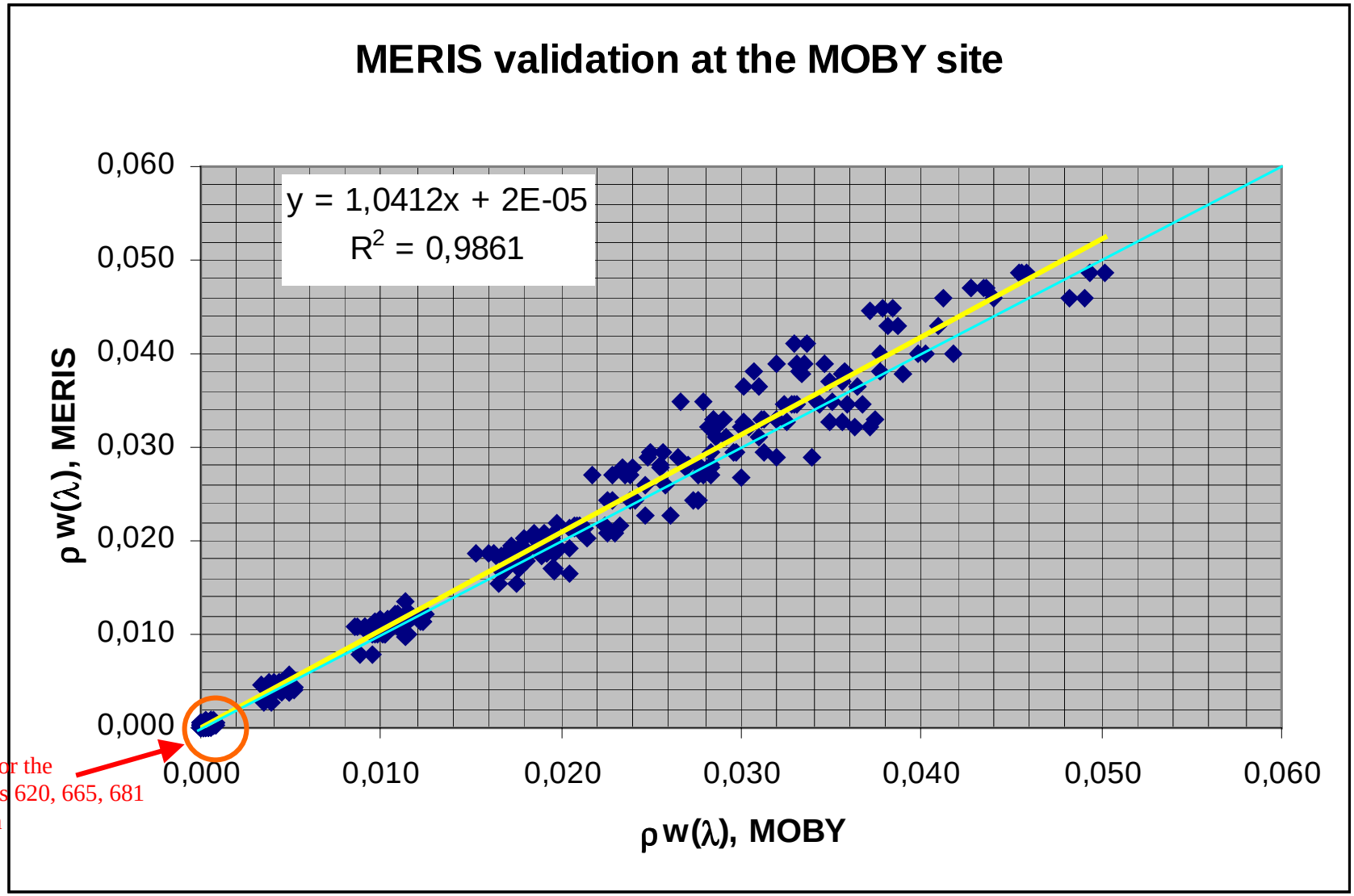

Fig. 11(a) : MERIS-derived water-leaving reflectances as a function of the same quantity as derived from the MOBY measurements. The yellow line is a linear fit to the data points (slope, intercept and the coefficient of regression in insert) and the blue line is simply the 1:1 line.

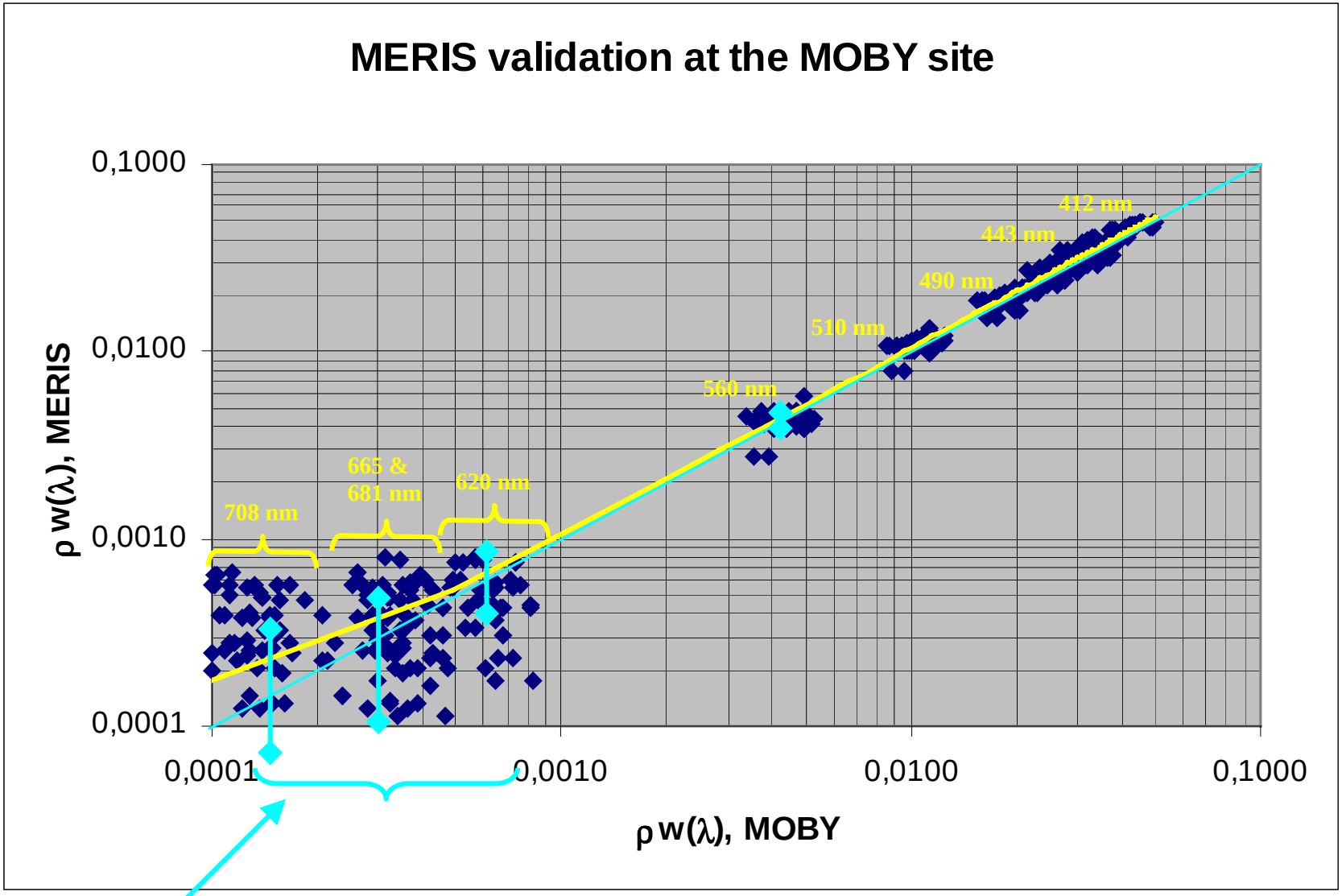

Fig. 11(b) : as in Fig. 11(a) but represented in the log-log space.

These light blue bars represent an error of about +/- 2 10^{-4} in terms of reflectance, centred onto the 1:1 line

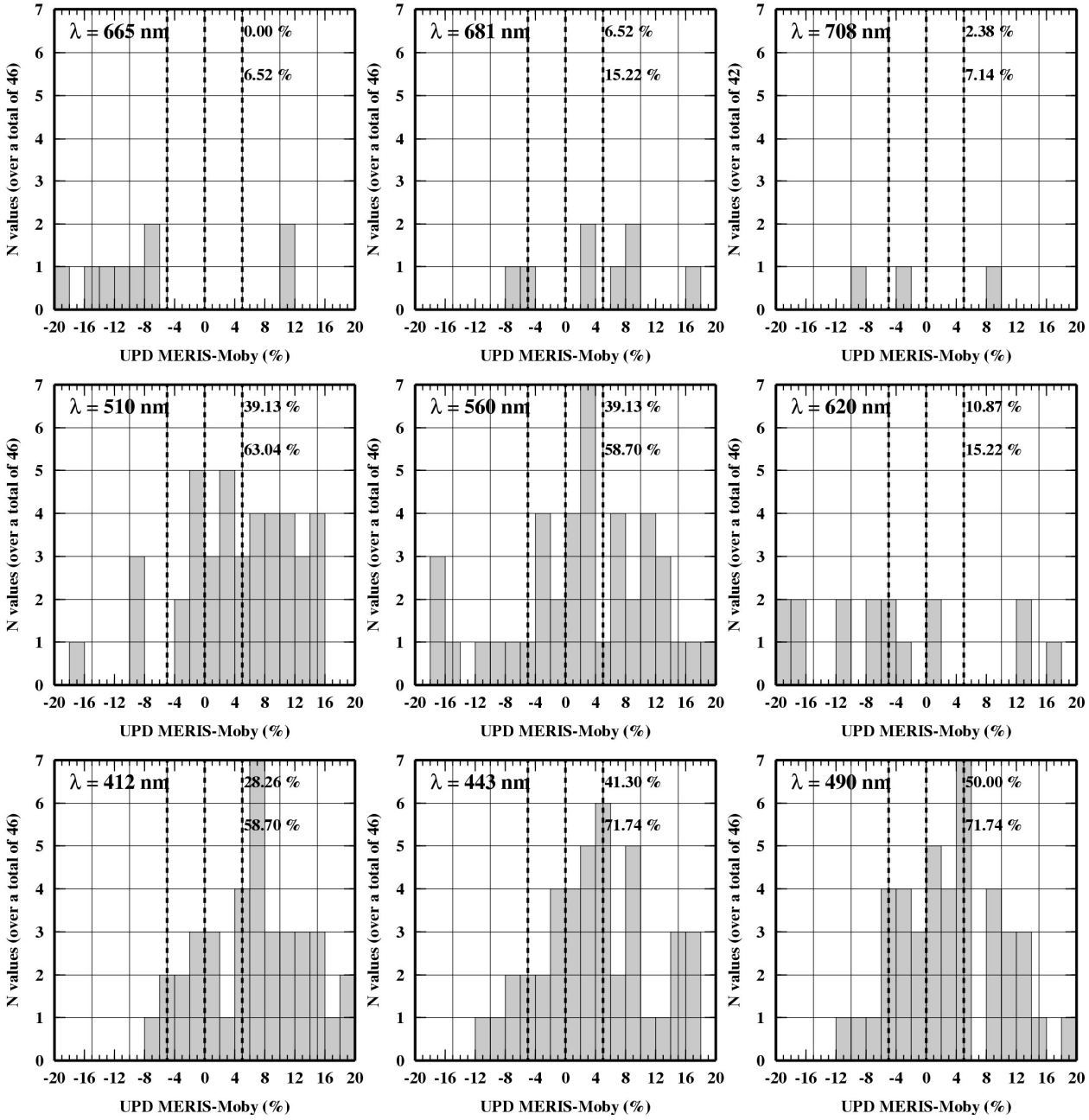

Fig. 12 : unbiased percent differences between the MERIS-derived and the MOBY-derived water-leaving reflectances (*i.e.*, 100*(X-Y)/((X+Y)/2)), for the wavelengths indicated.

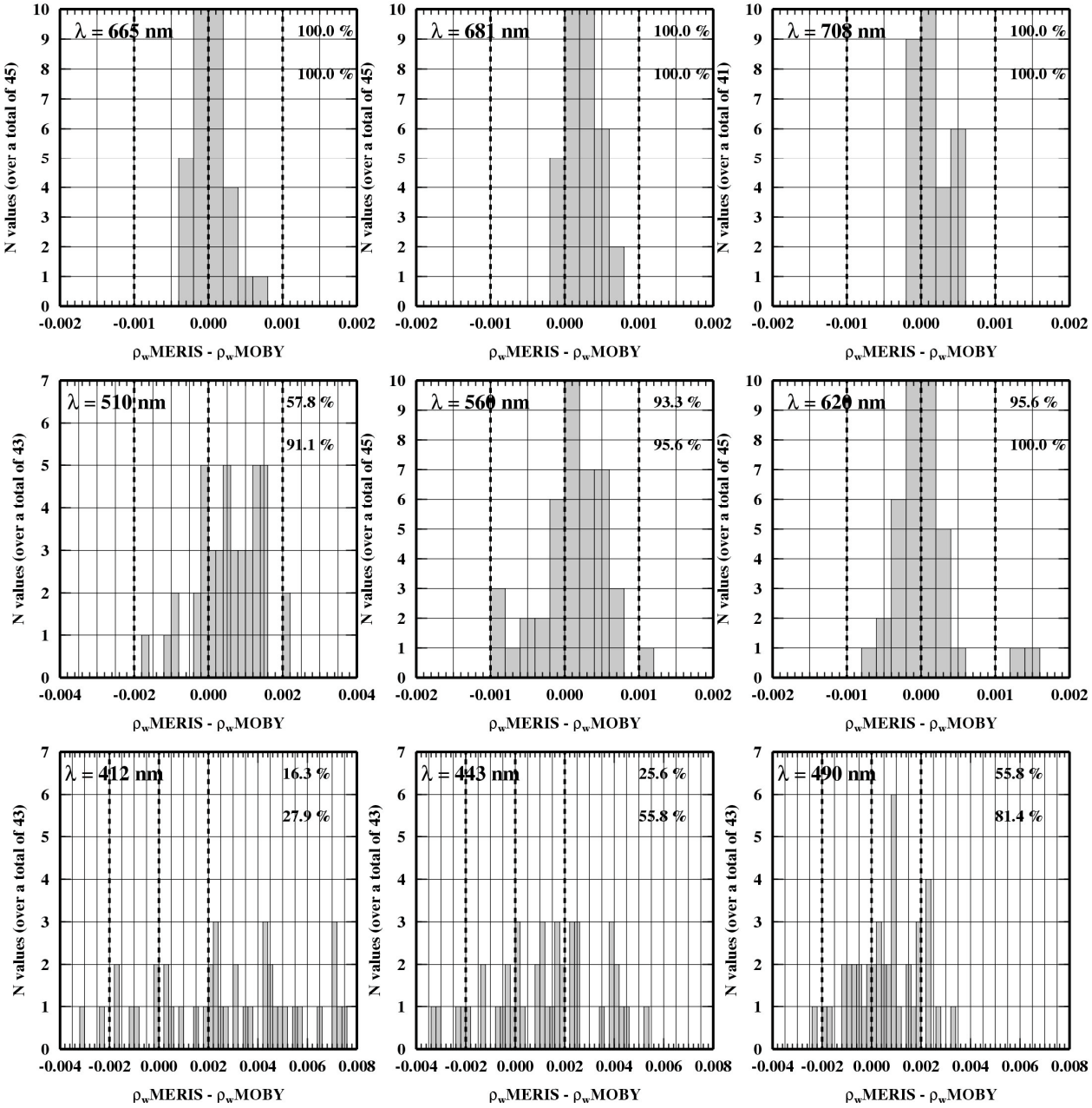

Fig. 13. : differences between the MERIS-derived and the MOBY-derived water-leaving reflectances for the wavelengths indicated. The vertical dashed lines grossly represent the specification of the atmospheric correction algorithm (*i.e.*, an accuracy of about ±0.002 in the blue and ±0.001 in the red).

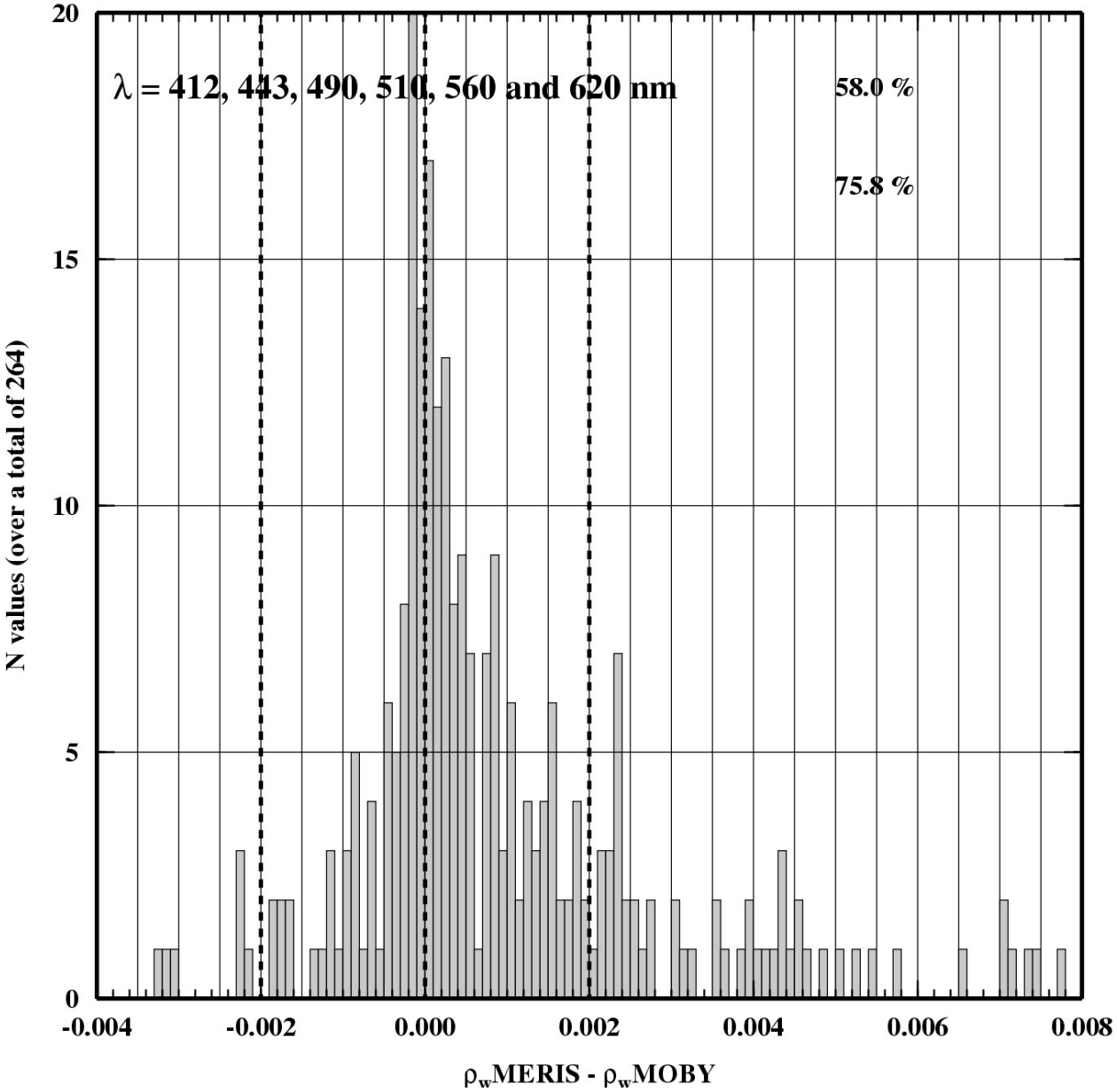

Fig. 14. As in Fig.13, but when the results for the 6 wavelengths indicated are pooled together.

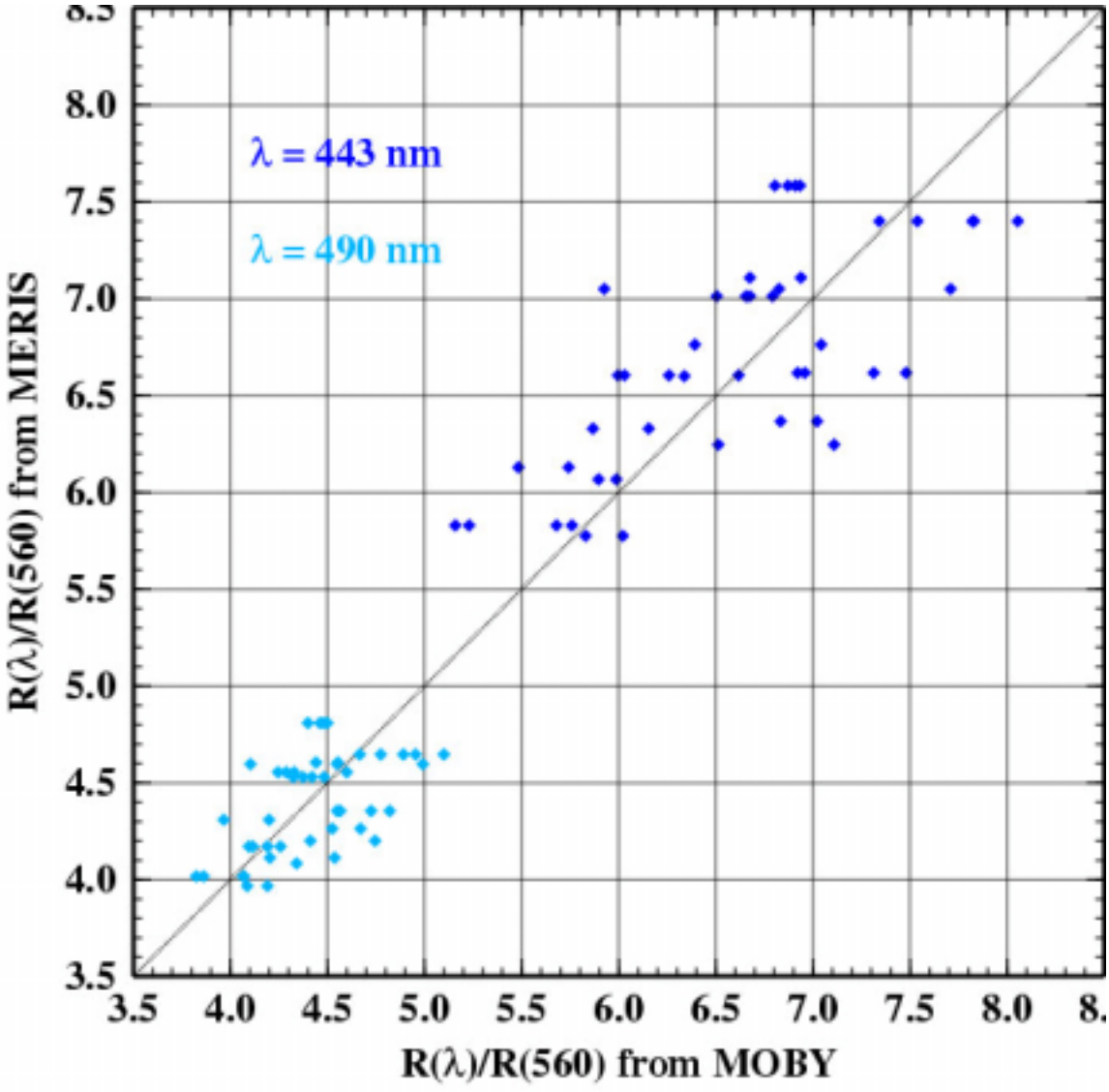

Fig. 15. Band ratio for the wavelengths indicated, either derived from the MERIS observations (vertical axis) or from the MOBY observations (horizontal axis).

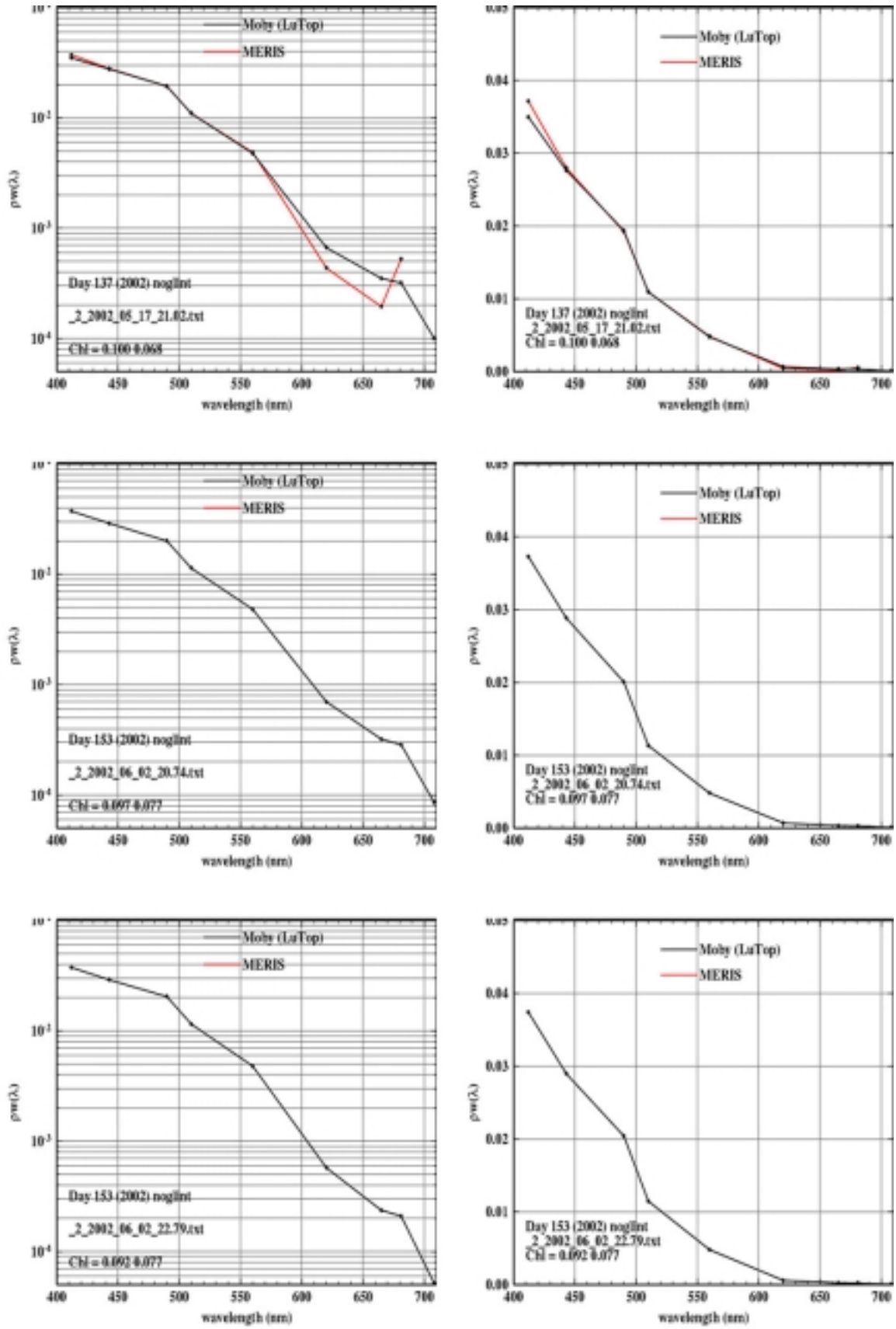

Figure 16. Spectra of the water-leaving reflectance (left panel : log scale ; right panel : linear scale), for the dates indicated. Results from the LOV breadboard and from the MERIS prototype are shown. The two chlorophyll values indicated are computed with the MERIS pigment index algorithm, either fed with the *in situ* reflectance values (left) or fed with the MERIS-derived reflectance values (right).

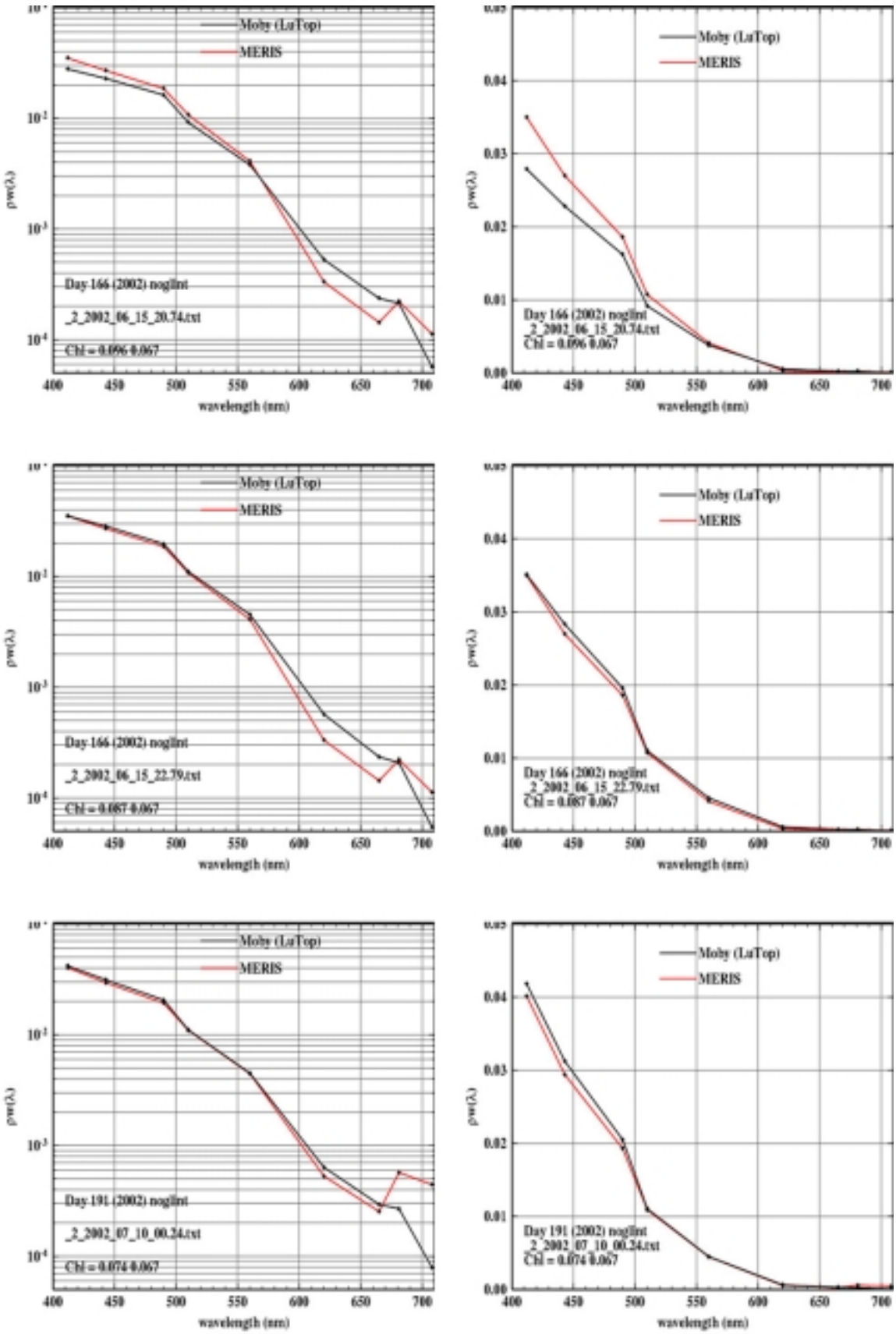

Figure 16. continued

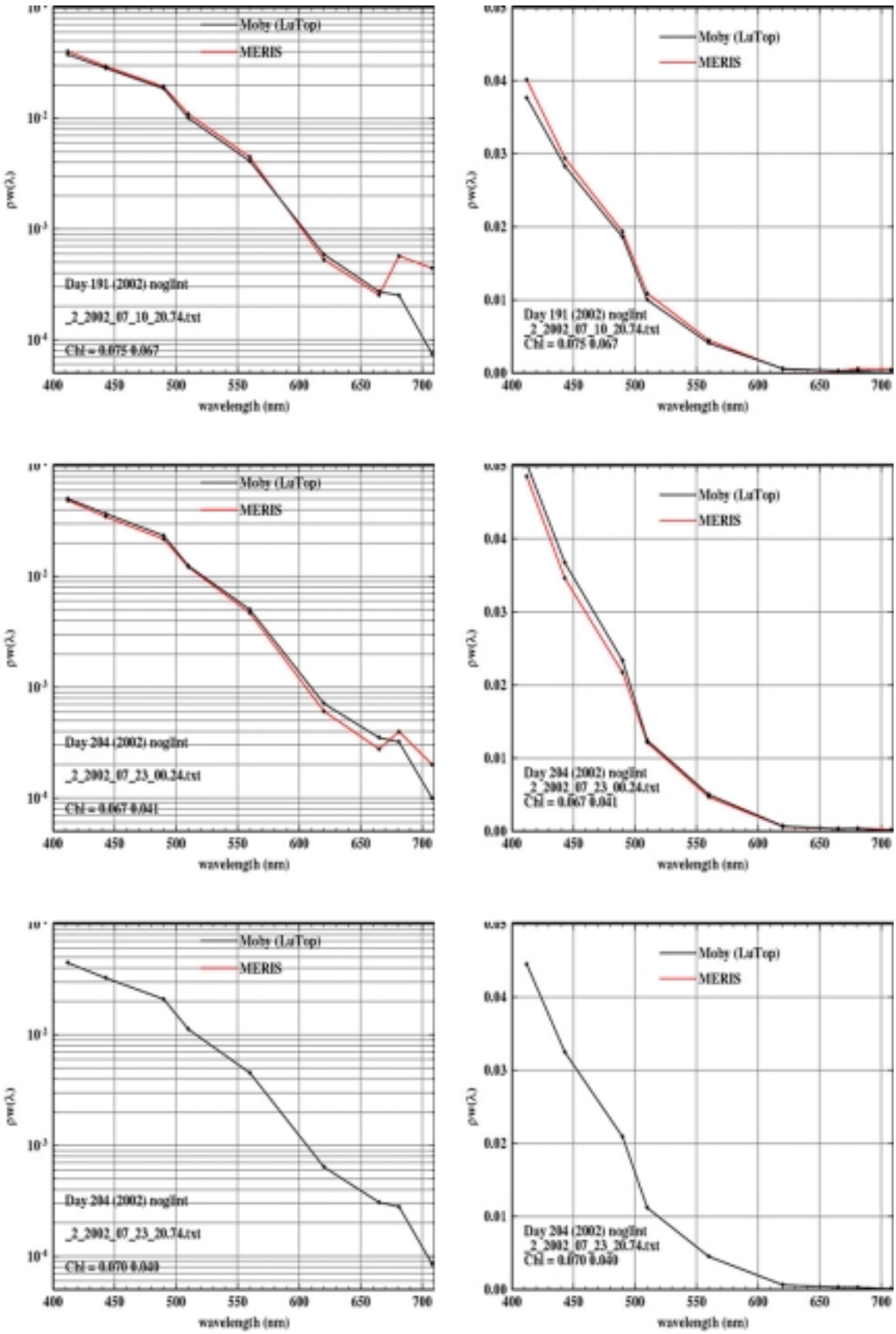

Figure 16. continued

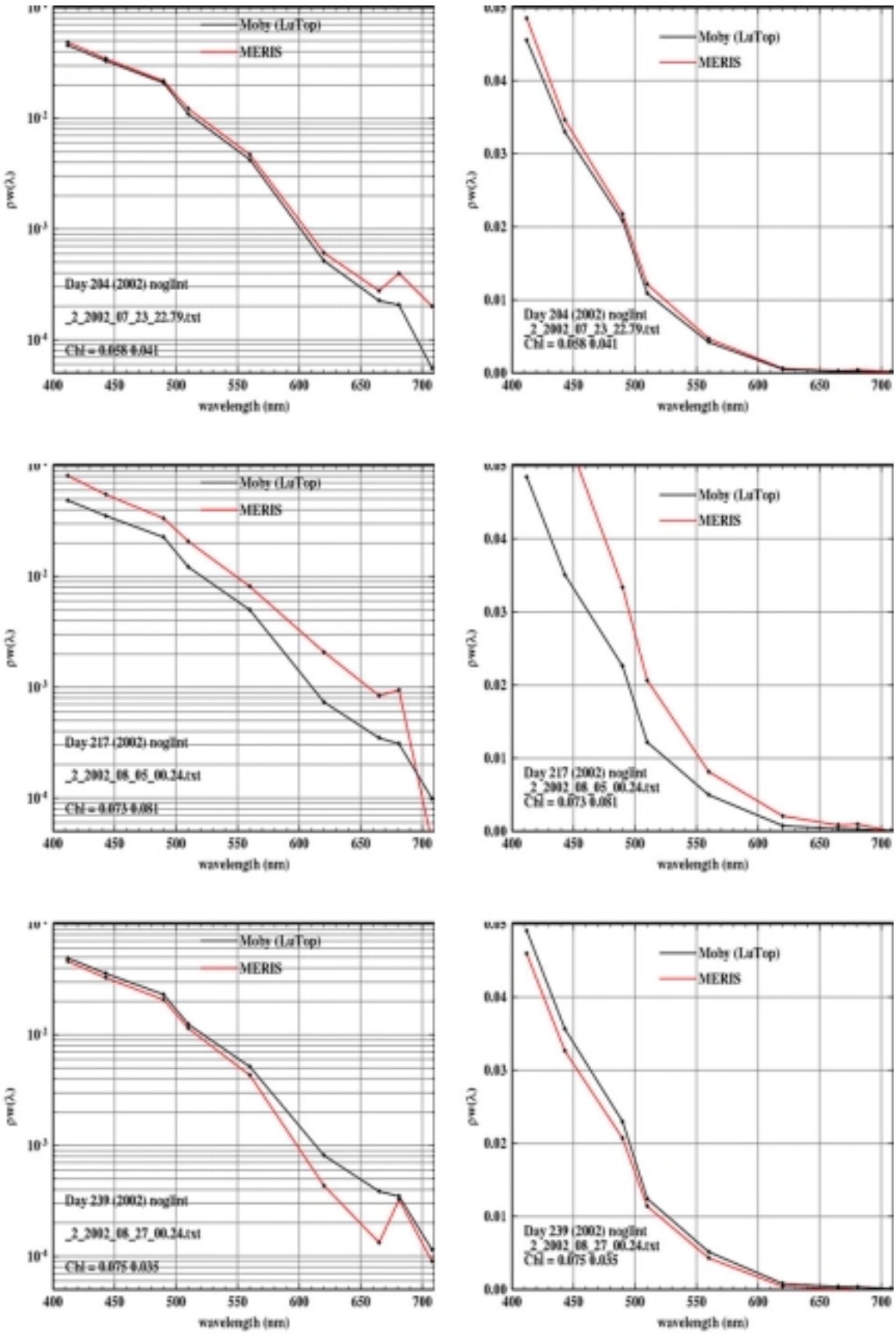

Figure 16. continued

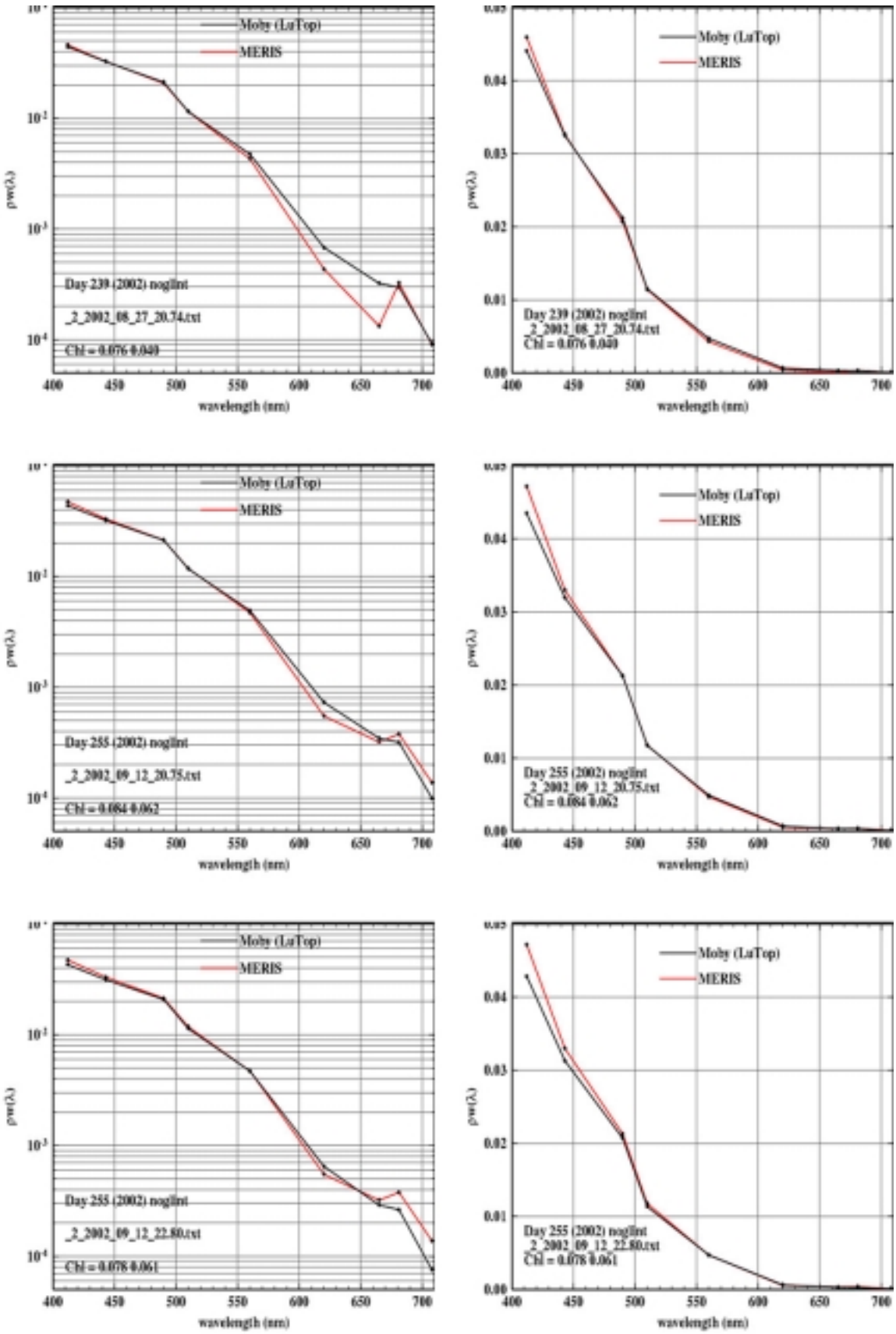

Figure 16. continued

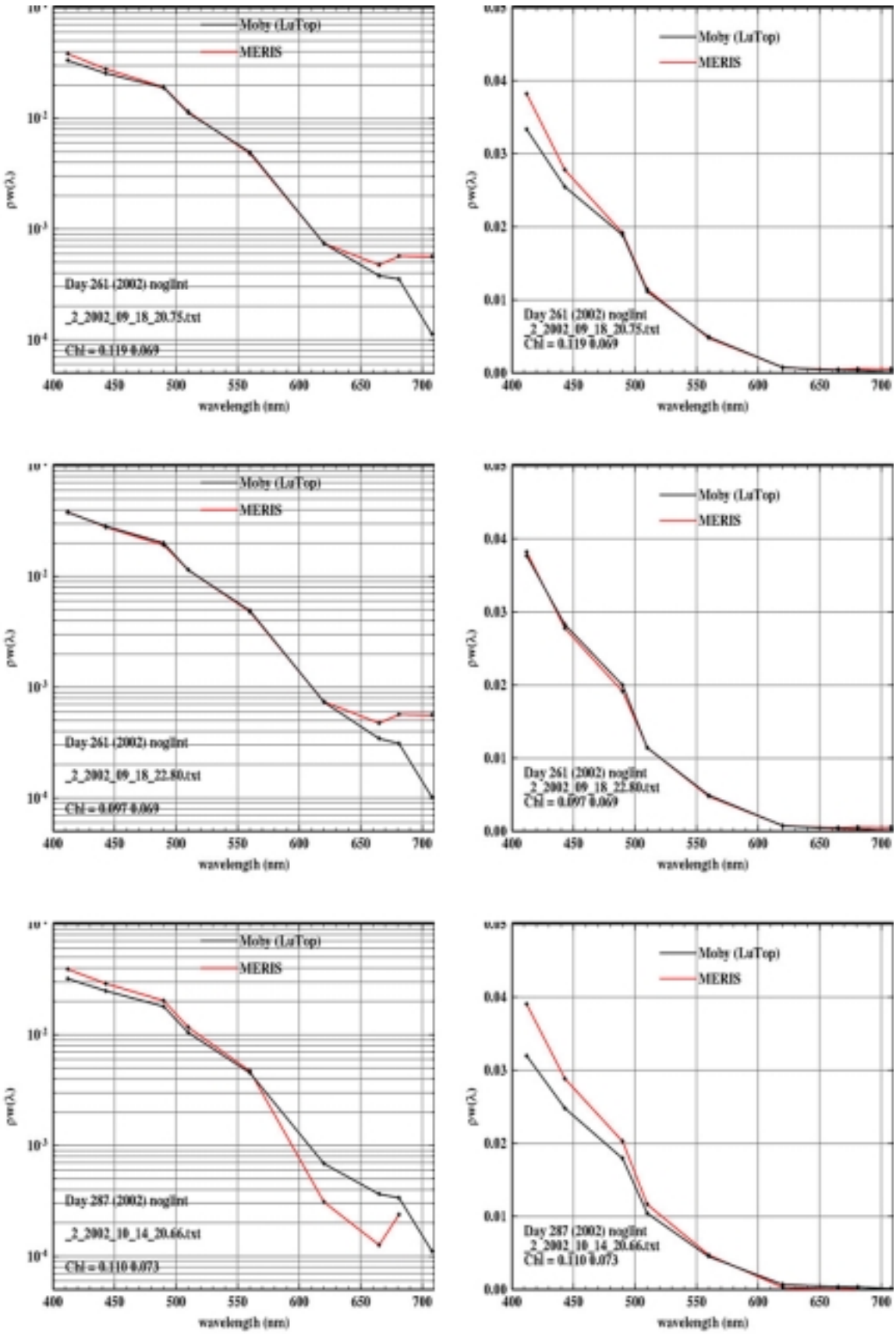

Figure 16. continued

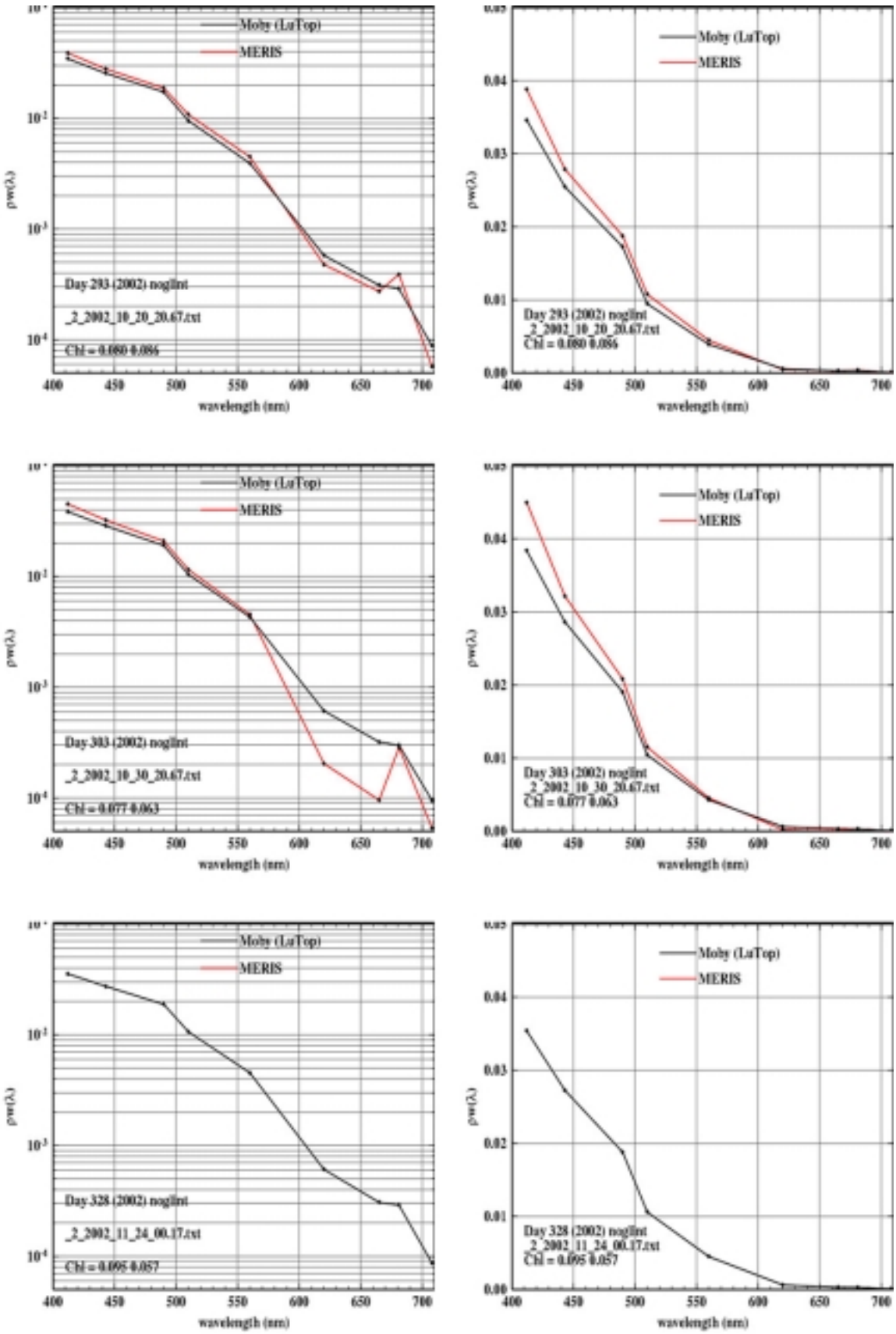

Figure 16. continued

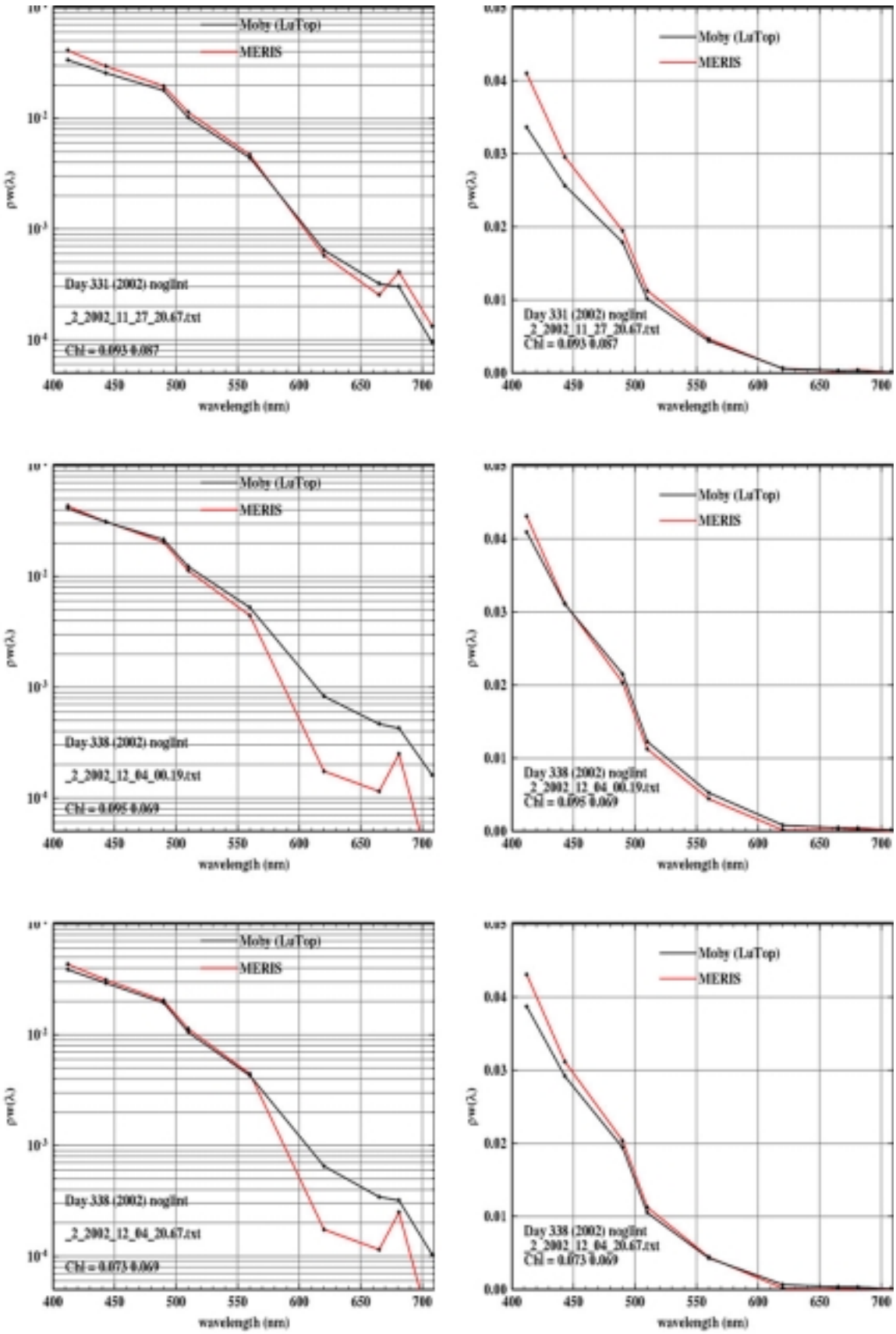

Figure 16. continued

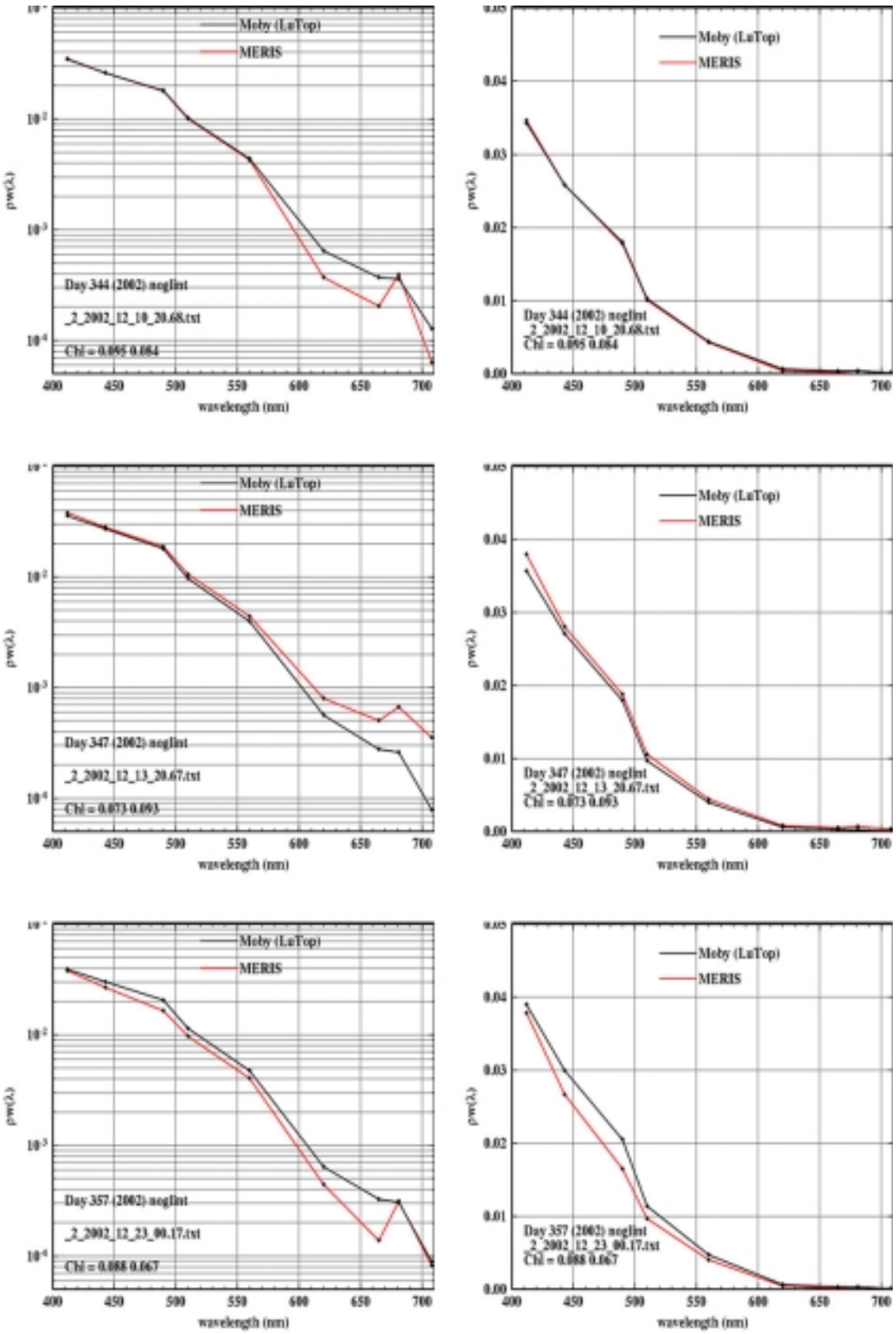

Figure 16. continued

9 References

Andreae M. O., 1996, Raising dust in the greenhouse, Nature **380**, 389-390.

Antoine, D. and A. Morel, 1998, Relative importance of multiple scattering by air molecules and aerosols in forming the atmospheric path radiance in the visible and near infrared parts of the spectrum, ***Appl. Opt.*** **37**, 2245-2259.

Antoine, D. and A. Morel, 1999, A multiple scattering algorithm for atmospheric correction of remotely-sensed ocean colour (MERIS instrument) : principle and implementation for atmospheres carrying various aerosols including absorbing ones, International Journal of Remote Sensing, 20, 1875-1916.

Clark, D. K., Gordon, H. R., Voss, K. J., Ge, Y., Broenkow, W., and Trees, C., 1997, Validation of atmospheric correction over the oceans, *Journal of Geophysical Research* **102**, 17209-17217.

Clark, D.K., M.A. Yarbrough, M. Feinholz, S. Flora, W. Broenkow, Y.S. Kim, B.C. Johnson, S.W. Brown, M. Yuen and J.L. Mueller, 2002, MOBY, a radiometric buoy for performance monitoring and vicarious calibration of satellite ocean color sensors : measurement and data analysis protocols, in "Ocean Optics Protocols for satellite ocean color validation", NASA/TM – 2002 – 210004/Rev 3-vol2, Feb. 2002, NASA GSFC, 138-170.

Gordon H. R., 1997, Atmospheric correction of ocean color imagery in the Earth observing system era, *J. Geophys. Res*. XX, xxx-xxx.

Gordon, H. R., and Clark, D. K., 1981, Clear water radiances for atmospheric correction of Coastal Zone Color Scanner imagery, *Applied Optics* **20**, 4175-4180.

Gordon H. R. and M. Wang, 1994, Retrieval of water-leaving reflectance and aerosol optical thickness over the oceans with SeaWIFS : a preliminary algorithm, *Appl. Opt*. **33**, 443-452.

Li X., H. Maring, D. Savoie, K. Voss, and J. M. Prospero, 1996, Dominance of mineral dust in aerosol light-scattering in the north Atlantic trade winds, *Nature* **380**, 416-419.

MEDIPROD group, 1976, Résultats de la campagne CINECA 5 - J. Charcot - Capricorne 7403 (1er Mars au 20 Avril 1974), Publications du CNEXO, N°10.

Morel A. and B. Gentili, 1991, Diffuse reflectance of oceanic waters : its dependence on sun angle as influenced by the molecular scattering contribution, *Appl. Opt*. **30**, 4427-4438.

Morel, A., and S. Maritorena, 2001, Bio-optical properties of oceanic waters: A reappraisal. Journal of Geophysical research, 106, 7763-7780.

OLIPAC (JGOFS) campaign, data unpublished.

O'Reilly, J.E., Maritorena, S., Mitchell, B.G., Siegel, D.A., Carder, K.L., Garver, S.A., Kahru, M. and McClain, C., 1998, Ocean color chlorophyll algorithms for SeaWiFS. *Journal of Geophysical Research* **103**, 24,937-24,953.

PACIPROD campaign, data unpublished.

Rast M. and J. L. Bézy, 1995, The ESA medium resolution imaging spectrometer (MERIS) : requirements to its mission and performance of its system, in RSS95, Remote Sensing in Action, Proc. 21st Annual Conf. Remote Sensing Soc., 11-14 September, 1995, University of Southampton, 125-132.

Shettle E. P. and R. W. Fenn, 1979, Models for the aerosols of the lower atmosphere and the effects of humidity variations on their optical properties, Environmental Research Papers, AFGL-TR-79-0214, Air Force Geophysics Laboratory, 20 September 1979.

Tyler J. E., 1973, Measurements of photosynthesis, available radiant flux, and supporting oceanographic data, Data report, SOCR Discoverer expedition, May 1970, S.I.O. Ref. 73-16, Univ. California.

World Climate Research Program, 1986, A preliminary cloudless standard atmosphere for radiation computation, Int. Ass. Meteorol. Atm. Phys., Radiation Commission, March 1986, WCP-112, WMO/TD-N° 24, 60 pp.

10 Glossary

ACRI-st :	"Mécanique Appliquée et Sciences de l'Environnement", French company in charge of the MERIS ground segment prototyping
ATBD :	Algorithm Theoretical Basis Document
BOUSSOLE :	"BOUée pour l'acquiSition de Séries Optiques à Long tErme" (an ocean colour calibration/validation project managed at LOV)
CCD :	Coupled Charge Device
CNES :	Centre National des Etudes Spatiales (French space agency)
DU :	Dobson Units
ECMWF :	European Centre for Medium Range Weather Forecast
ESA :	European Space Agency
LOV :	Laboratoire d'Océanographie de Villefranche
MEGS :	Meris Ground Segment
MERIS :	Medium Resolution Imaging Spectrometer (European ocean colour sensor, launched on the ENVISAT platform in March 2002)
MOBY :	Marine Optical Buoy
MODIS :	MODerate resolution Imaging Spectrometer (NASA's ocean colour sensor launched on the Terra satellite, December 1999, and on the Aqua satellite, May 2002).
MOS :	Marine Optical System
NASA :	US National Aeronautics and Space Administration
NIST :	US National Institute of Standards
NPL :	
PAR :	Photosynthetically Available Radiation
SeaWiFS :	Sea viewing WIde Field of view Sensor (NASA instrument aboard the Orbview Satellite, launched sept. 1997)
TOA :	Top Of Atmosphere
UPD :	Unbiased Percent Difference

11 Symbols

λ:	wavelength	nm
$L_w(\lambda,\theta_s,\theta',\Delta\phi)$:	Water-leaving normalised radiance	mW cm^{-2} sr^{-1} μ^{-1}
$[L_w]_N(\lambda,\theta_s,\theta',\Delta\phi)$:	Normalised water-leaving normalised radiance	mW cm^{-2} sr^{-1} μ^{-1}
$F_0(\lambda)$	Mean extraterrestrial spectral irradiance	W m^{-2} nm^{-1}
ε_c	Correction factor applied to $F_0(\lambda)$, and accounting for the changes in the Earth-sun distance. It is computed from the eccentricity of the Earth orbit, e = 0.0167, and from the day number D, as $\varepsilon_c = \left(1 + e\cos\left(\frac{2\pi(D-3)}{365}\right)\right)^2$	dimensionless
$E_d(0^+, \lambda)$:	Downward irradiance just above the sea surface	W m^{-2} μ^{-1}
$K_L(\lambda)$:	Diffuse attenuation coefficient for the upward radiance	m^{-1}
$L_u(\lambda)$:	Upward radiance	W m^{-2} sr^{-1} μ^{-1}
$Q(\lambda,\theta_s,\theta',\Delta\phi)$:	Q factor (*i.e.*, E_u/L_u)	sr

f : gfdfd

$R(\lambda, \theta_s)$:	Measured reflectance just below sea surface, *i.e.* $[(E_u(0^-) / (E_d(0^+))*0.96)]$, with a solar zenith angle θ_s	dimensionless
$\rho'_w(\lambda,\theta_s,\theta',\Delta\phi)$:	water-leaving reflectance ("MERIS definition" = $\pi L_w / E_d(0^+)$)	dimensionless
$a(\lambda)$:	Absorption coefficient	m^{-1}
$c(\lambda)$:	Attenuation coefficient	m^{-1}
$b_b(\lambda)$:	Back scattering coefficient	m^{-1}
θ_s:	solar zenith angle (cosine is μ_s)	degrees
θ_v:	Satellite viewing zenith angle (cosine is μ_v)	degrees
θ':	θ' = asin (sin(θ_v) / 1.34)	degrees
$\Delta\phi$:	Relative azimuth difference angle	degrees
$\tau_a(\lambda)$:	Aerosol optical thickness	dimensionless
$\tau_r(\lambda)$:	Rayleigh optical thickness	dimensionless
$\tau_{oz}(\lambda)$:	Ozone optical thickness	dimensionless
$t_{\theta_s}(\lambda,\theta_s)$	Irradiance transmittance for a sun zenith angle θ_s	dimensionless
	$t_{\theta_s}(\lambda,\theta_s) = E_d(0^+) / (\mu_s \varepsilon_c F_0)$, where $E_d(0^+)$ is the downwelling irradiance just above the sea surface	
$t_d(\lambda, \theta)$	Diffuse transmittance for angle θ	dimensionless
	$t_d(\lambda, \theta) = L_{TOA}(\lambda,\theta_s,\theta_v,\Delta\phi) / L_{0+}(\lambda,\theta_s,\theta_v,\Delta\phi)$	
RH	Relative humidity	percents
$\rho(\lambda,\theta_s,\theta_v,\Delta\phi)$	Reflectance ($\pi L / F_0 \mu_s$)	dimensionless

where the product π.L is the TOA upwelling irradiance if upwelling radiances are equal to $L(\lambda,\theta_s,\theta_v,\Delta\phi)$, for any values of θ_v within 0-π/2 and any $\Delta\phi$ within 0-2π.

Subscripts t : total reflectance
w : water-leaving reflectance
path : path reflectance
r : Rayleigh reflectance
a: aerosol reflectance
ra: heterogeneous aerosol-molecule scattering
G : sun glint reflectance

$\rho^*(\lambda,\theta_s,\theta_v,\Delta\phi)$	Reflectance within a compound atmosphere, containing molecules and aerosols (subscripts as for ρ)	dimensionless
$\Re(\theta')$	Geometrical factor, accounting for all refraction and reflection effects at the air-sea interface (Morel and Gentili, 1996)	dimensionless

$$\Re(\theta') = \left[\frac{(1-\bar{\rho})}{(1-\bar{r}R)} \frac{(1-\rho_F(\theta'))}{n^2} \right]$$ (subscript 0 when θ' = 0)

where

n is the refractive index of water	dimensionless
$\rho_F(\theta)$ is the Fresnel reflection coefficient for incident angle θ	dimensionless
$\bar{\rho}$ is the mean reflection coefficient for the downwelling irradiance at the sea surface	dimensionless
$\bar{r}$ is the average reflection for upwelling irradiance at the water-air interface	dimensionless

12 Appendix 1 : the MERIS chlorophyll concentration images

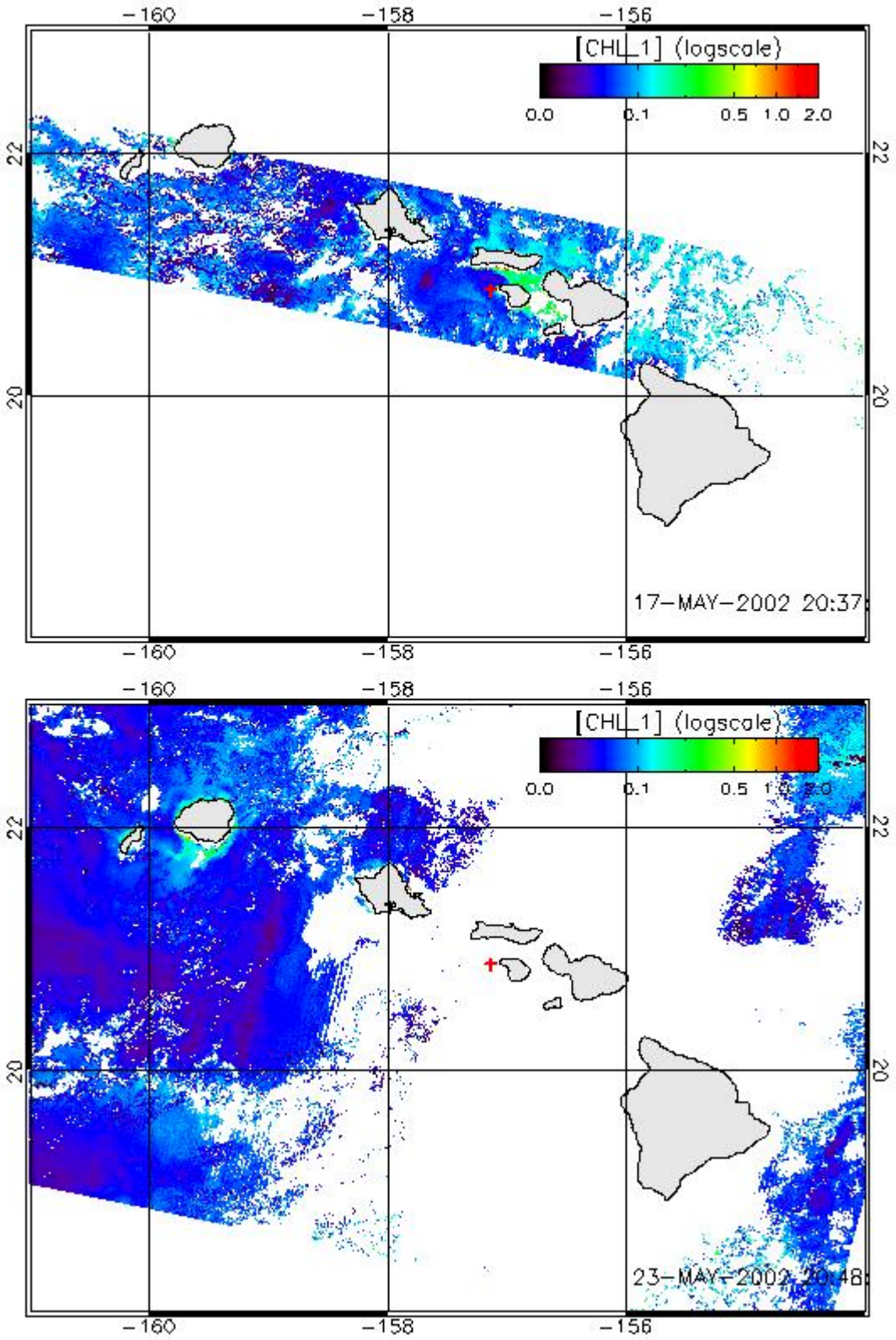

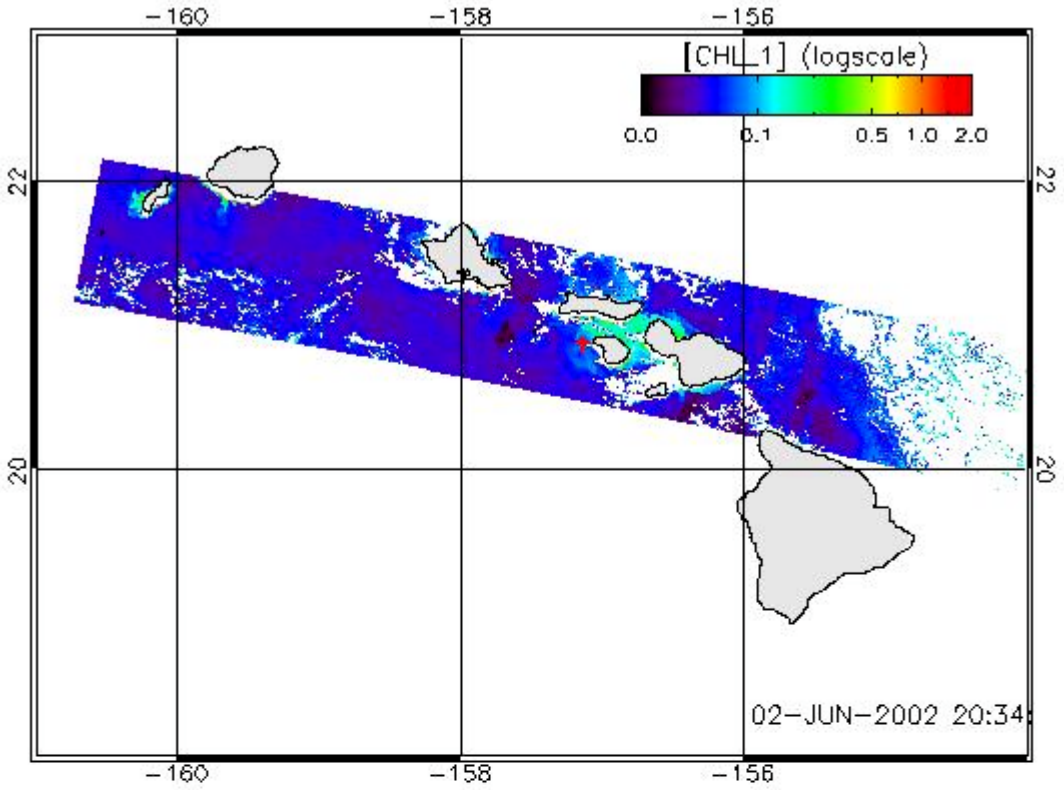
−160
−158
−156
[CHL_1] (logscale)
0.0
0.1
0.5
1.0
2.0
22
20
02−JUN−2002 20:34

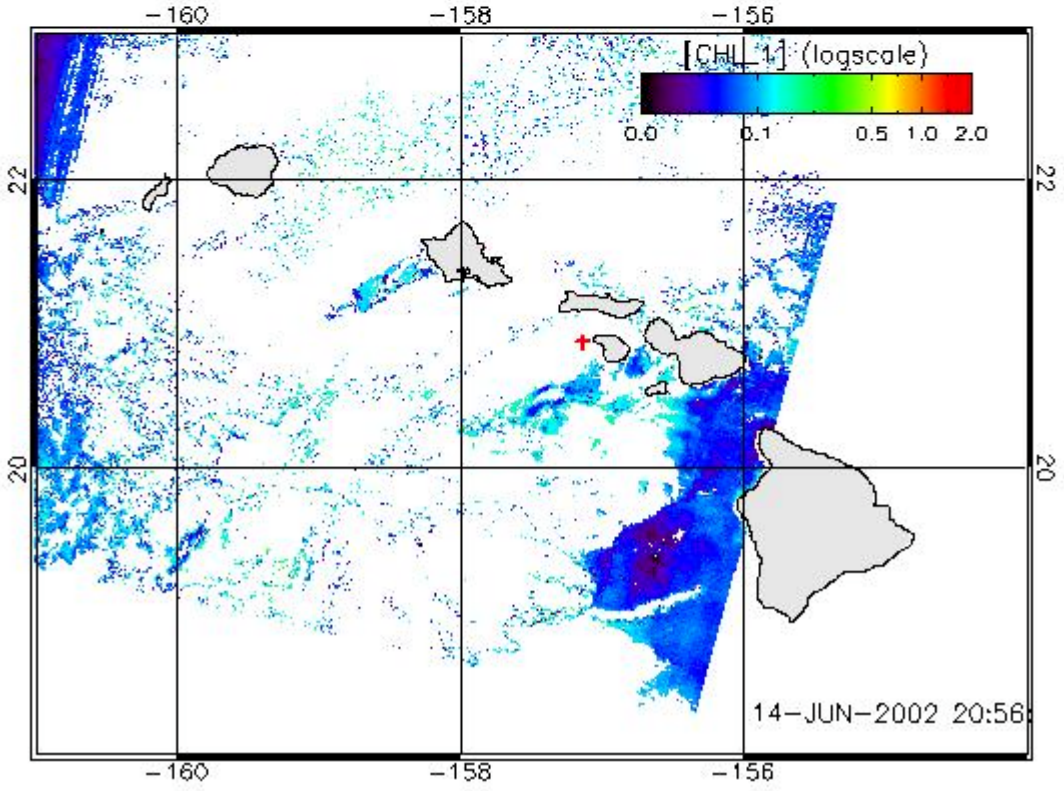
−160
−158
−156
[CHL_1] (logscale)
0.0
0.1
0.5
1.0
2.0
22
20
14−JUN−2002 20:56

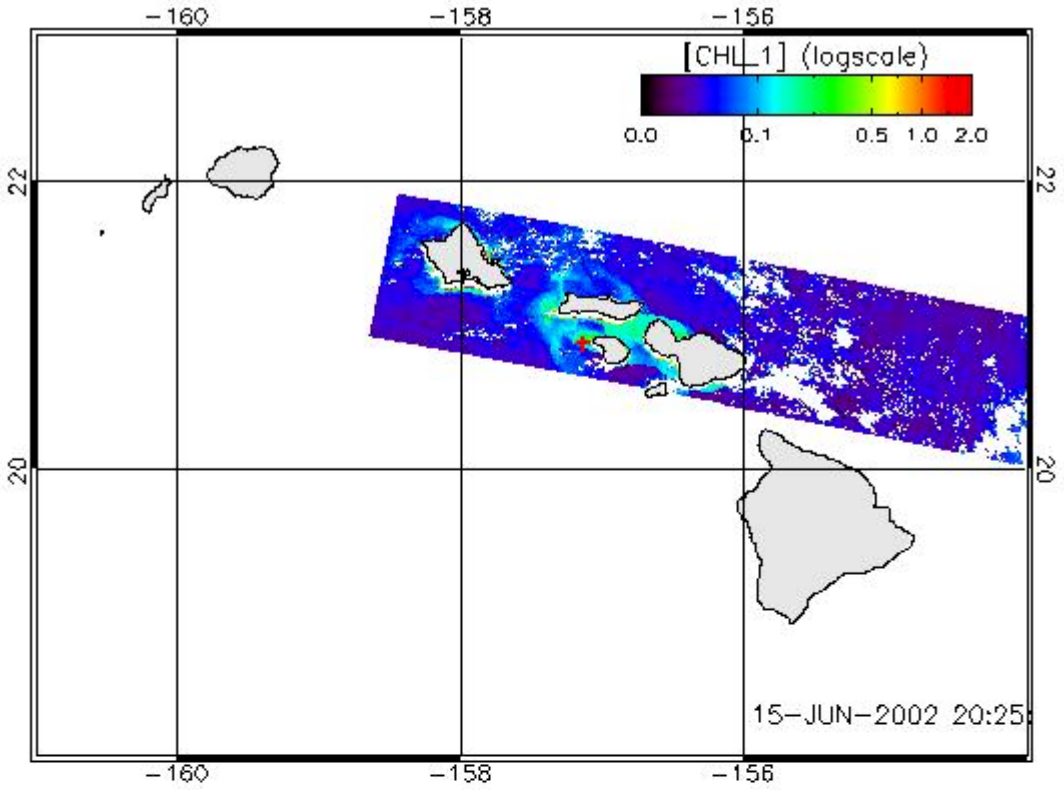
−160
−158
−156
[CHL_1] (logscale)
0.0
0.1
0.5
1.0
2.0
22
20
15−JUN−2002 20:25

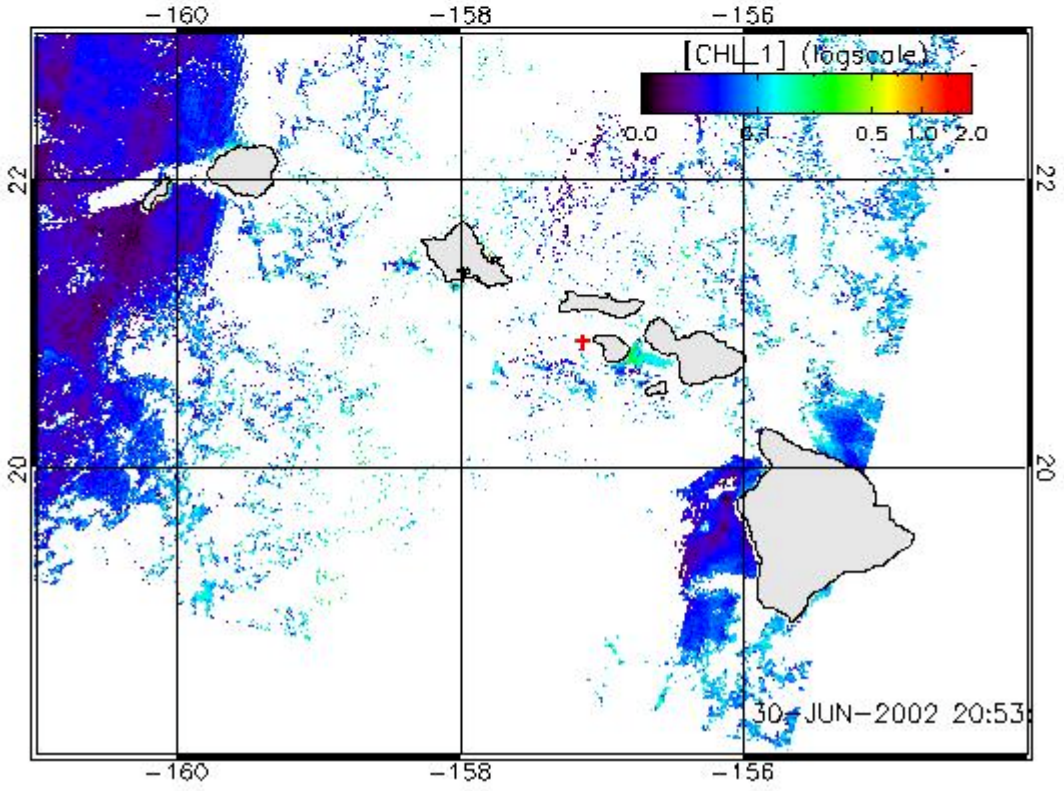
−160
−158
−156
[CHL_1] (logscale)
0.0
0.1
0.5
1.0
2.0
22
20
30−JUN−2002 20:53

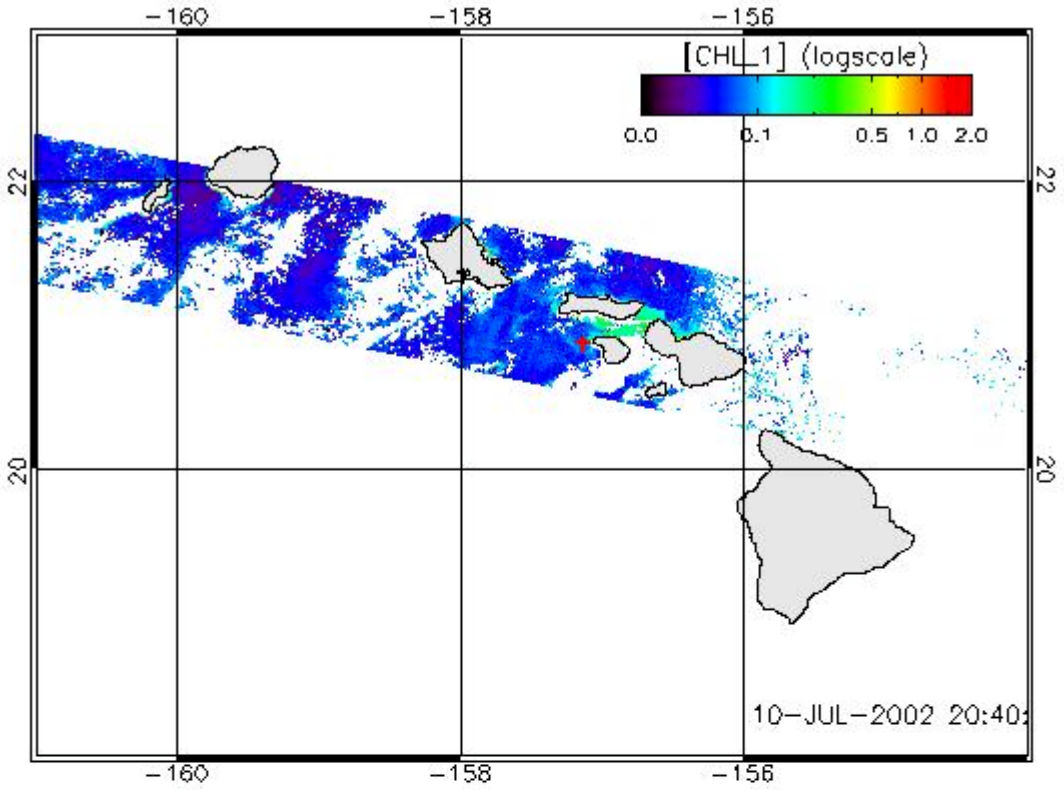
−160
−158
−156
[CHL_1] (logscale)
0.0
0.1
0.5
1.0
2.0
22
20
10−JUL−2002 20:40

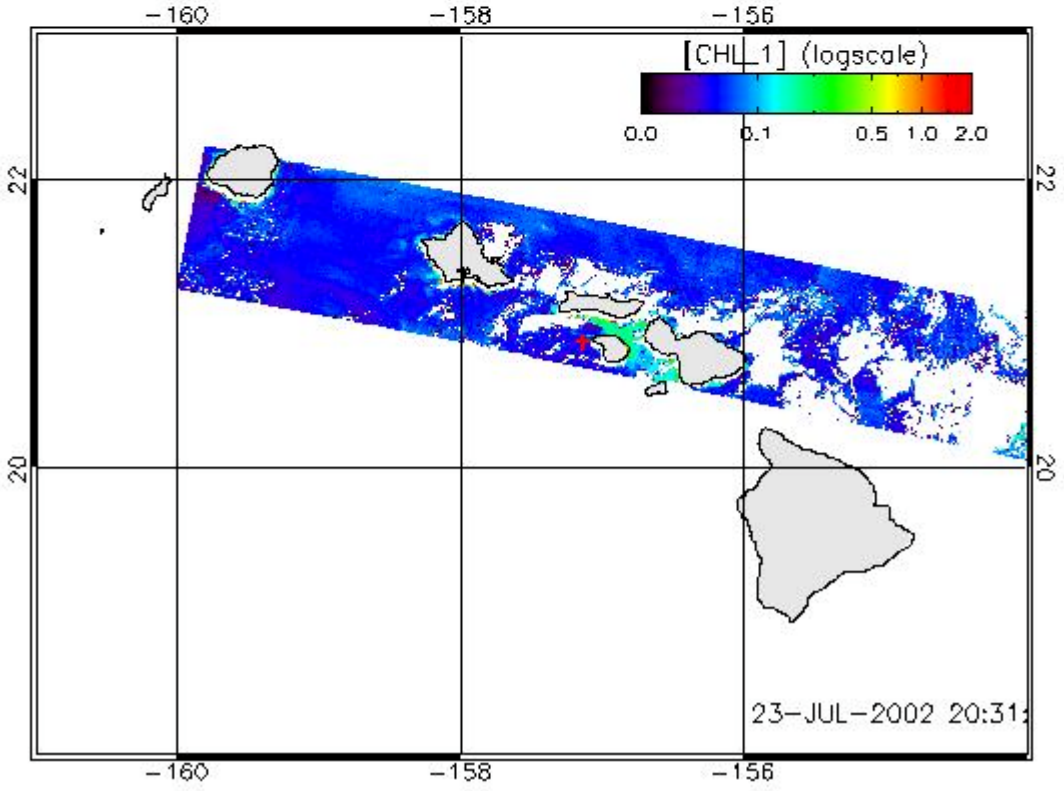
−160
−158
−156
[CHL_1] (logscale)
0.0
0.1
0.5
1.0
2.0
22
20
23−JUL−2002 20:31

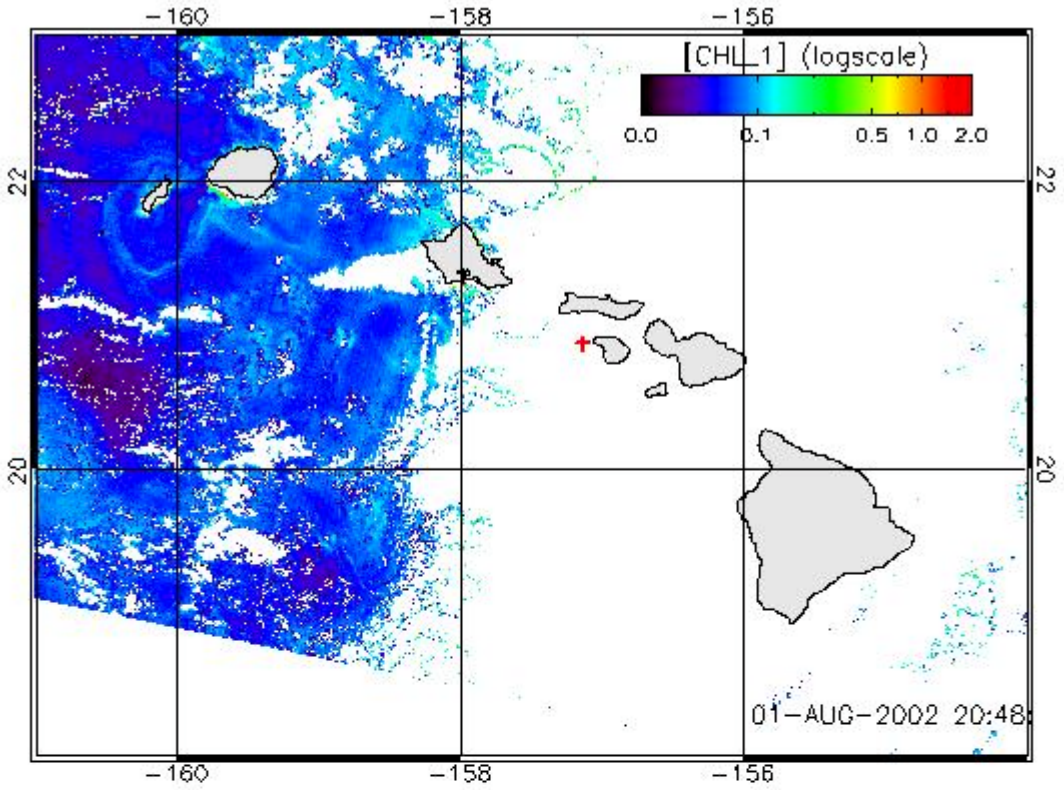
−160
−158
−156
[CHL_1] (logscale)
0.0
0.1
0.5
1.0
2.0
22
20
01−AUG−2002 20:48

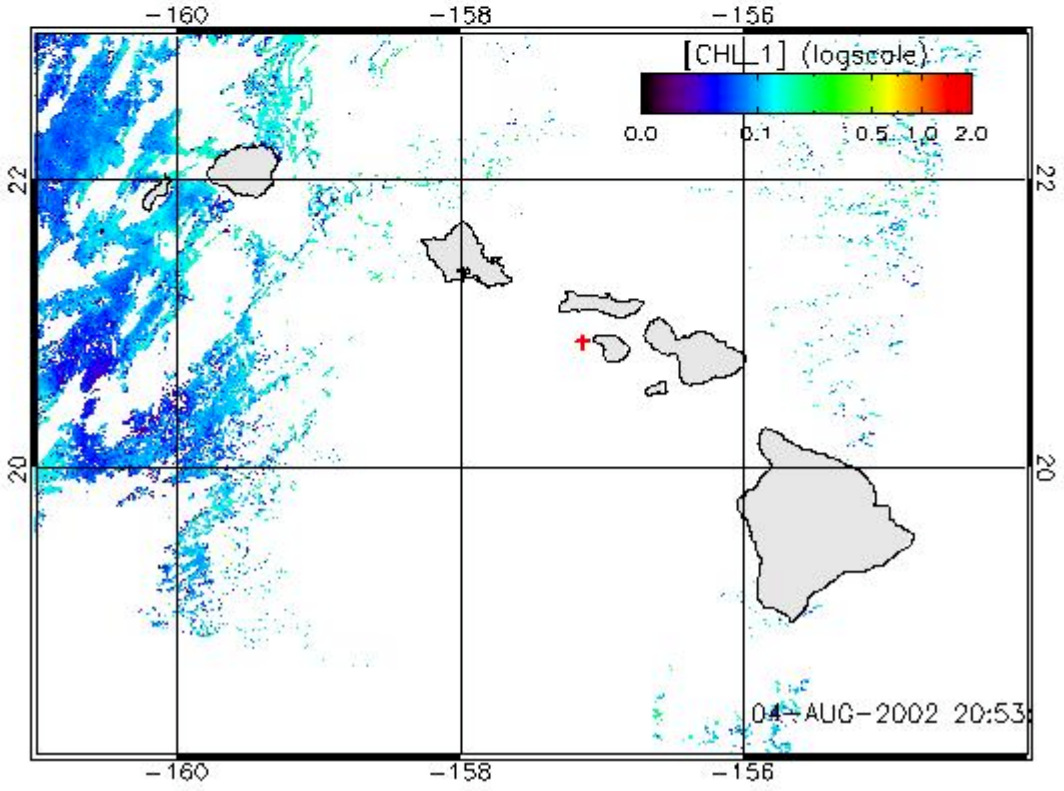
−160
−158
−156
[CHL_1] (logscale)
0.0
0.1
0.5
1.0
2.0
22
20
04−AUG−2002 20:53

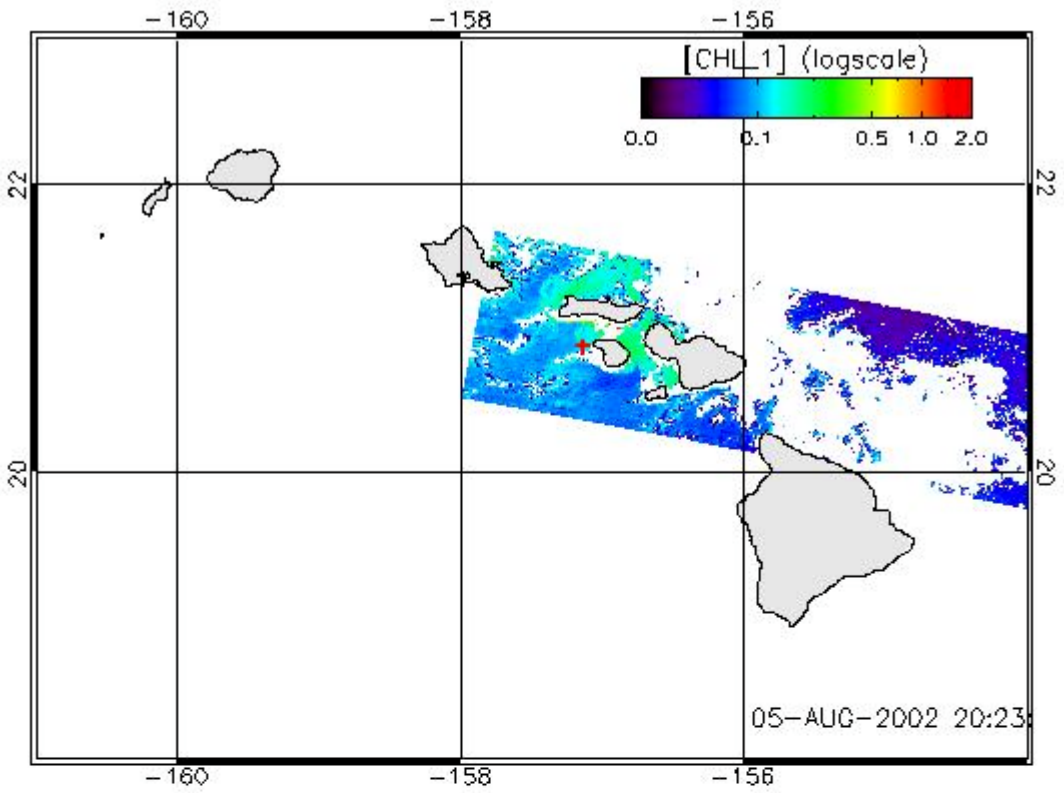
−160
−158
−156
[CHL_1] (logscale)
0.0
0.1
0.5
1.0
2.0
22
20
05−AUG−2002 20:23:

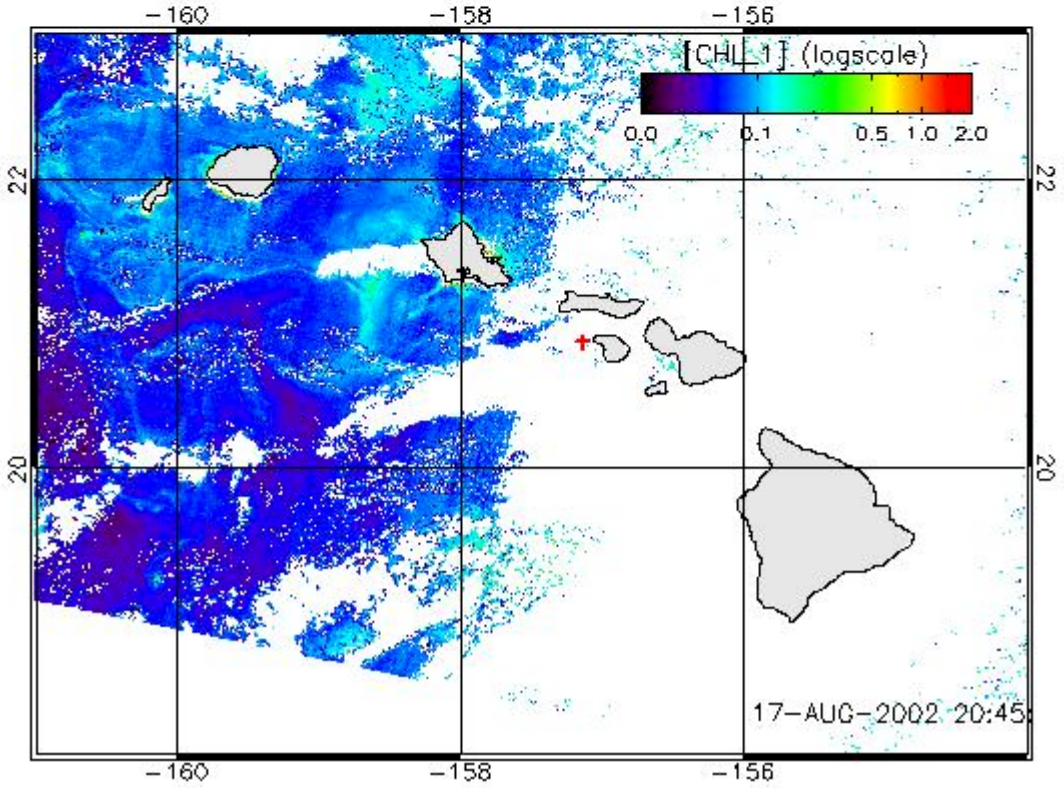
−160
−158
−156
[CHL_1] (logscale)
0.0
0.1
0.5
1.0
2.0
22
20
17−AUG−2002 20:45:

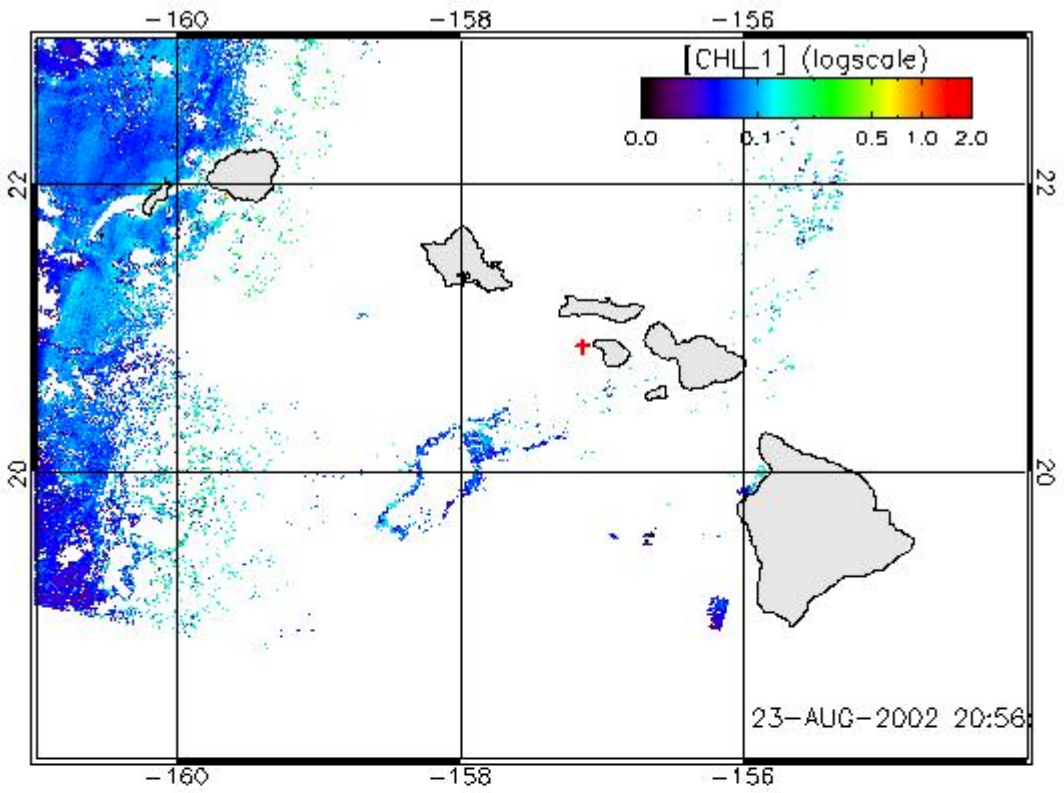
−160
−158
−156
[CHL_1] (logscale)
0.0
0.1
0.5
1.0
2.0
22
20
23−AUG−2002 20:56:

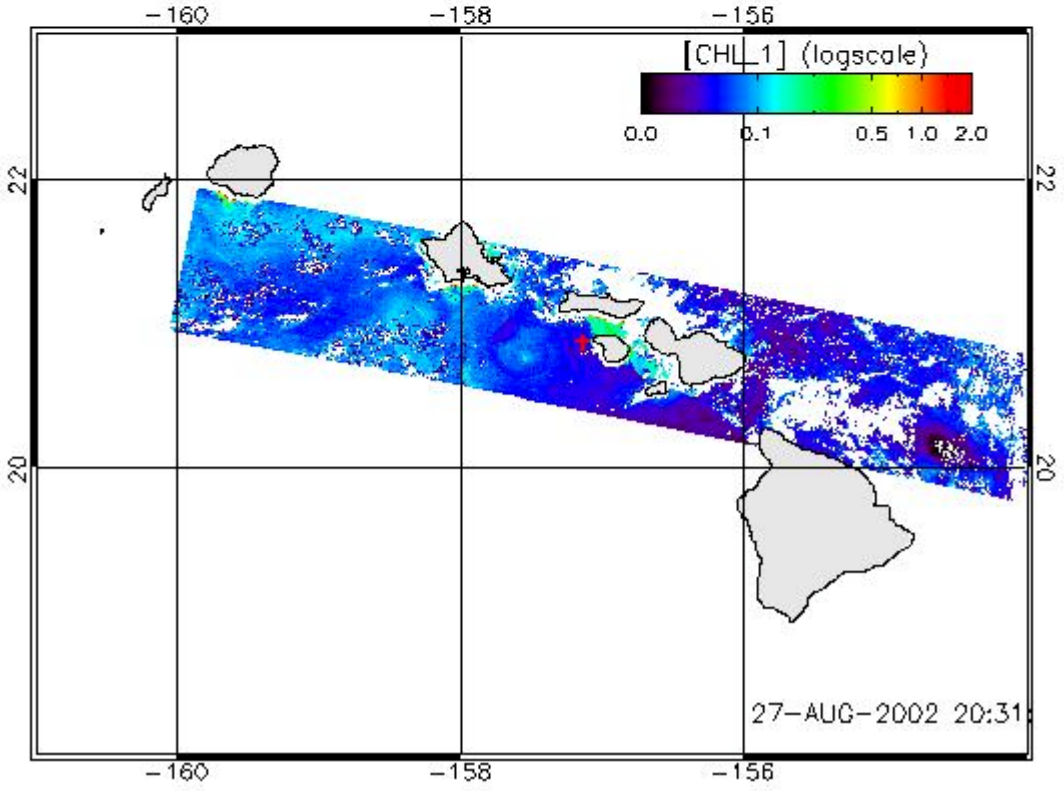
−160
−158
−156
[CHL_1] (logscale)
0.0
0.1
0.5
1.0
2.0
22
20
27−AUG−2002 20:31:

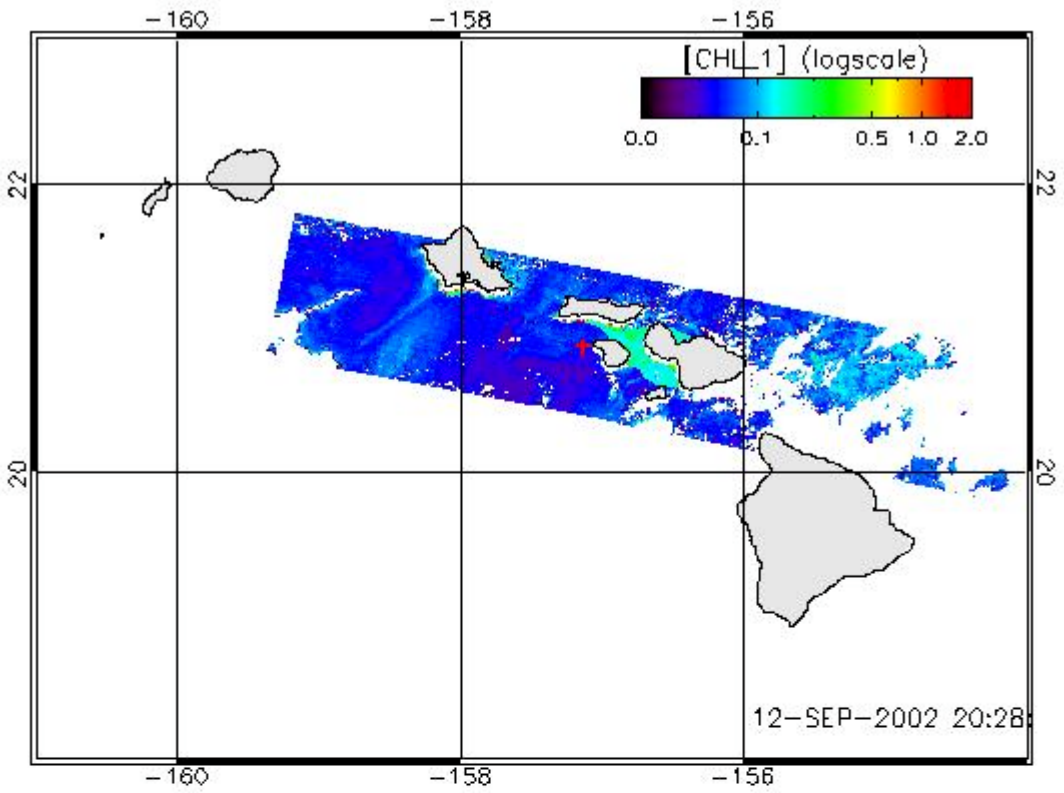
−160
−158
−156
[CHL_1] (logscale)
0.0
0.1
0.5
1.0
2.0
22
20
12−SEP−2002 20:28

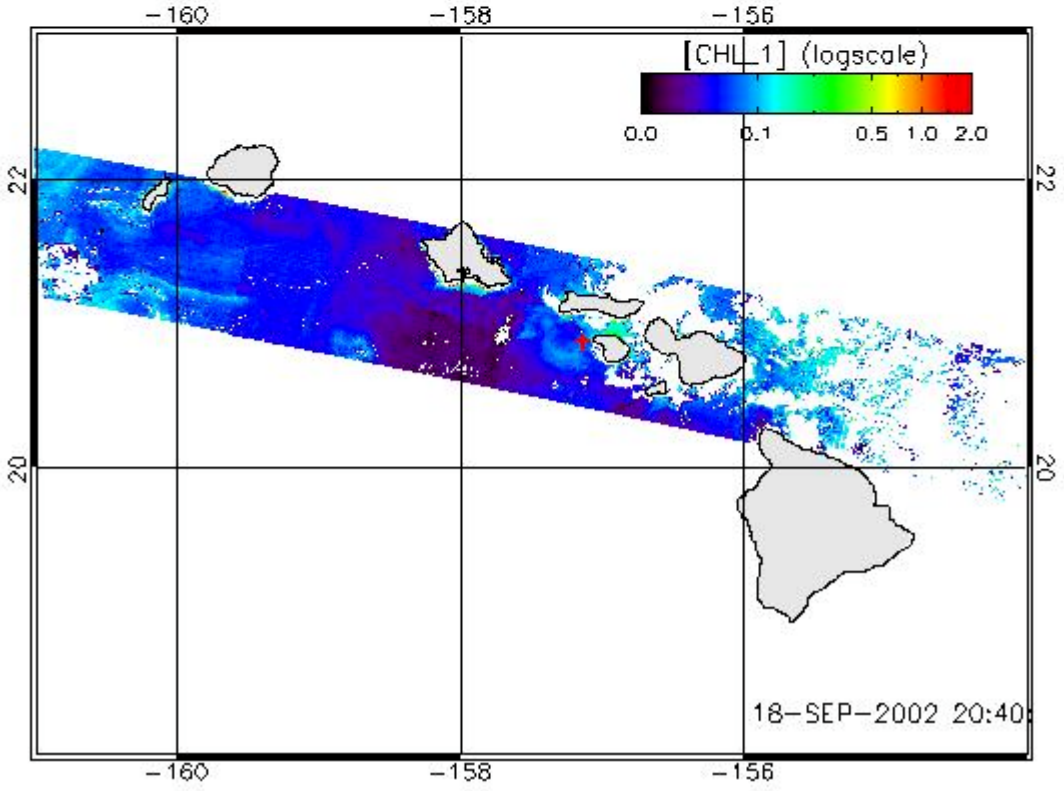
−160
−158
−156
[CHL_1] (logscale)
0.0
0.1
0.5
1.0
2.0
22
20
18−SEP−2002 20:40

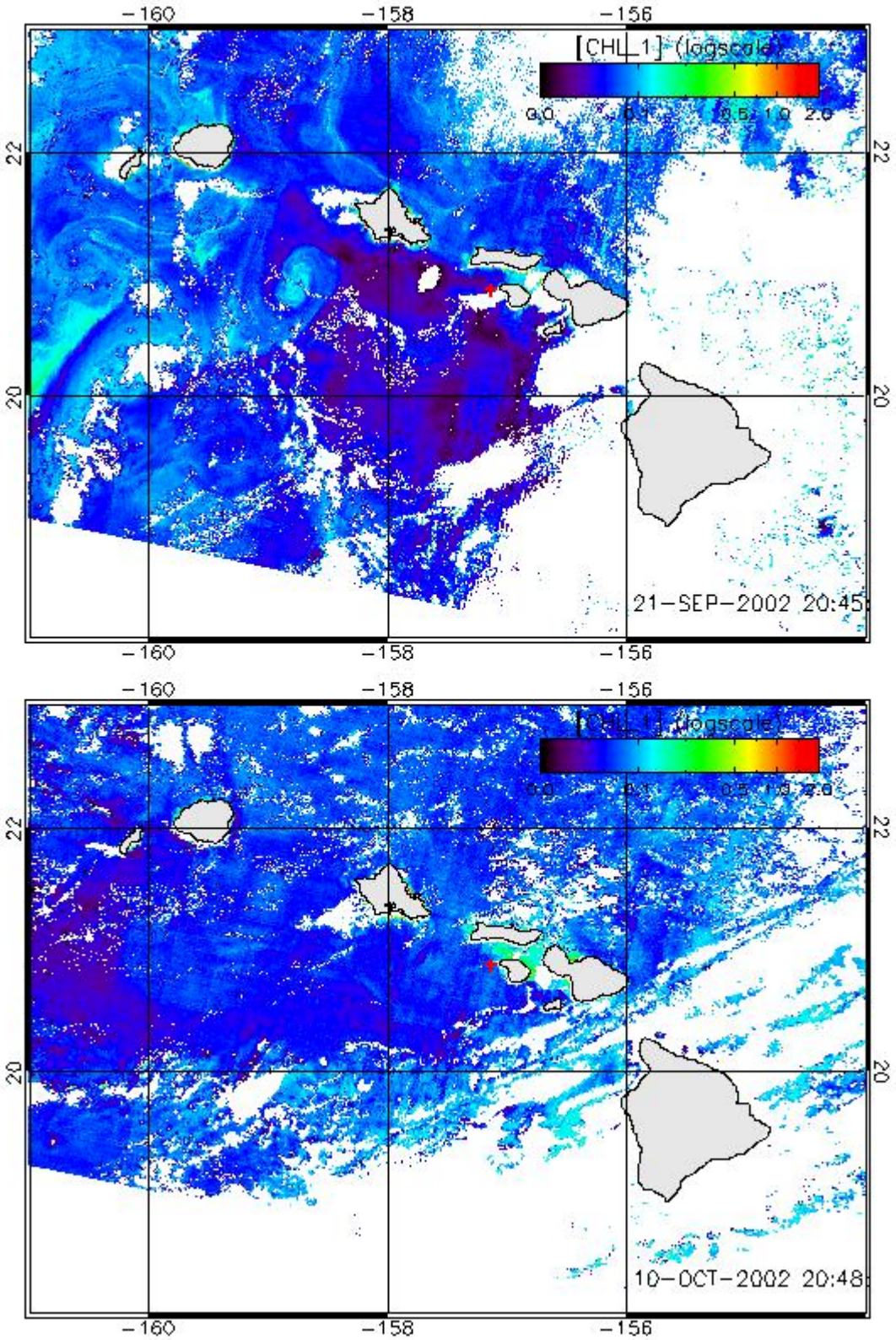
−160
−158
−156
22
20
[CHL_1] (logscale)
0.0
0.5
1.0
2.0
21−SEP−2002 20:45
10−OCT−2002 20:48

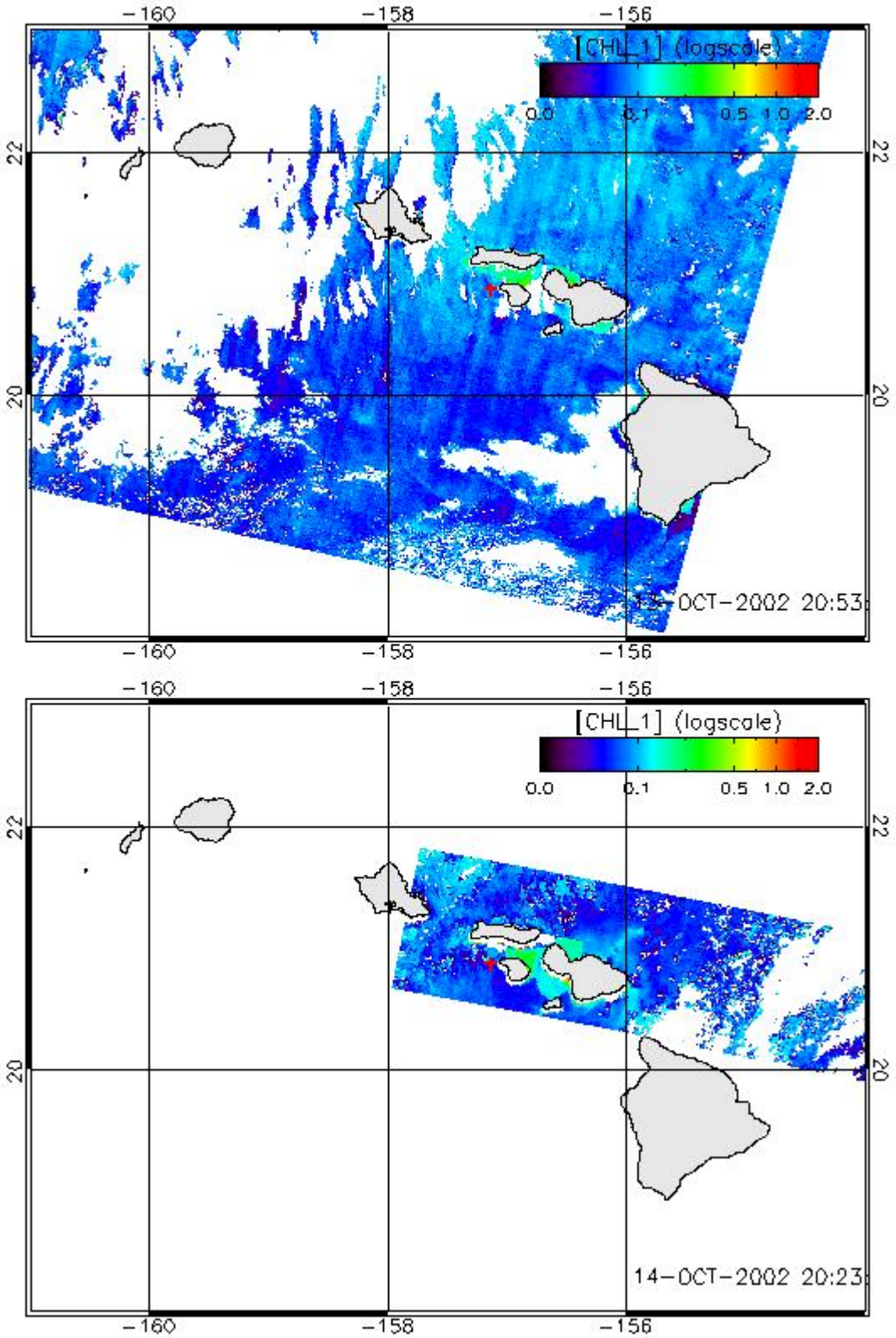
[CHL_1] (logscale)
0.0 0.1 0.5 1.0 2.0
-160
-158
-156
22
20
13-OCT-2002 20:53
[CHL_1] (logscale)
0.0 0.1 0.5 1.0 2.0
14-OCT-2002 20:23

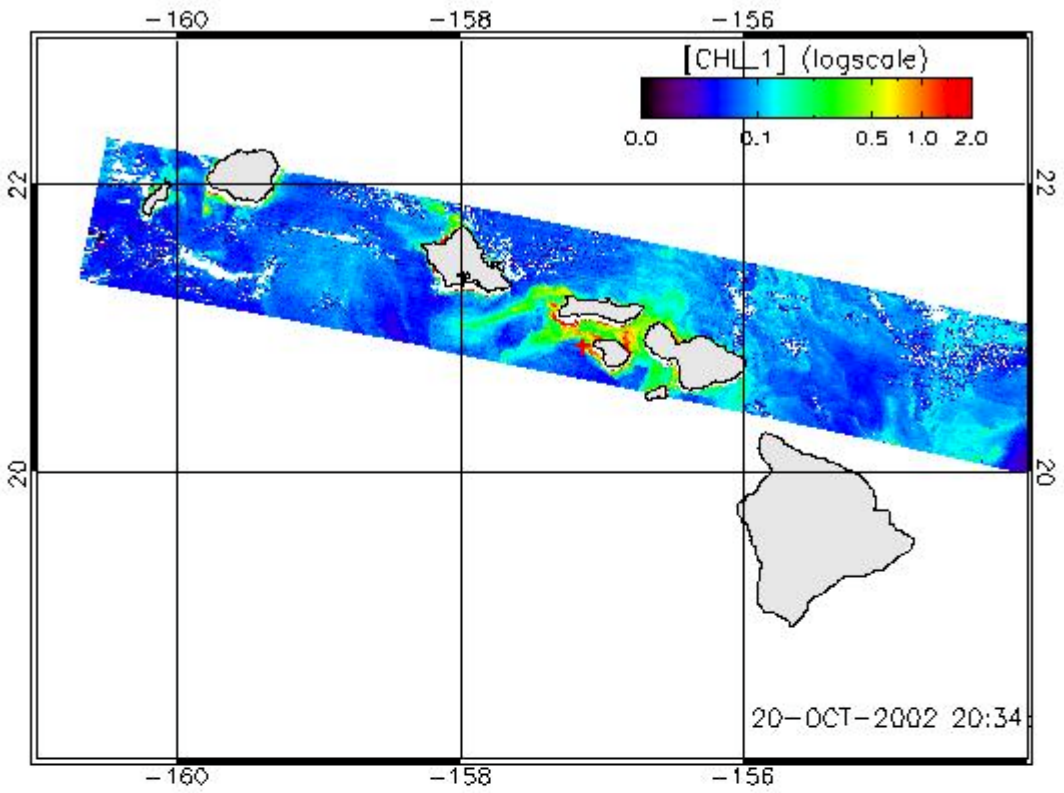
−160
−158
−156
[CHL_1] (logscale)
0.0
0.1
0.5
1.0
2.0
22
20
20−OCT−2002 20:34

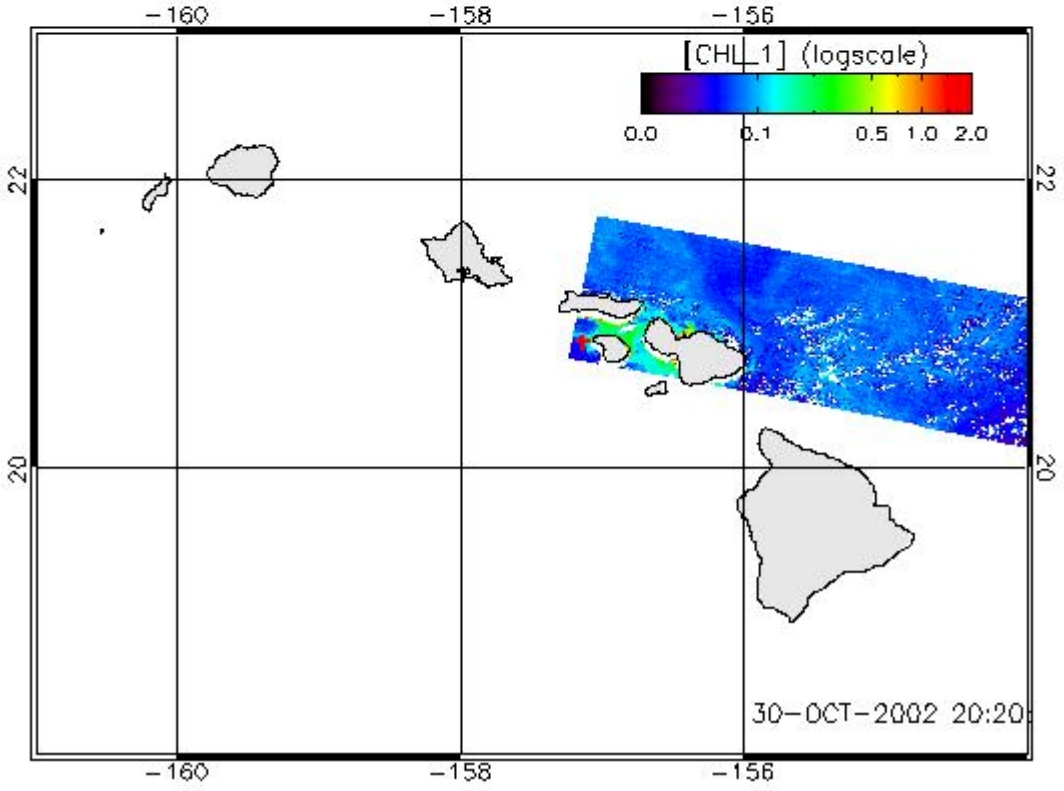
−160
−158
−156
[CHL_1] (logscale)
0.0
0.1
0.5
1.0
2.0
22
20
30−OCT−2002 20:20

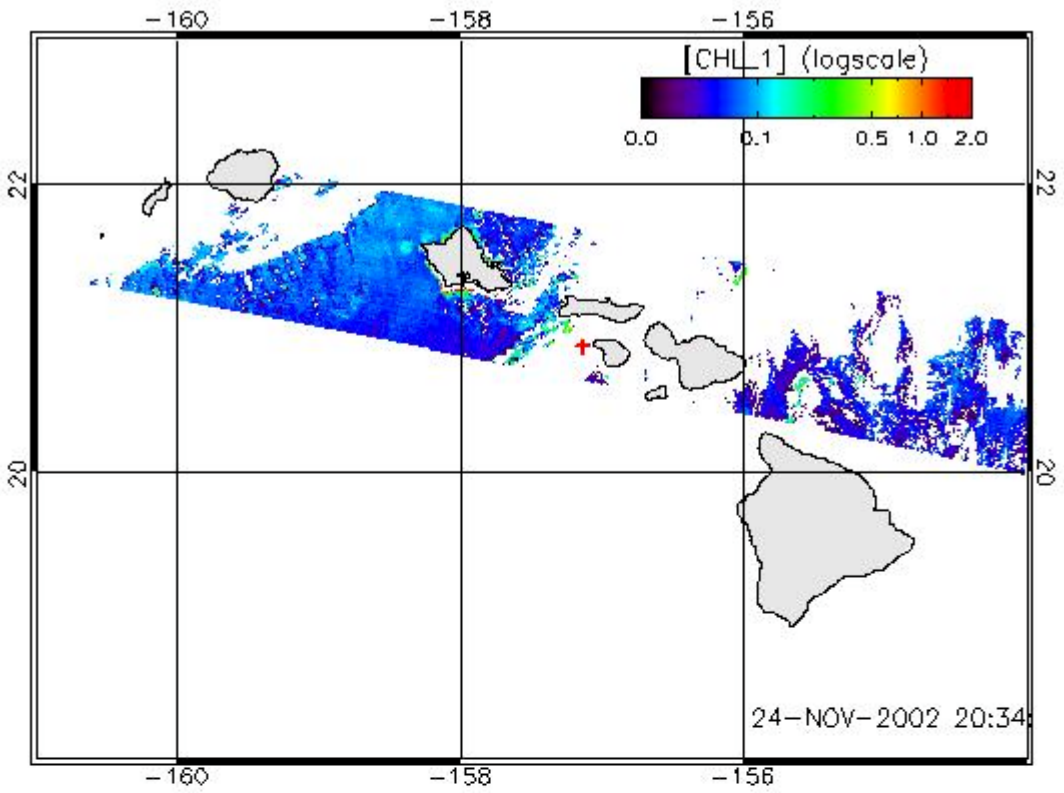
−160
−158
−156
[CHL_1] (logscale)
0.0
0.1
0.5
1.0
2.0
22
20
24−NOV−2002 20:34

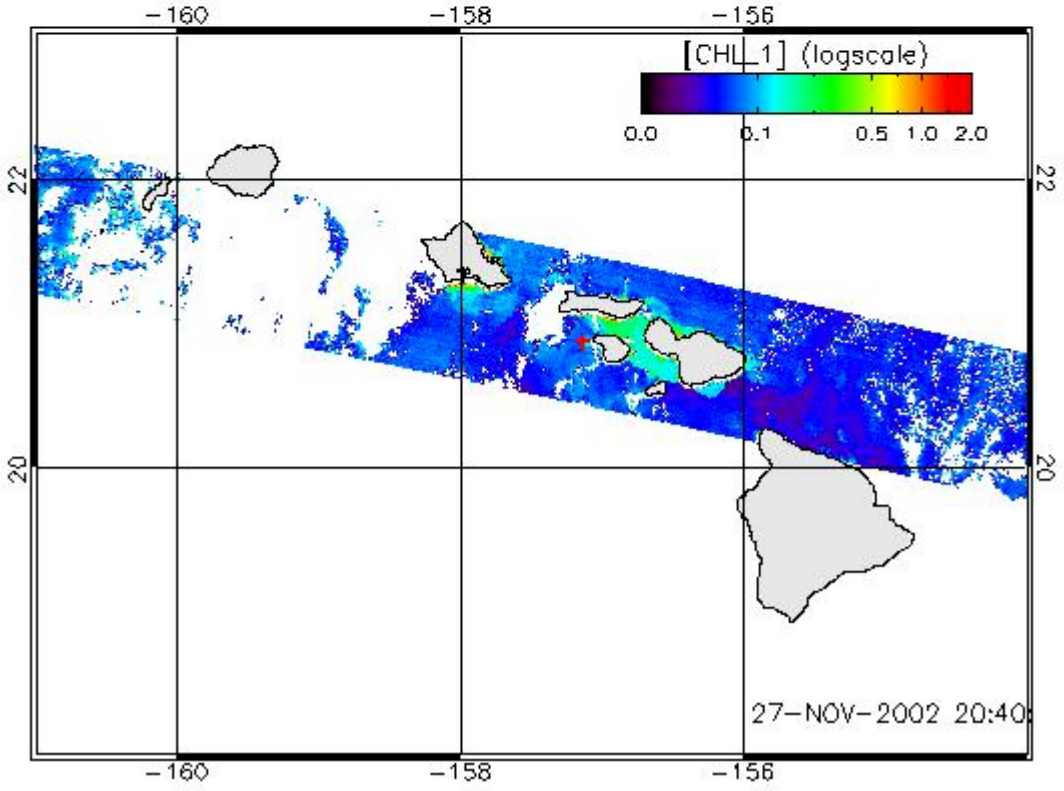
−160
−158
−156
[CHL_1] (logscale)
0.0
0.1
0.5
1.0
2.0
22
20
27−NOV−2002 20:40

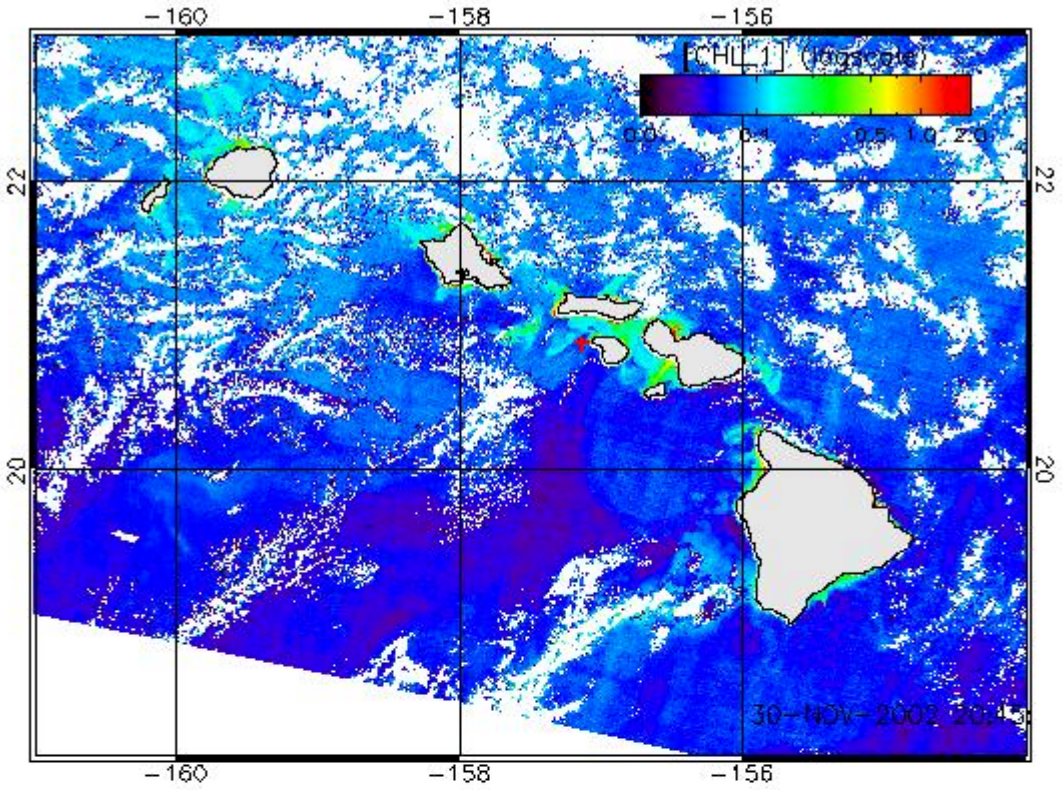
−160
−158
−156
22
20
[CHL_1] (logscale)
0.0
0.1
0.5
1.0
2.0
30−NOV−2002 20:2

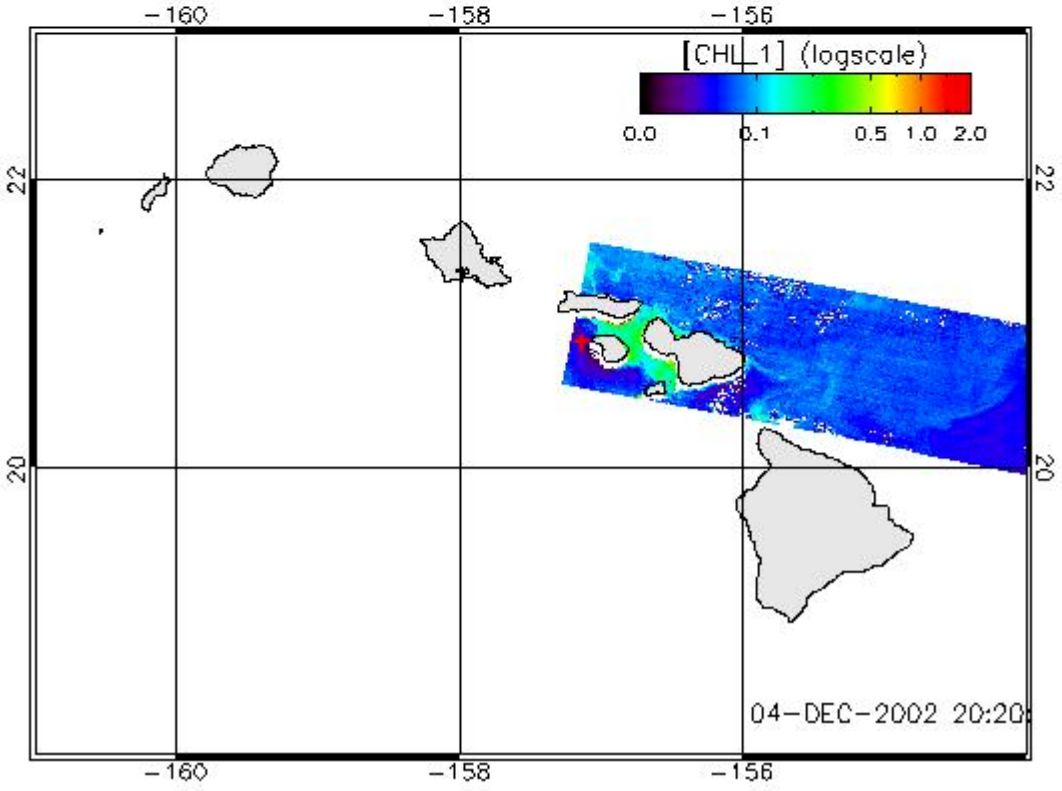
−160
−158
−156
22
20
[CHL_1] (logscale)
0.0
0.1
0.5
1.0
2.0
04−DEC−2002 20:20

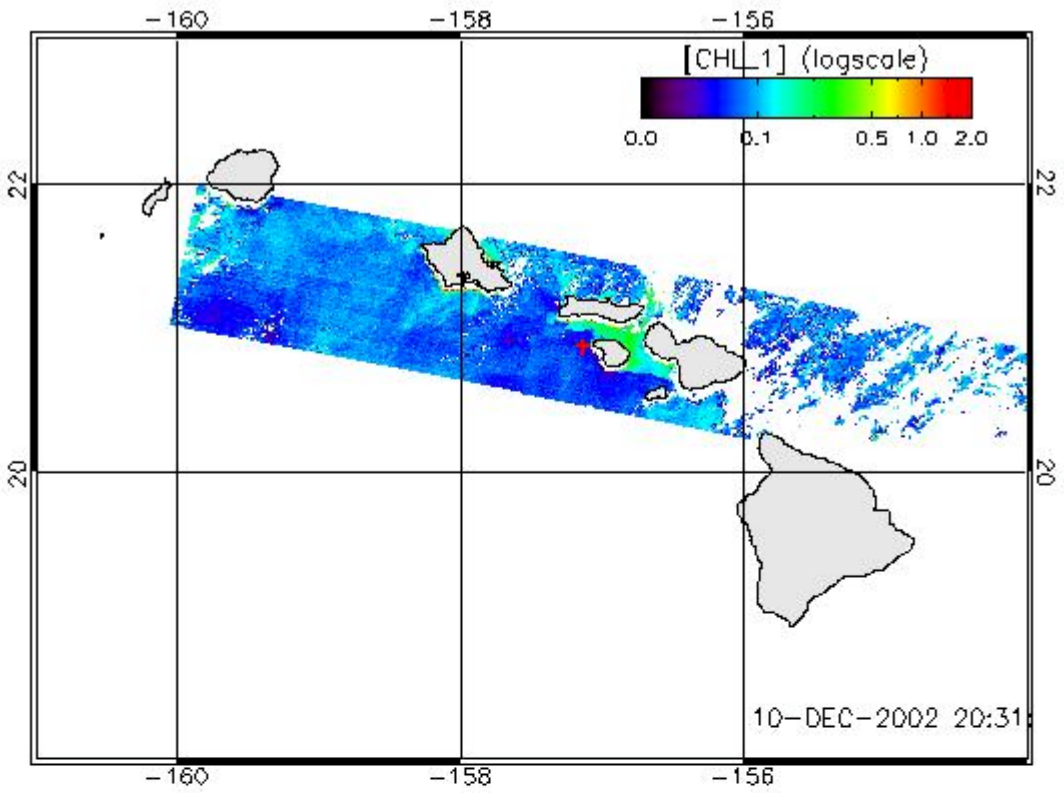
−160
−158
−156
[CHL_1] (logscale)
0.0
0.1
0.5
1.0
2.0
22
20
10−DEC−2002 20:31

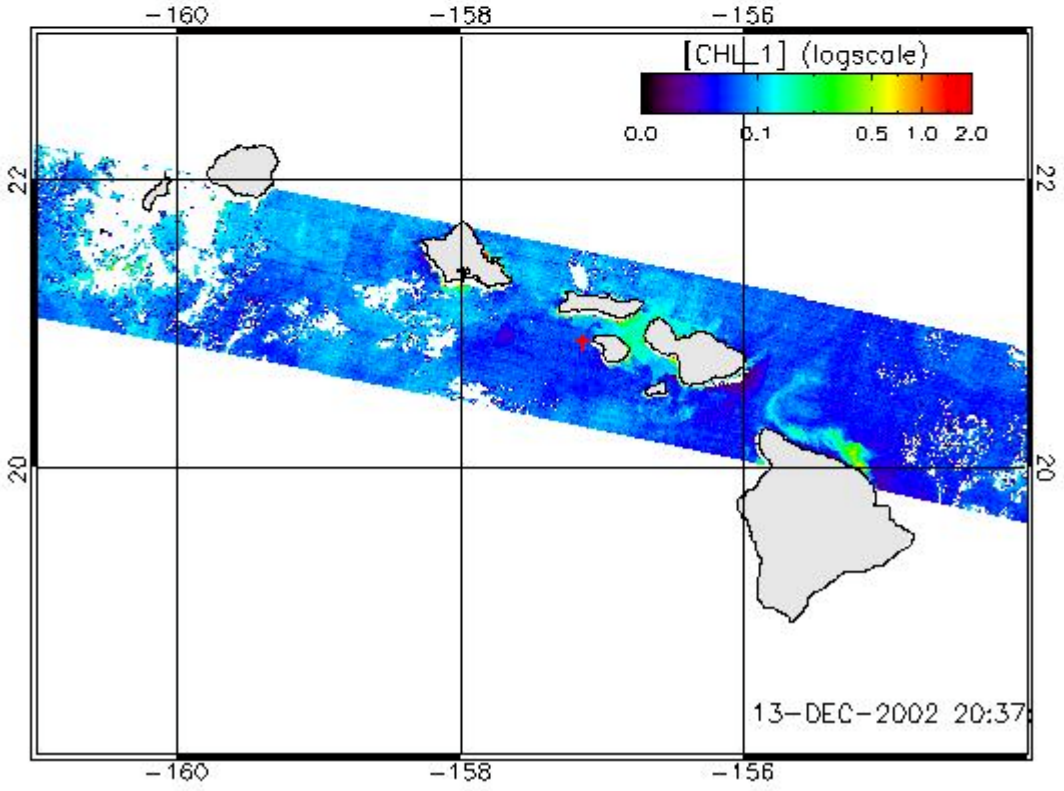
−160
−158
−156
[CHL_1] (logscale)
0.0
0.1
0.5
1.0
2.0
22
20
13−DEC−2002 20:37

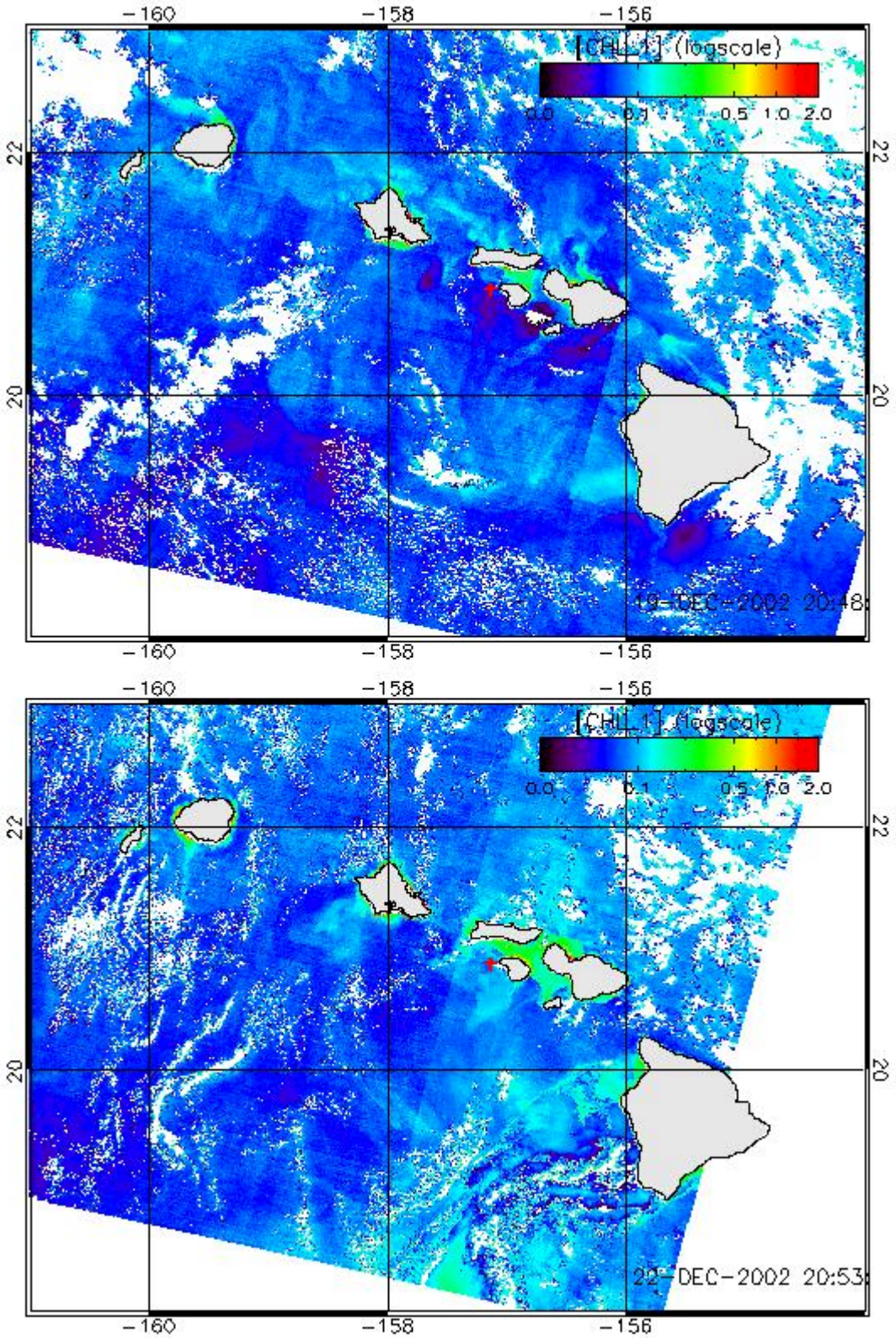
-160
-158
-156
22
20
[CHL_1] (logscale)
0.0
0.1
0.5
1.0
2.0
19-DEC-2002 20:48
22-DEC-2002 20:53

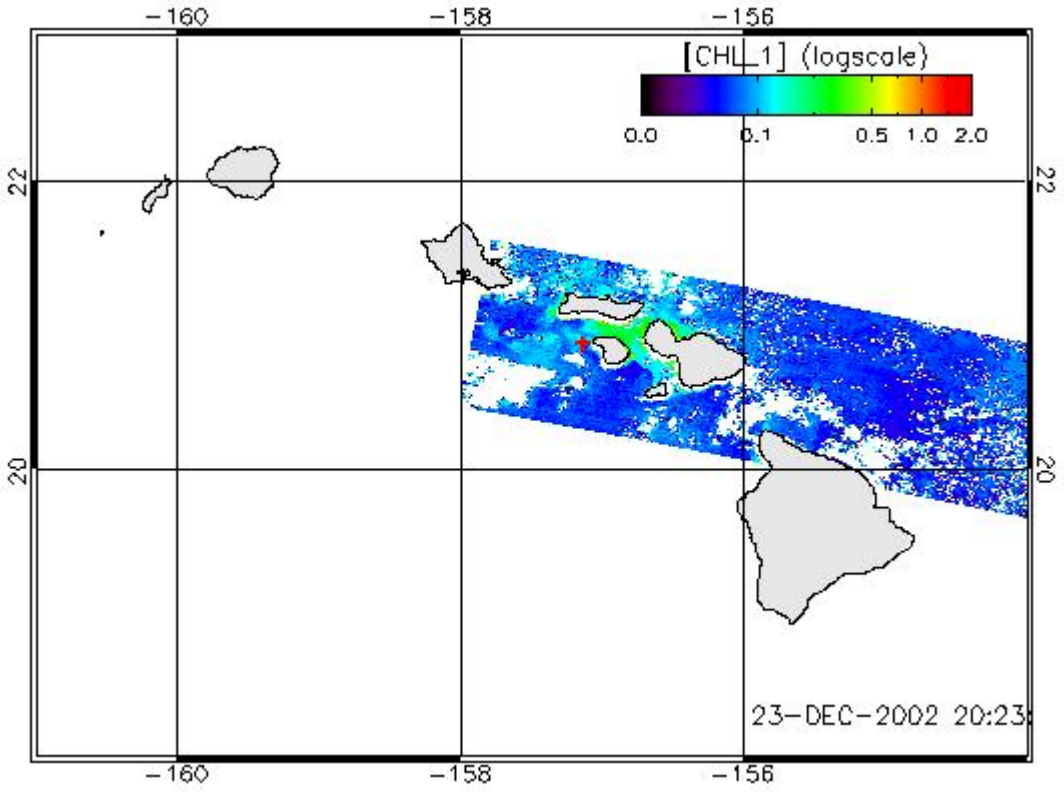
−160
−158
−156
[CHL_1] (logscale)
0.0
0.1
0.5
1.0
2.0
22
20
23−DEC−2002 20:23:

13 Appendix 2 : MERIS band passes

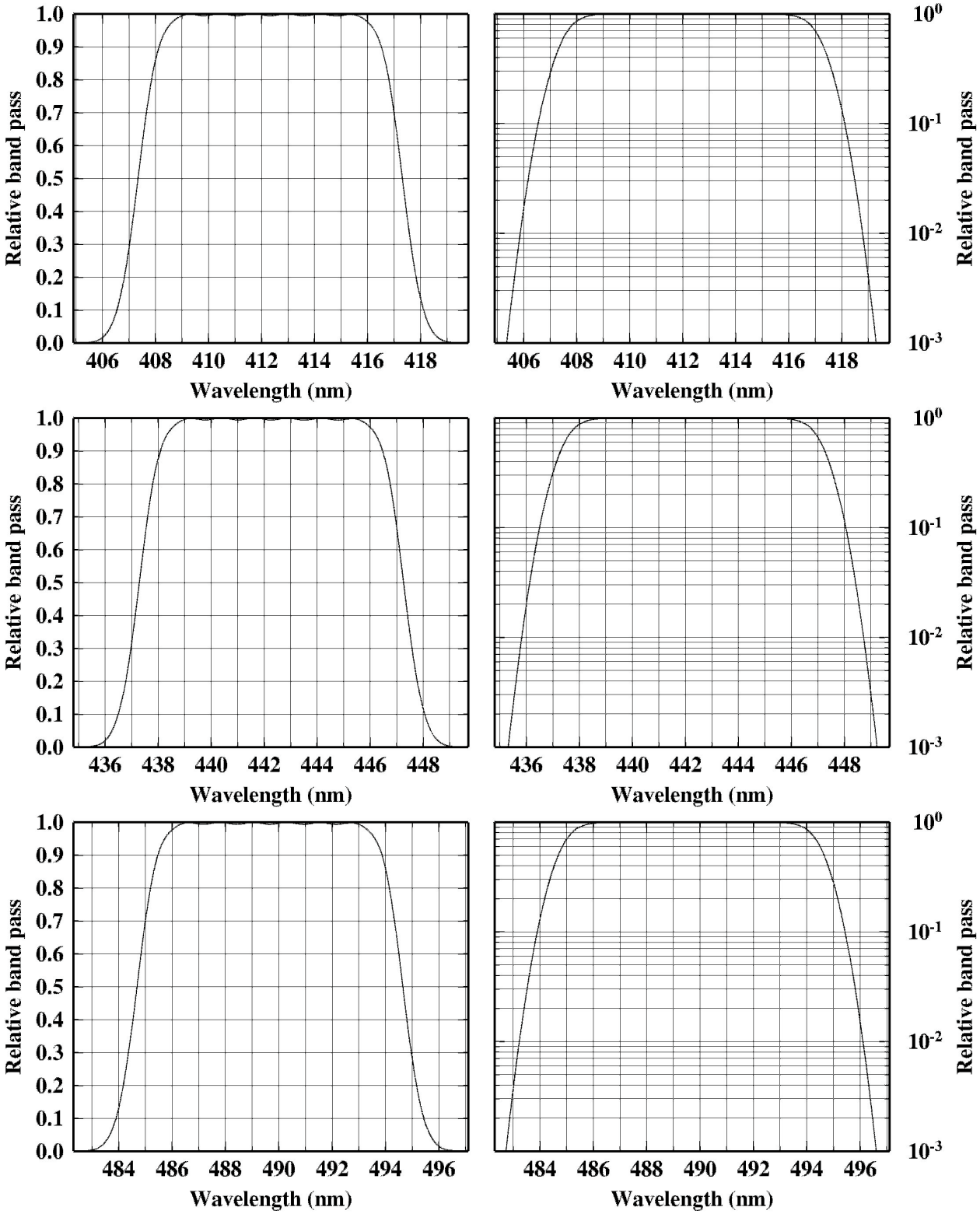

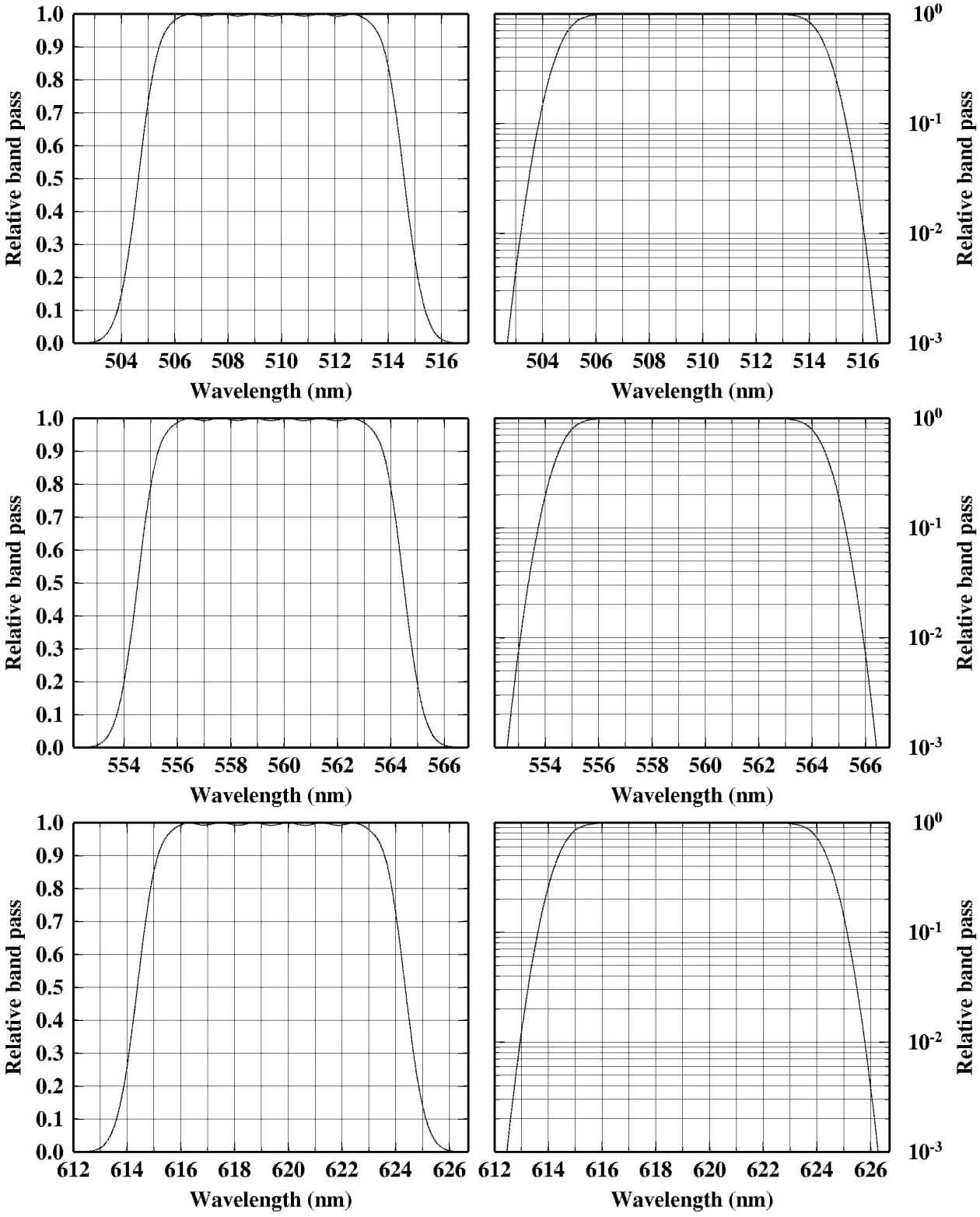
Relative band pass
Wavelength (nm)
1.0
0.9
0.8
0.7
0.6
0.5
0.4
0.3
0.2
0.1
0.0
504 506 508 510 512 514 516
554 556 558 560 562 564 566
612 614 616 618 620 622 624 626
10^{0}
10^{-1}
10^{-2}
10^{-3}

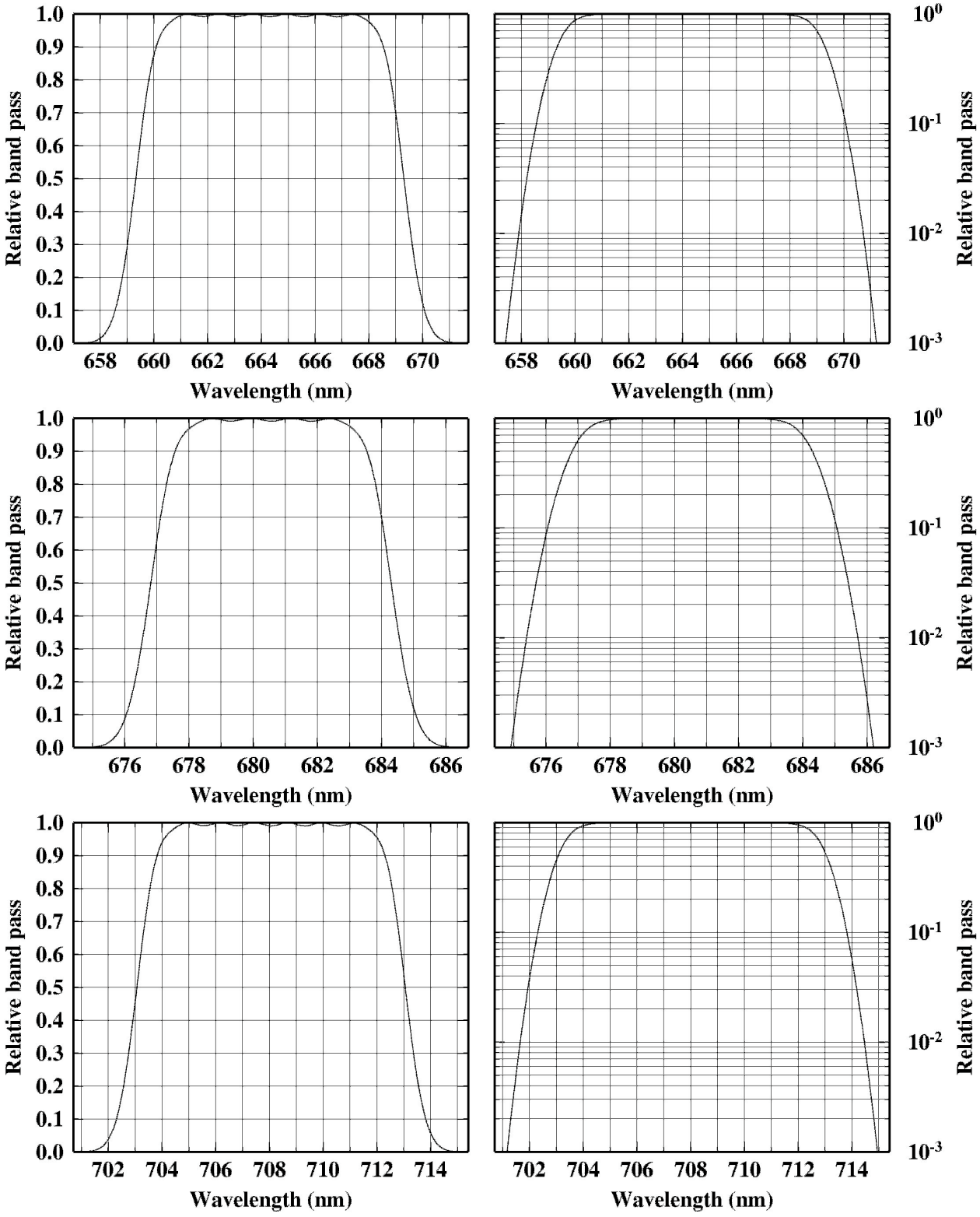
Relative band pass
Wavelength (nm)
1.0
0.9
0.8
0.7
0.6
0.5
0.4
0.3
0.2
0.1
0.0
658 660 662 664 666 668 670
676 678 680 682 684 686
702 704 706 708 710 712 714
10^{0}
10^{-1}
10^{-2}
10^{-3}